Evaluation of in vivo magnetic resonance imaging based measurement of myelin water

Charmaine L. L. Chia, B.Sc.

Medical Physics Unit

McGill University, Montreal

June 2006

A thesis submitted to McGill University in partial fulfillment of the requirements of the degree of Master of Science.

Your file Votre référence
ISBN: 978-0-494-28475-9
Our file Notre référence
ISBN: 978-0-494-28475-9

Abstract

In vivo magnetic resonance spin-spin relaxation data can be decomposed into T_2 distributions using a non-negative least squares algorithm thereby allowing multiple water compartments of tissue to be distinguished. In brain, T_2 distributions typically contain myelin water (MW), intra/extra-cellular water, and cerebrospinal fluid. The percentage of MW signal to the total T_2 distribution signal constitutes the myelin water fraction (MWF), which is related to myelin content, making it a useful measure for monitoring demyelinating diseases like multiple sclerosis.

This thesis presents simulations of T_2 decay curves for white and grey matter brain tissue models and investigates the effect of analysis procedures on the T_2 distribution and the MWF estimates. Cross-site reproducibility and scan re-scan experiments were also conducted to establish the reliability of MWF estimates and hence the applicability of the technique for clinical trials.

Résumé

LES mesures de relaxation T_2 *in vivo* peuvent êtres décomposées en distributions de T_2 en utilisant une variation non-négative de la méthode des moindres carrés, permettant l'identification de multiples compartiments d'eau tissulaire. Dans le cerveau, les distributions de T_2 présentent habituellement des compartiments d'eau attribués à la gaine de myéline ("l'eau myélinique"), au cytoplasme et au fluide interstitiel, ainsi qu'au liquide céphalo-rachidien. Le rapport entre la fraction du signal de l'eau associée à la gaine de myéline et le signal total de la distribution représente la "fraction d'eau myélinique". Cette fraction est reliée à la présence de la gaine de myéline, d'où son utilité comme mesure pour la surveillance de maladies démyélinisantes telle la sclérose en plaques.

Ce mémoire présente des simulations de courbes de relaxation T_2 de modèles de substance blanche et de substance grise. Ces simulations ont servi à l'étude de l'impact du choix de méthode d'analyse sur les distributions de T_2 et sur l'évaluation de la fraction d'eau myélinique.

Des essais furent également effectués pour évaluer la reproductibilité inter-site et inter-examen afin d'établir la fiabilité des mesures de la fraction d'eau myélinique et par conséquent l'applicabilité de cette technique aux fins d'essais cliniques.

Acknowledgments

I would like to express my appreciation to my supervisor, Dr. G. Bruce Pike, for his guidance, support and endless encouragement during my studies and research. My acknowledgement also goes to Dr. Ervin Podgorsak for giving me the opportunity to study Medical Physics at McGill University.

Many thanks to my lab mates for their assistance throughout the course of this project and for creating a fun and stimulating environment. This thesis would have been much more arduous without Drs. Bojana Stefanovic, Jan Warnking, Mark Griffin, Jennifer Campbell, Katerina Klepousniotou, as well as Ives Levesque, Jean Chen, Karma Advani, Vivian Woo, Ilana Leppert, Michael Ferreira, Leili Torab, Clarisse Mark, and Christine Tardif. I also wish to thank Dr. John Sled for his help, Margery Knewstubb and Jennifer Chew for administrative assistance, and the MRI technicians for helping to run studies.

I would also like to extend my thanks to Dr. Alex MacKay and Thor Bjarnason for their advice and collaboration on this project. I am also grateful to Vicky Huang, Sara St. James, and Dr. Katherine Kousaie for their moral support and comraderie. Lastly, and most importantly, I am indebted to my family, the pillar which I constantly leaned on, who gave me unwavering love, support and encouragement throughout my Masters program in Montreal.

Contents

Abstract i

Résumé ii

Acknowledgements iii

Contents vi

List of Figures ix

List of Tables xi

List of Abbreviations xii

1 Introduction 1

2 Background 4

2.1 Myelin in the Central Nervous System 4

2.1.1 The Nervous System 4

2.1.2 Myelin 6

2.1.3 Multiple Sclerosis 7

2.2 Magnetic Resonance Imaging 11

2.2.1 Basic NMR Physics 12

2.3 Investigating Multiple Sclerosis using MRI 18

2.3.1 Non-conventional MR Imaging Techniques 19

3 Simulations **30**

3.1 White and Grey Matter Models 30

3.2 Non-Negative Least Squares Algorithm 32

3.2.1 Regularized NNLS Solutions 33

3.2.2 NNLS Analysis Parameters 36

3.3 Calculating Myelin Water Fraction Estimates 39

3.4 Simulation Results 40

3.4.1 NNLS Solution for Noise-free Data 40

3.4.2 The Effect of SNR and Regularization 40

3.4.3 T_2 Distributions and MWFs for Varied MW Pool Weights 43

3.4.4 The Effect of CSF Contamination 44

4 Experimental Materials and Methods **49**

4.1 Sequence Design 49

4.1.1 qT_2 Protocols 51

4.2 Human Studies 53

4.2.1 Cross-site Comparison 55

4.2.2 Scan Re-scan Reproducibility 56

4.2.3 Across Subjects and Regional Variations 58

5 Results **60**

5.1 Cross-site Reproducibility of MWF Estimates 61

5.2 Scan Re-scan Reproducibility of MWF Estimates 65

5.3 MWF Estimates in Healthy Subjects 71

6 Discussion **78**

6.1 Simulation Study 79

6.2 NNLS Analysis Procedure 81

6.2.1 Defining Exact Myelin Water Ranges 84

6.3 Scan Re-scan Reproducibility of MWF Estimates 88

6.4 Subject and Regional Variations of MWF Estimates 90

6.5 Cross-site Reproducibility 92
6.5.1 Protocol Differences and the Effect on T_2 Distributions 92

7 Conclusion and Future Work **94**
7.1 Summary 94
7.2 Future Work 95

A Ethics Approval **96**

Bibliography **98**

List of Figures

2.1 A schematic of the main parts of a neuron. 5

2.2 A cross-sectional view of a myelinated axon. 6

2.3 A graph showing various forms of MS and their levels of disability over time. 9

2.4 Axon demyelination and remyelination, transection, and degeneration. . . . 11

2.5 Example PD-, T_1-, and T_2- weighted images of an MS patient. 17

2.6 The 2-pool model illustrating magnetization transfer effects. 23

2.7 The 4-pool model illustrating magnetization exchange between various proton pools. 27

3.1 A sample multi-component T_2 decay curve and its corresponding unregularized and regularized T_2 distributions. 35

3.2 One thousand realizations of T_2 distributions of a WM model with various SNR levels. 41

3.3 MWF histograms of WM data (varying SNR) calculated with different MW range cut-offs. 41

3.4 T_2 distributions from SNR = 200 WM data analyzed with various allowed ranges of regularization. 43

3.5 MWF histograms for SNR = 200 WM data with different amounts of regularization using the 50.1 ms MW range cut-off. 44

3.6 T_2 distributions and corresponding MWF histograms from SNR = 200 data analyzed with 2 - 2.5% allowed increase in χ^2. 45

3.7 T_2 distributions from GM model data (1000 realizations, SNR = 200, 2 - 2.5% allowed χ^2 increased, MWF 2%) with varying CSF weightings. . . . 46
3.8 T_2 distributions from WM model data (1000 realizations, SNR = 200, 2 - 2.5% allowed χ^2 increased, MWF 14%) with varying CSF weightings. . . . 47
3.9 MWF histograms using different MW ranges for a SNR = 200 GM model (MWF 2%) with various amount of CSF contamination. 47
3.10 MWF histograms using different MW ranges for a SNR = 200 WM model (MWF 14%) with various amount of CSF contamination. 48

4.1 Schematic of the 32-echo spin-echo sequence for multi-component T_2 quantification. 51
4.2 Comparison of sample 5^{th} echo images acquired with the UBC and MNI protocol. 52
4.3 The single-slice acquired for human studies with examples of various ROIs. 54
4.4 Illustration of the WM ROIs chosen and their sub-divisions. 57

5.1 T_2 distributions for Protocol 1 data collected at UBC and MNI and analyzed by both sites. 62
5.2 T_2 distributions for Protocols 1 and 2 data collected and analyzed at MNI. . 64
5.3 Entire ROI T_2 decay curves and their differences for Protocol 1 data collected on four separate scans on the same slice of the same subject. 67
5.4 Entire ROI T_2 distributions for Protocol 1 data collected on four separate scans on the same slice of the same subject. 68
5.5 T_2 distributions for sub-sections within the entire ROI from Protocol 1 data collected on four separate scans on the same slice of the same subject. . . . 69
5.6 $\overline{MWF}$s (σ as error bars) calculated with different MW ranges from T_2 distributions with different amount of regularization. 70
5.7 Comparison of the protocols' decay curves (normalized) and distributions (2 - 2.5% regularization). 72

5.8 Regularized T_2 distributions using the UBC protocol, 2 - 2.5% regularization and their underlying LS-solutions from a normal subject. 73
5.9 MWF estimates calculated with different MW ranges for UBC protocol data. 75
5.10 MWF estimates calculated with different MW ranges for MNI protocol data. 75
5.11 Summary plot of $\overline{MWF}$ estimates (error bars represent σ) from UBC protocol data for various MW ranges. 76
5.12 Summary plot of $\overline{MWF}$ estimates (error bars represent σ) from MNI protocol data for various MW ranges. 76
5.13 Myelin water maps of a healthy subject created with different MW ranges and regularization. 77

6.1 A T_2 distribution from *in vivo* data with different amounts of regularization showing how MW range cut-offs are crucial in defining MWFs. 83
6.2 Select plots from literature showing MWF estimates across various brain structures in normal subjects. 87

List of Tables

2.1 Percentage of total protein and lipid in myelin, white matter, and grey matter in the human brain. 7

2.2 T_1 and T_2 values of some normal tissue types at 1.5 T at body temperature (37°C). 13

2.3 Sequence timing parameters required to give PD-, T_1- and T_2- weighted images. 17

3.1 Pool weightings used in the simulation study. 31

3.2 Simulation analysis parameters. 37

3.3 T_2 vector of 120 logarithmically spaced values between 10 and 4000 ms. . . 42

4.1 Comparison of the UBC (Protocol 1) and MNI (Protocol 2) protocols. . . . 52

4.2 Summary of the protocol acquisitions and analysis carried out for the cross-site reproducibility study. 55

4.3 Summary of the number of voxels in the ROIs for various protocols. 59

5.1 Summary of the MWFs from Protocol 1 data acquired at UBC and MNI. . . 61

5.2 Summary of the MWFs from Protocol 2 data acquired and analyzed at MNI. 62

5.3 Summary of the MWFs using different integration limits from Protocol 1 data acquired at UBC and analyzed at UBC. 63

5.4 Summary of $\overline{MWF}$s using a 10 - 40 and 10 - 50 ms MW range for various allowed increases of χ^2 for the genu of the corpus callosum. 66

5.5 Summary of $\overline{MWF}$s using a 10 - 40 and 10 - 50 ms MW range for various allowed increases of χ^2 for the splenium of the corpus callosum. 66
5.6 Summary of $\overline{MWF}$s using a 10 - 40 and 10 - 50 ms MW range for various allowed increases of χ^2 for the left minor forceps. 69
5.7 Summary of $\overline{MWF}$s using a 10 - 40 and 10 - 50 ms MW range for various allowed increases of χ^2 for the right minor forceps. 69
5.8 $\overline{MWF}$ for various ROIs in normal subjects using various protocols. 74

6.1 Analysis parameters from select publications using NNLS. 82
6.2 MWC and RC from the test/retest study by Vavasour *et al.* as a comparison to our scan re-scan results from UBC protocol data. 88
6.3 Calculated sample sizes required to ensure statistical power. 90

List of Abbreviations

ADC	apparent diffusion coefficient
CSF	cerebrospinal fluid
CPMG	Carr-Purcell-Meiboom-Gill
DTI	diffusion tensor imaging
FLAIR	fluid-attenuated inversion-recovery
FOV	field of view
FWHM	full-width half-maximum
GM	grey matter
^{1}H	hydrogen nuclei
IE	intra/extra-cellular
LC	linear combination
LS	least squares
MNI	Montreal Neurological Institute
MR/MRI	magnetic resonance / magnetic resonance imaging
MRSI	magnetic resonance spectroscopy imaging
MT	magnetization transfer
MTR	magnetization transfer ratio
MW	myelin water
MWF	myelin water fraction
NAGM	normal appearing grey matter
NAWM	normal appearing white matter
NMR	nuclear magnetic resonance
NNLS	non-negative least squares

PKU	phenylketonuria
QA/QC	quality assurance / quality control
qMT	quantitative magnetization transfer
qT_2	quantitative T_2
RC	reliability coefficient
RF	radio-frequency
ROI	region of interest
SE	spin echo
SNR	signal-to-noise ratio
SSFP	steady-state free-precession
T	Tesla
T_1	spin-lattice relaxation time constant
T_2	spin-spin relaxation time constant
T_2^*	intrinsic spin-spin relaxation time constant
TE	echo time
TI	inversion time
TR	repetition time
μ	regularizer
UBC	University of British Columbia
UTE	ultra-short TE
WM	white matter

Chapter 1

Introduction

MEDICAL physics is relatively new in the field of medicine considering that Wilhelm Röntgen discovered x-rays just over a century ago in 1895. Soon after, discoveries were made in natural radioactivity, quantization of energy, and intricacies of the atom (the Bohr model), to name a few. Medical physics techniques started with x-ray radiographs and continued with ionizing radiation for therapy, early development of nuclear medicine and detection systems, cobalt-60 therapy units, ultrasound, computed tomography (CT) and magnetic resonance imaging (MRI). X-rays and CT scans depend on the photoelectric effect and Compton interactions from ionizing radiation, while nuclear medicine scans (e.g., positron emission tomography (PET) or single photon emission computed tomography (SPECT)) involve the injection of radioactive material and detection of radiation emitted from the patient. These imaging modalities are potentially harmful, whereas MRI is a non-invasive procedure which employs strong magnetic fields in the radio-frequency range to obtain information from hydrogen nuclei (protons) in the human body.

MRI is now well-recognized for its ability to gather anatomical information with millimetre scale isotropic resolution, and also biochemical and functional information. Qualitative and quantitative images are used to diagnose and study pathologies throughout the body such as cancer, vascular disease, and musculoskeletal and neurological disorders. Conventional magnetic resonance (MR) techniques give qualitative images with contrast due to differences in proton density (PD) and relaxation times (T_1 and T_2) which allow

pathological tissue to be easily distinguished from healthy tissue. Novel techniques like magnetization transfer (MT), diffusion tensor imaging (DTI), MR spectroscopy (MRS) and multi-echo T_2 acquisitions are able to give quantitative measures of biophysical parameters, thereby potentially improving pathology specificity.

Motivation

Multiple sclerosis (MS) is a debilitating neuro-degenerative disease characterized by demyelination in the central nervous system (CNS), especially in white matter (WM) of the brain. Although there are treatments, medications and therapies for MS, there is unfortunately no cure. Currently, MS research efforts are substantial and diverse and include pediatric MS, bone marrow transplant, genetic susceptibility, immunology and myelin repair. Although the predominant role of MRI is clinical diagnosis and monitoring of the disease, quantitative MRI is gaining increased importance in MS research.

In order to retard, prevent, or reverse loss of myelin in MS, a clear understanding of myelin pathology is required as well as methods to measure myelin status *in vivo*. This thesis focuses on one such method of *in vivo* myelin imaging termed T_2 relaxometry which is based on quantitative analysis multi-echo MRI acquisitions. Specifically, this method allows the estimation of the myelin water fraction (MWF), which is expected to be closely linked with myelin content. While this method has been pioneered by the group of Alex MacKay at the University of British Columbia (UBC) during the past 12 years, preliminary experience with the technique in this lab showed disappointingly high variability in results. The overall objective of this thesis was therefore to investigate the potential origins of this instability and to quantitatively establish the currently achievable reproducibility of MWF estimates to determine the applicability of the technique in a clinical research context. Our approach to investigating this technique began with simulations of a multi-component brain tissue model to achieve a better understanding of how MWF estimates are affected by signal-to-noise ratio (SNR) levels and analysis procedures. A scan re-scan experiment on a healthy subject was then performed to estimate measurement reproducibility, as well as a cross-site comparison of the most established multi-echo protocol. The T_2 relaxometry

work presented in this thesis also complements other quantitative MRI research in MS at the Montreal Neurological Institute's McConnell Brain Imaging Centre.

Outline

Chapter 2 contains an introduction to MS, the disease motivating this research, followed by a brief review of the basics of MRI and a literature review of its use in the study of MS. Chapter 3 describes the simulation process, analysis procedures and results from the simulation study. Chapter 4 describes the multi-echo pulse sequence design and different protocols tested as well as the various *in vivo* human studies performed. Chapter 5 presents results from the *in vivo* experiments, and Chapter 6 discusses the use of MWF estimates from qT_2 studies as a biomarker for myelin. The last chapter closes with concluding remarks as well as considerations for future investigations.

Chapter 2

Background

2.1 Myelin in the Central Nervous System

2.1.1 The Nervous System

The nervous system is built on *neurons* (nerve cells) and *glial cells* (non-neuronal supporting cells), and acts as the major regulatory, controlling and communicating system in the body. It is largely made up of the *central nervous system* (CNS), which consists of the brain and the spinal cord. The neuron, found in abundances of billions in the human brain, is the functional unit of the nervous system while glial cells primarily serve the needs of neurons. The neuron (refer to Figure 2.1) contains a cell body which has two main kinds of long processes extending from it: typically several branch-like *dendrites* and one *axon* (also called a *nerve fibre*). The axon's purpose is solely to conduct nerve impulses from the cell body to other cells, while the dendrites receive signals from neighbouring nerve cells. The diameter of the axon, among other factors, determines the velocity of the nerve impulse. Many tasks carried out by the nervous system requires fast signal conduction, but extremely thick axons would not be an efficient use of space to transport signals throughout the body. Instead, a crucial component which allows extremely rapid signal conduction without requiring thick nerve fibres is the axonal membrane *myelin* [1].

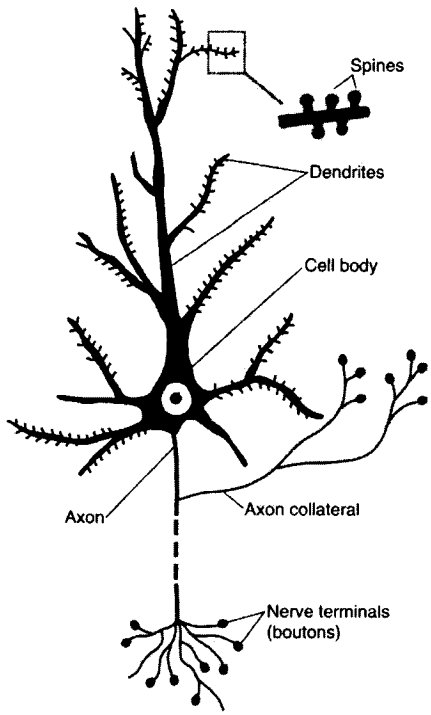

Figure 2.1: A schematic of the main parts of a neuron [1].

2.1.2 Myelin

Myelin is a lipid-protein membrane found primarily in the *white matter* (WM) of the CNS and in the large motor axons in the *peripheral nervous system* (PNS). *Oligodendrocytes* and *Schwann's cells* produce myelin in the CNS and PNS, respectively. Oligodendrocytes can extend up to 50 processes, ensheathing multiple nerves simultaneously. Myelination begins with contact between axonal membranes and oligodendrocytes in a compaction (winding) process within the cytoplasmic space to form a myelin sheath of closely packed membrane pairs separated by narrow fluid spaces [2]. An increase in axonal diameter of myelinated axons and the process of saltatory conduction (i.e., the transmission of action potentials from node to node) both contribute to an increase in conduction velocity. While unmyelinated axons have conduction speeds less than 1 m/sec, the thickest myelinated axons conduct at about 120 m/sec [1]. Figure 2.2 contains a cross-sectional view showing the ultrastructure of a myelinated nerve fibre in the CNS.

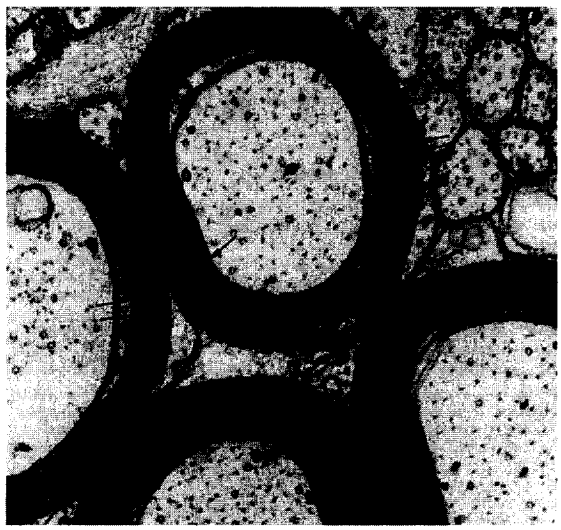

Figure 2.2: A cross-sectional view of a myelinated axon [3].

The human brain consists of ~35% myelin (percent dry weight). GM contains nerve bodies with few myelinated axons while WM, of which 50 - 60% is myelin, consists of myelinated axons. WM appears whitish upon visual inspection due to the large proportion of lipid in myelin. The percentage protein and lipid composition in Table 2.1 explains why

WM and GM have different water contents (72 and 82%, respectively) due to WM's larger quantity of myelin which is a relatively dehydrated structure [4].

Damage to myelin can be caused by exposure to toxins, infection, injury, degeneration, or autoimmune disease. The result of myelin damage includes decreased conduction velocity and loss of cell-cell interactions between the axon and myelinating glial cells, which can cause destabilizing changes in the axonal cytoskeleton. Areas with demyelination are left with hard, scarred tissue called *plaques* or *lesions*. The process itself is not all-or-none, but can range from little damage to complete loss of the myelin sheath. The regions proximal and distal to the area of demyelination appear to have normal conduction, while abnormalities are confined to regions of demyelination in focally demyelinated fibres. Although demyelinated lesions can retard conduction, it does not necessarily lead to clinical deficit [5].

Remyelination in the CNS occurs in two stages: (i) recruitment phase (oligodendrocytes proliferate and migrate to the site of injury), and (ii) differentiation phase (oligodendrocytes make contact with axons to form the myelin sheath) [2]. Axons in the CNS are capable of remyelinating, but may not be able to do so in all affected regions since oligodendrocytes are responsible for ensheathing up to 50 axons simultaneously. Furthermore, oligodendrocyte cell-loss in affected areas cause remyelination to be impossible [2, 4].

2.1.3 Multiple Sclerosis

Multiple sclerosis (MS), or *sclérose en plaques* as originally described in 1868 by Jean-Martin Charcot (1825-1893) [6], is the most common demyelinating disorder in humans

Table 2.1: Percentage of total protein and lipid in myelin, white matter, and grey matter in the human brain (percentages are based on dry weight) [4].

Substance	Myelin	WM	GM
Total protein	30%	39%	55.3%
Total lipid	70%	54.9%	32.7%

and the most common cause of neurologic disability in young adults [2]. There is an estimated 2.5 million sufferers worldwide, and everyday 3 people in Canada are diagnosed with MS [7]. Although all age groups can be affected, MS mainly affects individuals between 18 - 50 years of age with onset typically around age 30. Rates of incidence are about 2:1 in favour of females to male, although males tend to experience more severe forms and have poorer prognosis [8]. Clinical attacks are neurologic deficits which usually last more than 24 hours, typically for several days. Hallmark symptoms include bladder, bowel, sexual and cognitive dysfunction, dizziness, depression or other emotional changes, fatigue, difficulty in walking, numbness, pain, vision problems, and spasticity. Although etiology is still unknown, the onset of MS has been linked to viral, environmental and genetic factors.

All ethnic groups are susceptible to MS, but Caucasians have a higher incidence even when living in regions with a lower prevalence. Lower prevalence is seen in regions closer to the equator, while countries like Canada, Scotland and Scandinavia have the highest prevalence where about 1 in 1000 have MS. Although geographical residence plays a role in prevalence, the risk of developing MS is also thought to depend on early exposure to environmental agents. For someone who lived their first 15 years in a high-risk region and later migrated to a low-risk region, they will have a higher risk than those in their new host country. The converse is true for someone who migrates from a low- to a high- risk region. It appears minimal or no common environmental factors in childhood or adulthood are responsible for triggering MS in adopted children or spouses of MS patients [9, 10].

There are different forms of MS characterized by the severity and progression of disability (refer to Figure 2.3 for disease time-course): **RR** - relapsing-remitting (70% or higher occurrence in patients), **PP** - primary-progressive (15% occurrence), and **RP** - relapsing-progressive (15% occurrence), where at least two-thirds of relapsing-remitting patients eventually develop a secondary-progressive (**SP**) form. RR MS patients experience relapsing attacks (or exacerbations) with periods of total remission where partial sequelae or total improvement may occur. After each attack, disability may accumulate and their clinical presentation may be SP where they sustain continuous deterioration de-

spite no new attacks. The PP form shows no stabilization or periods of recovery with a gradual accumulation of disabilities with acute or sub-acute onset of symptoms. The RP form is characterized by recurrent attacks but significant progression of disability between attacks. It is sometimes hard to distinguish the early conversion of the progression from RR to SP patients. Lastly, SP is a relapsing form which becomes a continuous progressive course with periods of stabilization or mild remission or even the occasional attack [2, 11]. Diagnosis of MS is based on clinical evidence of lesions of the CNS, disseminated in time and space.

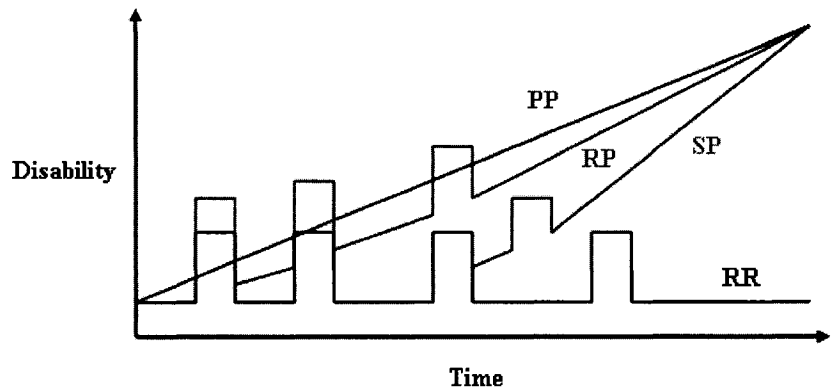

Figure 2.3: A graph showing various forms of MS and their levels of disability over time.

MS is an autoimmune disease where the body is unable to distinguish its own cells from foreign cells and orchestrates attacks on its own tissue. It is primarily characterized by inflammation of the CNS where the myelin sheath is the main target of tissue injury. These regions form lesions which are well known to have a reduction in lipid content from loss of myelin which is replaced by water. Remyelination can spontaneously repair MS lesions, more so in earlier stages of MS than in later stages or more progressive forms. In general, remyelination occurs in small lesions, and even so the sheaths are disproportionately thin for the axon diameter and are limited to the lesion edges [4, 12]. There currently is research focused on repairing damaged myelin sheaths. *In vivo* transplantation of human oligodendrocytes and Schwann cells into rodents have been successful in remyelinating

axons. Therefore, it is possible to evaluate the ability of *in vivo* remyelination in human cells based on the same models used to evaluate rodent cells [5]. To date, there is still no effective human therapy to rectify the damage caused to the myelin sheath during MS.

Although inflammation primarily leads to myelin loss (as previously described in Section 2.1.2), axonal loss is also observed [2, 11, 13–16]. Axonal loss has an important role in developing irreversible deficit, but fortunately the mammalian CNS is quite capable of compensating for neuronal loss which reverses, prevents or retards inevitable neurological disability. In RR MS patients, where axonal loss is abundant, inflammation and demyelination causes disability. Subsequent reduction in inflammation, re-organization of sodium channels on demyelinated axons, and remyelination leads to remission. Axonal loss occurring in this type of MS is relatively clinically silent. It may be a continuous, although not necessarily linear, process for RR MS patients to progress to SP MS. The brain may have a threshold beyond which accumulated axonal loss during RR MS leads to further neurological decline and disability. Chronically demyelinated axons will eventually degenerate in SP MS patients who may also have continued axonal loss and inflammation. Animal models, as well as clinical observations suggesting decreasing brain inflammation over time in the later stages of MS, support this latter phenomenon [14]. Figure 2.4 shows the processes described above.

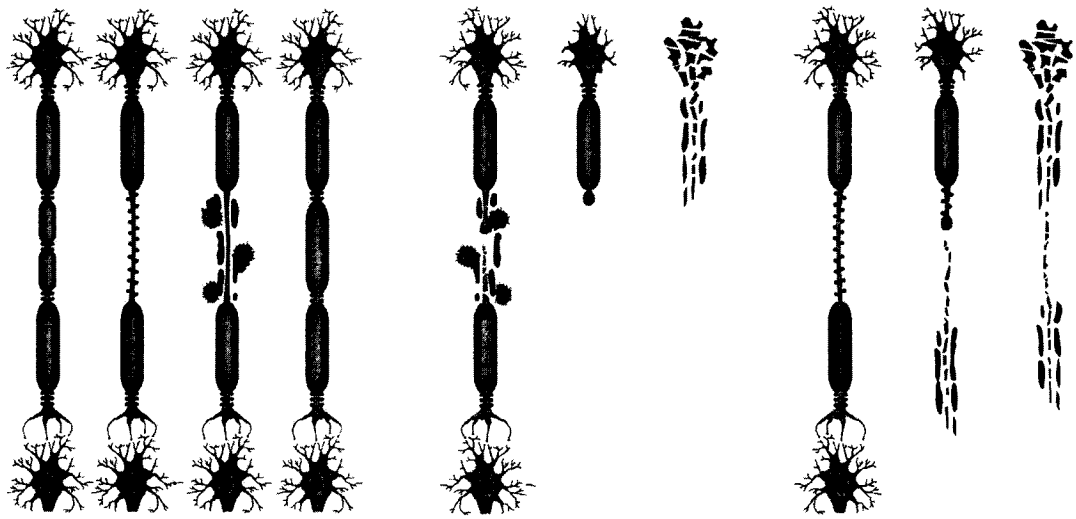

Figure 2.4: (*a*) A nerve fibre undergoing demyelination and remyelination. (*b*) Axonal transection occurring in a demyelinating lesion. (*c*) Chronically demyelinated axons degenerating in multiple sclerosis lesions. (From [17].)

2.2 Magnetic Resonance Imaging

The phenomenon of *nuclear magnetic resonance* (NMR) in condensed matter was first observed using different methods: F. Bloch used induction [18, 19] and E. M. Purcell used absorption [20]. Both shared the 1952 Nobel Prize in Physics for this achievement. NMR has since been a powerful non-invasive analysis tool allowing the study of physical and chemical properties of matter. However, it was not until the 1970's, when the first imaging principles were developed, that P. C. Lauterbur obtained the first NMR images in 1973 [21]. In 2003, Lautebur and Mansfield shared the Nobel Prize in Medicine for their work which made MRI possible.

2.2.1 Basic NMR Physics

Generation of the Magnetization Vector *M*

When hydrogen (^{1}H) is put in a magnetic field, it has an associated energy E as a result of the interaction between its magnetic moment **m** and the field **B**. Two possible energy states arise from the two possible orientations in the magnetic moment, known as Zeeman energy splitting. The minimum and maximum energy correspond to the nucleus aligned *with* ("spin-up") or *against* the field ("spin-down"), respectively. For a large proton population, the ratio of the two spin states is in slight excess of the lower energy state (approximately 7 in 10^6). This results in a *net macroscopic nuclear magnetization* $\mathbf{M}_0$ defined as the total magnetic moment in a unit volume aligned along the *main static magnetic field* $\mathbf{B}_0$.

These nuclear spins precess at a well-defined frequency (known as the *Larmor* frequency), exhibiting resonance. The gyromagnetic ratio, γ, a constant unique to each nuclear species, has a value of 42.576 $\frac{MHz}{T}$ for ^{1}H. The nuclear magnetic moment will experience a torque when **M** and **B** are not aligned. The equation describing the motion for the magnetization vector **M** is:

$$\frac{d\mathbf{M}}{dt} = \mathbf{M} \times \gamma\mathbf{B}. \tag{2.1}$$

The solution to the equation is a gyroscopic precessional motion (analogous to a top spinning about the gravitational field) with the rate of precession, ω, given by the Larmor relation:

$$\omega_o = \gamma B_o. \tag{2.2}$$

Relaxation from Interaction with Radio-frequency Fields

A radio-frequency (RF) pulse, also denoted as $\mathbf{B}_1$, can be applied to perturb the magnetization vector from its equilibrium position. If the RF pulse is applied *on-resonance*, meaning its frequency matches the resonant frequency of the nuclear species of interest, then it is able to rotate **M** away from $\mathbf{B}_0$ by some angle θ governed by the RF pulse strength B_1 and duration τ:

Table 2.2: T_1 and T_2 values of some normal tissue types at 1.5 T at body temperature (37°C) [22].

Tissue	T_1 (ms)	T_2 (ms)
Grey matter	950	100
White matter	600	80
Cerebrospinal fluid	4500	2200
Muscle	900	50
Fat	250	60
Blood	1200	100 - 200

$$\theta = \gamma B_1 \tau \tag{2.3}$$

Upon termination of the RF pulse, **M** will continue precessing while evolving to its thermal equilibrium $\mathbf{M}_0$, resulting in a *free induction decay* (FID). This relaxation process occurs in both the longitudinal and transverse direction. The characteristic time T_1 denotes the relaxation in the longitudinal direction (along $\mathbf{B}_0$, towards $\mathbf{M}_0$) and T_2 denotes the relaxation in the transverse direction (perpendicular to $\mathbf{B}_0$, towards 0). T_1, also called the *spin-lattice* time constant, and T_2, the *spin-spin* time constant, are physical properties that are governed by interactions between the nuclei and their environment (lattice) and different nuclei (spins), respectively. The latter phenomenon has a more dramatic effect on the transverse magnetization signal through the loss of phase coherence due to spin dispersion. Solids typically have $T_1 \gg T_2$, liquids like pure water have $T_1 \approx T_2 \approx 3$ s, and semi-solids like biological tissue have $T_1 > T_2$. Table 2.2 contains typical relaxation values of normal biological tissue types at 1.5 T. As a note, T_1 is dependent on field strength, while T_2 is relatively variant.

The Bloch Equation and its Solution

The Bloch equation is used in classical physics to give a more complete description of the behaviour of macroscopic magnetization vectors. It is based on Equation 2.1 but includes terms for longitudinal and transverse relaxation. The complete equation and its x, y, z directional components are as follows:

$$\frac{d\mathbf{M}}{dt} = \mathbf{M} \times \gamma\mathbf{B} - \frac{M_x\hat{\mathbf{x}} + M_y\hat{\mathbf{y}}}{T_2} - \frac{M_z - M_o}{T_1}\hat{\mathbf{z}} \tag{2.4}$$

$$\frac{dM_x}{dt} = \gamma M_y B_o - \frac{M_x}{T_2} \tag{2.5}$$

$$\frac{dM_y}{dt} = -\gamma M_x B_o - \frac{M_y}{T_2} \tag{2.6}$$

$$\frac{dM_z}{dt} = -\frac{M_z - M_o}{T_1}. \tag{2.7}$$

The general solutions to the Bloch equation can be described in terms of transverse (Equation 2.8) and longitudinal (Equation 2.9) relaxation. The equilibrium, or steady-state solution, of these solutions can be determined from the limit $t \to \infty$ which gives $M_{xy}(\infty) = 0$ and $M_z(\infty) = M_o$.

$$M_{xy}(t) = M_o e^{-\frac{t}{T_2}} \tag{2.8}$$

$$M_z(t) = M_o + [M_{z,o} - M_o]e^{-\frac{t}{T_1}} \tag{2.9}$$

Spin-lattice Interaction and Longitudinal Decay

The T_1 relaxation time indicates how fast the longitudinal component returns to thermal equilibrium after an RF excitation pulse. Saturation and inversion recovery experiments are used to deduce T_1. Saturation recovery experiments are composed of a series of 90° RF pulses and the measurement of the FID. The separation time between the RF pulses is

called the *repetition time*, or TR. By varying TR, the magnetization recovery curve can be mapped out from 0 (TR = 0) to M_0 (TR = ∞).

The inversion recovery experiment is similar to saturation recovery except it achieves twice the dynamic range by employing an initial 180° pulse (inversion pulse) to send M_0 to -M_0. After the inversion pulse, a 90° pulse is applied after a time *TI*. A recovery curve can be mapped out by varying TI. Another advantage of this experiment is the ability to null signal from certain tissues by taking advantage of the curve passing through 0 when TI = $\ln 2T_1$. Enhanced contrast images are made possible by selectively nulling tissues of known T_1.

Spin-spin Interaction and Transverse Decay

The transverse magnetization decays exponentially as $e^{-\frac{t}{T_2}}$, but the observed FID decays at a higher rate (T_2^*) in a real experiment due to magnetic field inhomogeneities in the sample. The spins in the sample will experience a different magnetic environment; therefore, each will precess at slightly different rates, causing the spread in the Larmor frequency. The spins fan out as they lose phase coherence, which prematurely reduces the net magnetization and FID. *Spin echo* experiments refocus the dephasing spins causing a signal maximum at the spin echo (i.e., re-alignment of spins). Upon achieving maximum signal, continued signal decrease occurs as a result of ongoing T_2^* decay. By continually reversing the decay through refocusing pulses an *echo time* (TE) apart, an intrinsic T_2 decay envelope is formed by the train of spin echo amplitudes. Therefore, true T_2 values can be measured with the removal of field inhomogeneity via spin echo experiments. Equation 2.10 shows the relation between T_2^* and T_2 where ΔB represents the measure of field inhomogeneity across the sample.

$$\frac{1}{T_2^*} = \frac{1}{T_2} + \gamma \Delta B \tag{2.10}$$

The original spin echo experiment was performed by E. L. Hahn [23] using two 90_x° pulses which rotates the spins about the x axis. Carr and Purcell [24] modified the experiment such that the 90_x° is followed by a 180_x° pulse (CP sequence). The 90_x° pulse flips the

spins onto the y axis while the refocusing 180°_x would cause the spin echo to align along the -y axis. This experiment was later modified by Meiboom and Gill [25] where a 90°_x pulse is followed by a 180°_y pulse. This experiment, known as the Carr-Purcell-Meiboom-Gill (CPMG) sequence, refocuses the dephasing spins back along the y axis.

The CP and CPMG sequences are quite different in terms of error sensitivity. The CPMG sequence does much better under system imperfections such as flip angle errors. Since the CP sequence pulses are along the same axis, successive non-ideal 180° pulses accumulate error and cause the magnetic moment vector to be further out of the xy plane. The same RF pulse imperfections in the CPMG experiments results in no RF error accumulation since the refocusing pulses are applied about the y axis. Any over- or under- shoot ends up cancelling each other at every other echo [26].

Imaging

MRI is based on the manipulation of ^{1}H in our body's highly aqueous environment. It is a non-invasive diagnostic tool able to differentiate the macromolecular environment and density of mobile protons. The biological differences in water content, or more specifically, the MR physical parameters *proton density* (PD) and *relaxation times* (T_1 and T_2), affect signal strength which gives image contrast, allowing normal and pathologic tissue to be distinguished. The principal imaging sequence parameters affecting the contrast are the: excitation tip angle (θ), echo time (TE), and sequence repetition time (TR). Table 2.3 outlines the parameter requirements for conventional PD-, T_1-, and T_2- weighted images (examples are shown in Figure 2.5).

Table 2.3: Sequence timing parameters required to give PD-, T_1- and T_2- weighted images.

	TE	TR
PD	short	long
T_1	short	short
T_2	long	long

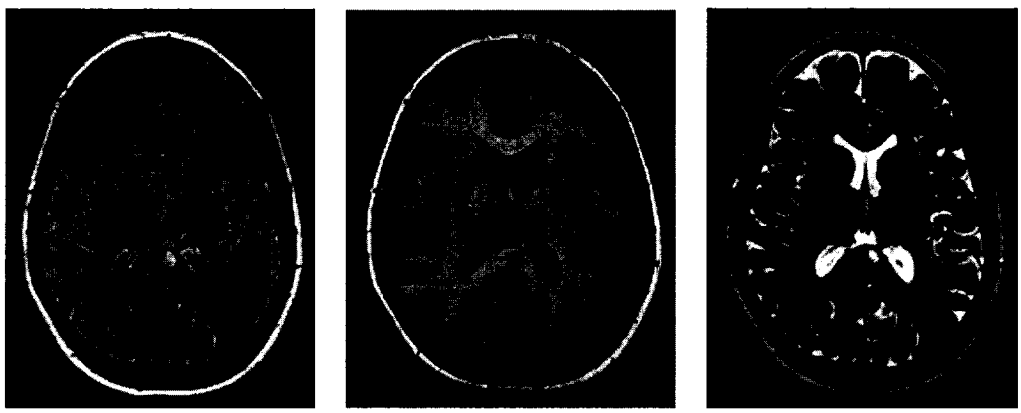

PD T_1 T_2

Figure 2.5: Example PD- (left), T_1 (middle) and T_2- (right) -weighted images of an MS patient with a lesion in the splenium of the corpus callosum.

2.3 Investigating Multiple Sclerosis using MRI

Over the past 20 years, MR has had a major impact on the management and understanding of MS. The current use of MR in MS includes technical issues, role in diagnosis, understanding the disease through natural history studies, and application in clinical trials [27]. MRI has a much greater sensitivity to MS lesions than that of clinical examinations or other imaging modalities like CT scans. Although MS is still clinically diagnosed, MR is the best paraclinical test due to its ability to demonstrate abnormalities in 95% of clinically definite MS patients [15]. Conventional scans include PD-, T_1-, and T_2- weighted imaging (refer to Figure 2.5), as well as fluid-attenuated inversion-recovery (FLAIR) and gadolinium-enhanced T_1-weighted imaging.

By using a short TR, the signal from tissues with short T_1 values is able to recover faster and will appear hyperintense. Protons in bulk water (e.g., in CSF or tissue with loss of structural integrity or associated with edema) with longer T_1 will appear hypointense. T_1-weighted images therefore have less sensitivity to edema but give more pathological specificity. Lesion specificity can be increased selectively with the use of gadolinium (Gd), a paramagnetic contrast agent which is injected into the patient as the compound gadolinium-diethylenetriaminepentacetate (Gd-DTPA). Gd-DTPA is unable to cross the blood brain barrier (BBB) except during the acute inflammatory phase of MS lesion development when the BBB is disrupted [2]. By injecting Gd-DPTA in the patient prior to a T_1-weighted scan, the relaxation times of newly formed lesions are shortened (the T_1 value is more affected than T_2) and acute lesions then appear hyperintense. The majority of these acute lesions are seen on unenhanced T_1-weighted images as acute black holes which may completely resolve. A few hours or few days after enhancement develops, a new lesion can be seen on a PD- or T_2- weighted scan which may enlarge to a variable extent. The same lesion may appear to shrink and reactivate by enhancement and enlargement. This cyclic BBB breakdown and inflammation most likely occurs several times before significant demyelination occurs.

Protons in a less restricted environment will have longer T_2 values and will decay less during a long TE. Tissues such as GM appear hyperintense in T_2-weighted images com-

pared to tissues with shorter T_2 relaxation times, such as WM. T_1-weighted images give great anatomical detail and show MS lesions as hypointense or isointense, but lesions are typically larger and more extensive on T_2-weighted images. T_2-weighted images are highly sensitive to tissues with changes in water content as well as the nature and concentration of tissue macromolecules.

PD- and T_2- weighted images provide qualitatively similar MS pathologic information. Both show lesions increasing in size over several weeks, probably due to inflammation. After about 4 weeks, lesions typically shrink and persist as a smaller stable lesion. Stability is thought to be associated with permanently demyelinated fibre tracts. The lesion may cyclically reactivate due to continuing pathology maturation and later form with neighbouring lesions into a larger confluent lesion. In T_2-weighted images, both CSF and focal lesions appear hyperintense which make defining the extent of periventricular lesions unclear. Because of this, PD-weighted and FLAIR (a modified T_2-weighted sequence which nulls the signal from CSF) images are more useful for identifying lesions near fluid-filled vessels since they appear brighter than the latter [2, 5].

2.3.1 Non-conventional MR Imaging Techniques

Although PD- and T_2- weighted images are sensitive to MS lesions, they are not specific to underlying pathology [28]. As an example, T_2-weighted image lesions may overestimate the degree of pathology due to edema or other forms of increased water content which are not pathologically specific. Just like there are different staining techniques for post-mortem studies, there are different MRI techniques sensitive to different aspects of pathology. As an illustration, some of these techniques are able to show pathologic abnormalities developing in normal appearing white matter (NAWM) before they can be detected using conventional scans.

While conventional techniques give qualitative information, some recently introduced methods have the potential to improve specificity of MR with more precise quantification of certain pathological changes. These MR techniques (briefly described below) include magnetization transfer (MT), functional MRI (fMRI), magnetic resonance spectroscopy

(MRS), diffusion imaging, and multi-component T_2 relaxation. Collecting data using these various techniques will result in a more comprehensive view of the disease.

Functional Magnetic Resonance Imaging

Functional MRI techniques are based on the monitoring of blood oxygen level dependent (BOLD) contrast. Neuronal activity is associated with an increase in metabolism which inherently increases blood flow and oxygen consumption [29]. FMRI indirectly measures neuronal activity from motor, sensory and cognitive brain function using the relative changes in microvascular blood oxygenation. Studies have shown that adaptive cortical changes can limit functional impairment from relapses and promote recovery in MS patients [30, 31].

Magnetic Resonance Spectroscopy

While MRI provides structural information, MRS is able to profile areas of the brain metabolically and biochemically based on a certain chemical species, typically ^{1}H due to its abundance in the body. A typical MR spectra gives resonances in *parts per million* (ppm) as a function of shift relative to a standard compound's frequency. Four major resonances are found in the ^{1}H spectra of human brain at long TEs: choline (Cho), creatine (Cr), N-acetyl groups (NAA), and lactate (Lac). Physiological changes in the brain, such as in MS, appear as changes in concentrations of these metabolites, whether within a lesion or sometimes in adjacent NAWM [32]. Biochemical data can be acquired from a single volume (single-voxel spectroscopy) or multiple voxels to generate an image based on the spectral distribution (magnetic resonance spectroscopic imaging, or MRSI).

The Cho peak is associated with the phospholipids, and the height of the peak serves as an internal control since the concentration of Cho in the brain is relatively constant. The Lac signal is usually barely detectable about the baseline noise, but in certain pathologic conditions (e.g., ischemia or inflammation), the signal will increase significantly. The most important resonant peak is NAA because it is localized within neurons and axons; therefore, making it a commonly accepted marker for axonal integrity [33, 34]. In general, the NAA

signal is lower in MS lesions (regardless of whether the type of MS is RR, SP or PP) as compared to normal WM of control subjects. It can be measured in MS lesions, NAWM and whole brain [2].

Via NAA, MRS is able to provide an index of neuronal damage [35], but unfortunately it has a few additional challenges compared to conventional MRI. First, brain tissue metabolites exist in millimolar concentration. To be detected, minimum metabolite concentrations must typically be between 0.5 - 1.0 mM [36]. This desired signal can be masked by signal from water in the brain and surrounding structures. Because of the low concentration, the signal-to-noise ratio (SNR) and image resolution of MRSI is much lower than in water-based images. This problem is minimized by suppressing stronger signals or inhibiting them from being excited. Secondly, spectra are typically acquired from single or multiple volumes (voxels) in localized areas. Although voxel arrays (images) can be attained by longer scan times, there is the trade-off with SNR. Lastly, MRS is most powerful when the spectra can be quantified, but accurate absolute quantification is difficult to perform. Therefore, relative quantification of one metabolite to another metabolite, which hopefully remains constant, is more widely performed due to its relative ease [37].

Diffusion-Weighted and Diffusion Tensor Imaging

Diffusion imaging is based on the microscopic water environment and is sensitive to the movement of water molecules over short distances. Free, or bulk, water is capable of movement in all directions and is characterized by *isotropic* diffusion. Highly organized tissue contain biological barriers such as cell membranes, organelles and microtubules which cause the movement of water to be restricted in one or more directions making diffusion *anisotropic*. Since the diffusion behaviour of brain water is similar to that of bulk water, the term *apparent diffusion coefficient* (ADC) is used to indicate the mean squared displacement per unit time due to the restriction caused by these biological barriers [38]. Diffusion coefficients are measured with a minimum of two measurements: one with diffusion weighting and another without. A measured reduction in diffusion anisotropy could indicate a breakdown in structure. Since anisotropy cannot be fully described by a single

scalar diffusion coefficient D, a tensor, $\underline{\mathbf{D}}$, is used to describe molecular movement along the principal axes of the scanner (x, y, z) and allows diffusional anisotropy effects to be fully characterized and exploited, thereby providing the intricacies of tissue microstructure.

Although the relationship between diffusion anisotropy measurements and water in myelin and axons is not well defined, the breakdown of the barriers and increases in extracellular space permit water molecules to diffuse more freely, which causes an increase in ADC [27, 39]. MR studies of diffusion in MS are a promising way to assess the structural integrity of WM tracts. Furthermore, water diffusitivity measurements are scanner independent since its value reflects the tissue's physical properties, unlike measured values like T_1 and T_2 which are field strength dependent MR parameters. Drawbacks to diffusion imaging are sensitivity to subject motion and generally low spatial resolution.

Magnetization Transfer

Mobile protons, such as bulk water, have relaxation times long enough ($T_2 > \sim 10$ ms) to be measured by conventional MR techniques which have minimum TE of a few milliseconds. Semi-solid macromolecules, such as the structural component of brain tissue like myelin, are not directly visualized by conventional MR due to their extremely short T_2 relaxation times ($T_2 < \sim 100$ μs) relative to TE. Magnetization transfer (MT) is a technique that is able to indirectly acquire information from these macromolecular protons by measuring the signal from mobile protons which are affected by exchange of magnetization between the "visible" (mobile) and "invisible" (semi-solid) components [40].

These two distinct pools are referred to as either *free* (mobile) or *restricted* (semi-solid) due to their different environments (correlation times). The free protons, characterized by a narrow Larmor spectrum ($< \sim 100$ Hz), experience fast rotational and translational motion. The restricted protons, characterized by a broader Larmor spectrum ($> \sim 10$ kHz), experience slower rotational and translational motion. In a heterogeneous biological environment, both free and restricted pools exist and interact by exchanging magnetization. A simple 2-pool model (binary spin-bath model) is often used to model the MT effects between the free and restricted protons [41]. The pools are coupled together where forward and reverse

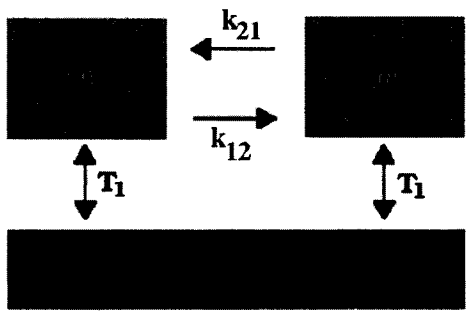

Figure 2.6: The 2-pool model illustrating MT effects. Upon saturation, the magnetization in the semi-solid pool is lost. Cross-relaxation effects with the mobile pool results in an increase in semi-solid signal (not MR visible) and a decrease in the mobile signal which can be measured with MR. While magnetization is transferred between the two pools, both pools continue to relax longitudinally according to their respective T_1 rates. (From [43].)

cross-relaxation rates, dominated by dipole-dipole interactions, can be modelled by a pair of coupled Bloch equations [42]. By perturbing the restricted pool by selectively saturating it several kHz off resonance, the effect on the mobile pool is observed as a result of cross-relaxation. The magnetization from the free pool is exchanged with the restricted pool while both pools undergo T_1 relaxation. The relative population size, respective pool relaxation times, and the MT rate affect the decrease in the mobile pool signal available for imaging. Figure 2.6 illustrates the 2-pool model.

The effect of MT is often calculated as the magnetization transfer ratio (MTR) where two sets of MR images are acquired, one with and one without a saturation pulse. The MTR represents the fractional signal loss as a result of complete or partial saturation of the restricted proton pool and is calculated as

$$MTR = \frac{M_o - M_{sat}}{M_o} \times 100\%. \tag{2.11}$$

Values range from near zero in CSF and blood up to $\geq$50% in tissue with a high proportion of restricted protons such as WM. The resulting magnetization transfer contrast (MTC), essentially reflects the concentration of macromolecular protons (either a reduction in the macromolecule pool or an increase in the water pool).

The measure of MTR is sensitive to changes in macromolecular structures and is increasingly being used in MS research due to high reproducibility, as well as being time effective (e.g., a whole brain scan with isotropic resolution of 1 mm^3 takes $\sim$ 15 minutes). However, it must be taken into account that the MTR is not an absolute measure of WM myelin content and is highly dependent on the experimental parameters (e.g., frequency offset and effective power of the saturating pulse). As a result, various studies acquiring brain MT measurements in a variety of ways have dissimilar absolute MTR values [44].

The MT exchange in myelinated WM is significantly higher than in non-myelinated WM or GM because myelin has a higher concentration of macromolecules. Studies have shown that patients with MS have lower MTRs than healthy subjects, even in so-called NAWM and normal appearing GM (NAGM). Large MTR reductions correspond to extensive demyelination with lesions showing varying degrees of myelin loss [45–47]. The myelin to axonal structure ratio is about 20:1; therefore, it is appropriate to assume that the measured MT effect is between the water pools and myelin (and not axons).

Although the MTR is quantitative in the sense it can be reproduced, compared and repeated, the value reflects the amount of MT as well as its dependence on a combination of experimental parameters. Quantitative MT (qMT) techniques yield intrinsic properties such as the respective T_1 and T_2 values and pool sizes of the mobile and restricted pools, as well as their first order MT exchange rates [48]. This technique, developed *in vitro* by Henkelman *et al.* [41] and *in vivo* by Sled and Pike [49], is more rigourous and can increase the specificity in interpreting MS pathology. Quantitative MT imaging (qMTI) is still limited by acquisition time and complexity.

Quantitative T_2 Measurements

Unlike MT, which is based on a binary spin-bath model with all the mobile protons pooled as one, and similarly for the macromolecules, a multi-component T_2 relaxation pulse sequence is able to separate pools of water in distinct environments. Early *in vivo* T_2 relaxation studies of the brain involved a few echoes and mono-exponential fits. Due to the heterogeneous nature of neural tissue, this method is incorrect and does not truly capture

nor represent the system measured [50]. Quantitative T_2 (qT_2) acquisitions use multiple spin-echoes to measure the T_2 decay curve at short intervals over an extended period of time, resulting in a well-sampled decay curve. Multi-exponential analysis methods can then determine a corresponding T_2 distribution representing the relative size of the various mobile components at their respective relaxation times.

Multi-component T_2 relaxation measurements have been collected in various materials (e.g., brain, breast, wood, blood, muscle) and this method holds very well in resolving signals from microanatomical domains since the spin-spin relaxation depends on the local water environment. Previous *in vivo* and *in vitro* qT_2 studies in neural tissue [51–62] have observed compartmentalization of water, although the exact relationship between the T_2 and the microanatomical environments is unresolved. Analysis of the T_2 decay curve of brain exhibits multi-exponential behaviour, and quantitative measurements have generally discerned three water components based on their T_2 values. These T_2 components have been described in the following way: (i) *myelin water* (a minor short component, $T_2 \approx 15$ ms), (ii) *intra/extra-cellular (IE) water* (a major intermediate component, $T_2 \approx 80$ ms), and (iii) *CSF* (long component, $T_2 > 1$ s) [53, 55, 56, 63].

Mackay *et al.* [56, 63–68] pioneered *in vivo* qT_2 studies with applications to MS using a 32-echo single-slice acquisition (4-average, scan time ~26 min) and a modified *non-negative least squares* (NNLS) fitting algorithm to determine the T_2 distribution. In brain, the short T_2 peak is assigned as the myelin water peak and is believed to represent the water trapped between the myelin bilayers. The *myelin water fraction* (MWF) is the percentage of the total mobile signal assigned to the myelin water peak and it gives an indication of the myelin content. Whether the MWF reflects solely the amount of myelin present or also conveys information about the integrity of the myelin bilayer is uncertain. However, histology studies support the hypothesis that the short T_2 component does indeed comes from myelin water [68, 69].

The average MWF in healthy WM and GM has been reported to be 11.29 and 3.13% [63], respectively, with decreased values noted in MS subjects [46]. In WM, the MWF can range from about 7% in the minor forceps to around 18% in the internal capsules, whereas only

a few percent difference is seen across GM due to low myelin content [46, 63, 68]. Previous studies have shown prolonged T_2 in NAWM of MS patients compared to normal subjects [70–77], although not all agree [78, 79]. The method of measurements (ranging from 2 to 128 echoes) and analysis (mono- and bi- exponential), as well as reported T_2 values, varied considerably. The study by Whittall *et al.* [80] also reports prolonged $\overline{T_2}$ in NAWM which shows that T_2 relaxation analysis is capable of being a sensitive measure of subtle changes in MS. It is also common to see multi-component curve fitting applied pixel-by-pixel to produce myelin water maps (short T_2 fraction) which are useful in assessing the state of myelin in patients with WM diseases.

Compatibility of Multi-compartment Water Models with MT's 2-pool model

The 2-pool MT model does not take into account water being in different environments since it assumes the exchange between the two water pools is much faster than that between the macromolecular and water components. This is unlike multi-echo sequence studies which are able to separate the water pools (see Figure 2.7 for a more complete model describing exchange between the different reservoirs). A more complete model of water and semi-solids in brain tissue has been explored with studies combining MTR and multi-echo experiments. Gareau *et al.* [81] looked at the MTR *vs.* myelin water in experimental allergic encephalomyelitis (EAE), an experimental model of MS, and found no or little correlation. Since MTR depends on T_1, the relation between the two may have been masked. Support for the idea that water trapped between the myelin bilayers is in close contact with semi-solid lipid protons has been given by *in vivo* and *in vitro* MT-prepared multi-echo measurements [65, 82].

MT parameters for WM can be derived from a 4-pool model (Figure 2.7), but there is debate on whether a 4-pool model is necessary or if a 2-pool model is sufficient to estimate the myelin content [83–85]. The argument for a 4-pool model is simply that the known existence of water reservoirs should not be ignored. Advocates of the 2-pool model suggest that relaxation rates reflect weighted averages of individual reservoirs since these reservoirs are indistinguishable on the MT time scale. Overall, the study of MS using

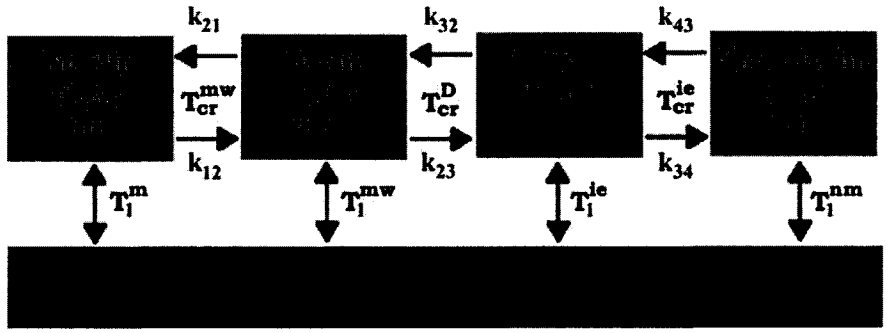

Figure 2.7: The 4-pool model illustrating magnetization exchange between various proton pools. (From [83].)

these two quantitative methods provide better insight in the interpretation of pathology. An ultimate goal is to unify the liquid/semi-solid qMT and multi-compartment water T_2 models of brain tissue, or at least clarify their relationship with each other, especially qMT's semi-solid pool fraction and qT_2's myelin water estimate.

Other Methods to Image Short T_2 Components

One of the major set-backs of the multi-echo single-slice T_2 acquisition is the long scan time required to reach a desired SNR, as well as post-processing times for myelin maps. Modifications to the acquisition include acquiring 48 echoes to better measure the short and long T_2 decay components, but this does not reduce scan times from that of the current 32-echo acquisition [86]. With the advent of higher field strengths and the corresponding SNR gains, multi-slice acquisitions at 3 T have been implemented with acquisition times similar or faster than the 1.5 T methods [87]. Jones *et al.* [66] introduced spatial filtering as a substitute for signal averaging. An anisotropic diffusion function uses the scaled gradient in each direction (relative to a parameter, which in turn depends on the standard deviation (σ) in the noise) to update each voxel's signal intensity. The anisotropic diffusion filter does not introduce a bias in the multi-echo signal intensities and as more iterations of the filter are applied, the σ for each ROI becomes lower. Therefore, instead of spending time acquiring more signal averages, a number of iterations can be applied to the data to

create myelin maps with smoothly changing intensities instead of maps with noise "holes". Although local σ decreases with filtering, a balance is required since "over-filtering" causes maps to be iso-intense, thereby losing the sensitivity to detect focal myelin abnomalities. Compared to the UBC-pioneered 4-average, unfiltered data, results showed that 2-average, filtered data was not as robust since its MWF histogram was broader. Simulated data proved that these differences were attributed to low SNR. Due to stringent SNR requirements for robust NNLS fitting, the spatial filtering technique cannot be used with 2-average data to produce equally robust MWFs as that of unfiltered 4-average data. Instead, spatial filtering can be applied to 4-average data to achieve a reduction of 40% in σ, making the data similar to an 8-average scan.

The linear combination (LC) method has been used as an alternative to NNLS fitting to generate myelin maps at a fraction of the computational time [67]. With LC methods, it is possible to reduce the multi-echo dataset, allowing for multi-slice spin-echo sequences acquired in shorter times with similar SNR [88, 89]. Myelin water images are generated by linearly combining images from the multi-echo data set. LC weights are chosen to filter out specific T_2 species without specifically estimating their T_2. A fractional myelin map is achieved by dividing the short-T_2 filtered image by a uniform filtered image. Jones found that the MWFs and variability from 32-echo data filtered via LC methods is similar to that from NNLS, although marginally farther from expected values than when using NNLS. Vidarsson *et al.* [88] optimized echo times for SNR efficiency for a multi-slice, few-echoes sequence. The 3-echo filter was shown to produce good myelin images within a mere 5 minutes of scan time. Results from myelin images compare well with literature, although the repeatability of the filter needs to be verified. LC filters have also been combined with a balanced steady-state free-precession (SSFP) multiple flip angle sequence. SSFP sequences boast high SNR efficiency, but CSF appears very bright and SSFP is more sensitive to artifacts. Flip angle optimization may also improve imaging time just like echo-time optimization with spin-echo myelin water imaging [90].

Ultra-short TE (UTE) is another approach to image short-T_2 components. For short T_2 components which constitute the minority of the mobile signal, UTE with robust long-T_2

suppression pulses enable tissue like myelin to be better discerned [91, 92]. This, as well as the other methods aforementioned, are innovative ways to increase SNR while decreasing scan time with optimized sequences and/or more efficient post-processing.

Chapter 3

Simulations

Simulations were conducted using Matlab (The MathWorks, Natick, MA, USA) to understand the biological tissue system being investigated with a multi-echo acquisition and to validate the implemented non-negative least squares (NNLS) analysis technique. Multi-echo decay curves similar to those expected *in vivo* were simulated for white and grey matter with varying levels of noise and analyzed to estimate myelin water fractions (MWFs). Analysis parameters were also adjusted to determine their effect on these reported values.

3.1 White and Grey Matter Models

The MR signal from white and grey matter was modelled as a combination of three components:

1. $T_2 = 15$ ms $\rightarrow$ myelin water (MW)
2. $T_2 = 80$ ms $\rightarrow$ intra/extracellular water (I/E water), and
3. $T_2 = 2000$ ms $\rightarrow$ cerebrospinal fluid (CSF).

Expected T_2 values and pool weightings from the literature were used to model these components with multi-exponential decay curves (see Table 3.1). The simulated tissue models were assigned a CSF weighting of 0%, although Whittall *et al.* observed CSF contamination in patients ranging from 1 - 15% (more in GM than WM, and even more in cortical GM) [50]. Normal WM and GM were modelled with 14 and 2% MWF, respec-

Table 3.1: Pool weightings (given in %) for the simulation study. One thousand different realizations were calculated with SNR 50, 100, 200, 400 and 1000 for simulated sets. The WM model was created with 14% MW and the GM model with 2% MW.

	% MW				
% CSF	2	6	10	14	18
0	✓	✓	✓	✓	✓
5	✓			✓	
10	✓			✓	
15	✓			✓	

tively. Since it is possible to get CSF contamination due to partial volume effect, the effect of CSF (with a weighting up to 15%) on the T_2 distribution was also investigated for the normal WM and GM simulations.

Tissue is heterogeneous, therefore it is expected that the relaxation times are not governed by a single value but vary over a given range. Some studies have simulated relaxation curves believed to be more representative of tissue by using Gaussian models [93–95] opposed to delta functions [50, 64, 66, 96]. In this study, all simulated decay data were created with single T_2 values for the individual tissue components.

Reflecting our data acquisition protocol, the simulated data consisted of 32 decay points spaced 10 ms apart, ranging from 10 to 320 ms. A more detailed description of the imaging protocol which the simulated data emulates is given in Section 4.1. It is well established that the main sources of noise in MR data are additive, white and Gaussian (normally distributed). This noise is present in both the real and imaginary channels of the complex image which is then normally saved as a magnitude image. As a consequence, the noise distribution in the magnitude image is Rician [97, 98]. One thousand realizations of decay curves of varying SNR levels (Gaussian noise with mean zero adding in quadrature to modelled data) with a 1^{st} echo intensity of $\approx$ 1300 (derived from preliminary *in vivo* acquisitions) were generated using

$$S(t) = \sqrt{\left(\sum_j s_j e^{\frac{t}{T_{2,j}}} + \varepsilon_{\Re}(0,\sigma)\right)^2 + \varepsilon_{\Im}(0,\sigma)^2} \tag{3.1}$$

where $\varepsilon_{\Re}(0,\sigma)$ and $\varepsilon_{\Im}(0,\sigma)$ represent the error introduced from random normally distributed noise with zero mean and standard deviation σ from the real and imaginary channels, respectively.

Relaxation curves can been analyzed by linear and non-linear methods. Examples include Provencher's CONTIN (a constrained regularization inverting method returning a continuous solution) [99, 100], Lawson and Hanson's least-distance programming [101], and linear programming approaches [102, 103]. More recently, linear combination of multi-echo data has been used in MS applications [67], sometimes incorporated with acquired echo time optimization [88]. A three- [96, 104, 105] and four- [65] pool model has also been used to fit the components. The NNLS analysis method, which is the most widely used for multi-component analysis [46, 54, 57, 59, 61, 63, 66–69, 83, 94–96, 106–111], was employed in our studies and is described in the following section.

3.2 Non-Negative Least Squares Algorithm

Multi-exponential relaxation processes can be described by the Fredholm integral equation of the first kind

$$y(t) = \int_{T_{min}}^{T_{max}} s(T)e^{-t/T}dT \tag{3.2}$$

where $s(T)$ corresponds to the amplitude of the component at T for values between T_{min} and T_{max} which are chosen to contain the expected T of the system. A sampled T_2 decay curve, y_i, can be described by the general equation

$$y(t_i) = \sum_{j}^{M} s(T_{2,j})e^{-t_i/T_{2,j}} \qquad i = 1,2,...,N \tag{3.3}$$

where N discrete data points are collected at times t_i with amplitude s_j at relaxation times $T_{2,j}$. It is possible for CPMG sequences to have baseline shifts as a results of electronic offsets or non-ideal refocusing pulses, to name a few, which can be accounted for by simply adding a constant term to Equation 3.3. It has been shown that large negative offsets results

in very large misfits due to the inability of NNLS to fit negative data [112]. Tolerable fits, close to the expected value, are seen for positive offsets. By extending the upper bound of the solution set, the overall misfit decreases as the offset value is better modelled by the larger values [112]. Very few studies seem to incorporate a baseline offset term in their analysis.

Baseline offsets are potential problems but can be minimized at data acquisition by using *phase cycling* (i.e., changing the phase of the RF pulse within or between a sequence to produce transverse magnetization with a different orientation in the rotating reference frame). An alternate method is *RF chopping* which requires an even number of signal averages. The phases of the RF excitation pulses for each signal average can be offset by 180° which results in signal with alternating +/− signal, each with the same offset. By subtracting all the signal averages with one phase from those with the alternate phase, the DC offset is eliminated and SNR improved [113].

The NNLS algorithm is used to transform the discrete T_2 decay curve (amplitude *vs.* time) into a discrete T_2 distribution $s(T_{2,j})$ (component amplitude *vs.* T_2). The least-squares (LS) T_2 spectrum typically consists of a few isolated delta functions over M possible T_2 times and is generated by the linear inversion of the exponential decay data set. The ideal bounds of $T_{2,j}$ is about half the smallest measured T_2 relaxation time to a few times the largest time in order to span an adequate range of solutions without loss of in precision [57, 95]. Unlike non-linear inversion techniques, NNLS is not an iterative process and does not require any *a priori* assumptions of the number of components or the relaxation times, and it does not have the pitfalls of non-convergence or convergence to only a local minimum [64, 95].

3.2.1 Regularized NNLS Solutions

Due to noise in the measured data, the proposed LS solution will not exactly reflect the measured data. The misfit parameter, χ^2, quantifies the difference in the measured data (y_i) and constructed data (y_i^p) from the proposed model $s(T)$, and is calculated as

$$\chi^2 = \sum_i^N \frac{(y_i - y_i^p)^2}{\sigma_i^2}. \tag{3.4}$$

The preferred solution is when the condition $\chi^2 \approx N$ is satisfied (i.e., each datum is approximately misfit by one standard deviation). The misfit's standard deviation is $\sqrt{2N}$, and spectra are classified as acceptable if χ^2 lies less than one or two standard deviations above the expected value [112]. If $\chi^2 \ll N$, the proposed solution is too closely fit to the data and the distribution will contain artifacts from noise. If $\chi^2 \gg N$, spectral information is lost due to insufficiently fitted data [64].

The NNLS distribution is smoothed (regularized) in order to diminish spurious peaks as a result of fitting to noise, as well as to adapt the NNLS solution to a more continuous model which is more representative of biological systems. The regularized solution is a result of minimizing Equation 3.5 (i.e., the misfit parameter as well as another constraint). Possible constraints may be the energy of the spectrum derivative (1^{st} derivative) or the energy of the spectrum curvature (2^{nd} derivative), or more commonly used, the "energy" of the solution (second term in Equation 3.5) [64].

$$\chi^2 + \mu \sum_j^M s_j (T_j)^2 \tag{3.5}$$

The value of the regularizor, μ, controls the amount of smoothing and causes χ^2 to increase monotonically with it. The LS solution corresponds to $\mu = 0$ and regularized solutions have $\mu > 0$, with larger values resulting in broader distributions and, therefore, poorer peak resolution. Figure 3.1 shows a sample multi-component decay curve and its corresponding unregularized LS-solution. Also plotted with the LS-solution are two regularized T_2 distributions (the red distribution has little smoothing so it closely follows the unregularized solution, the green distribution has more smoothing as seen by the broader peaks). A detailed implementation of Lawson and Hanson's NNLS [101] is given by Whittall and Mackay [64].

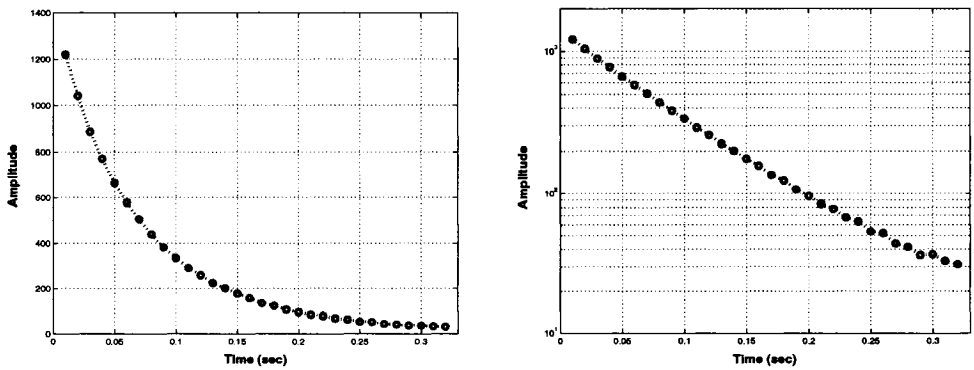

(a) (b)

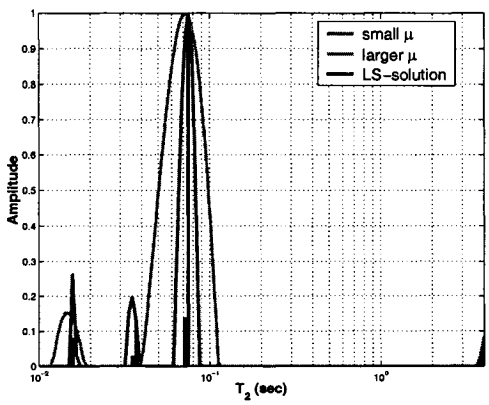

(c)

Figure 3.1: A sample multi-component T_2 decay curve drawn on a (*a*) linear and (*b*) logarithmic scale, and (*c*) its corresponding unregularized and regularized T_2 distributions. The blue bars represent the unregularized LS-solution while the red (small μ) and green (larger μ) lines correspond to increasingly smoother distributions.

Graham *et al.* [94] ran Monte Carlo simulations to assess the feasibility of multi-component T_2 relaxation analysis for *in vivo* data. The NNLS algorithm was used to produce T_2 distributions in simulated data modelling white matter, fast twitch muscle, and breast tissue. Two variations of the NNLS algorithm were tested to determine which was most appropriate for *in vivo* data with low SNR.

1. Choose μ as described by Whittall *et al.* [64] but reject any proposed data set with misfits larger than one standard deviation of the expected value (N is the number of

measured data points and $0 < \alpha < 1$):

$$\chi^2 = N + \alpha\sqrt{2N}. \tag{3.6}$$

2. Accept all solutions and regularize using the LS-based constraint where the misfit is allowed to increase by some chosen percentage p relative to the misfit χ^2_{min} from the LS solution:

$$\chi^2 = (\frac{100\% + p}{100\%})\,\chi^2_{min}. \tag{3.7}$$

Their study showed that the second method faired better than the first. The LS-based constraint method provided enhanced admissibility (i.e., percentage of distributions with the correct number of components, specifically the calculated T_2 value, relative pool weighting, peak width, and $\overline{T_2}$) for estimating T_2 components within specified accuracy. Although unregularized LS solutions gives enhanced admissibility at low SNR, allowing χ^2 to increase even by $\leq 1\%$ provided admissibilities $\geq 90\%$ and decreased component estimate uncertainties.

A recommended way to fit the data is by using weighted LS which is done by dividing each data point by its estimated noise prior to fitting [53, 64]. By doing so, the desired misfit can be achieved by changing μ since the noise estimate gives $\chi^2 \ll N$. Saab *et al.* found that following the criteria $\chi^2 \approx N$ may be counter-productive for experiments with high SNR and N and instead used phantom studies to find optimal values of μ which were then used for *in vivo* studies [114]. As shown by Graham *et al.*, the LS-based constraint method is better suited for the *in vivo* studies similar to those carried out in this project. Therefore, simulated data were analyzed with set ranges of allowed χ^2 increases as is commonly used in T_2 relaxometry [46, 63, 65–68, 109].

3.2.2 NNLS Analysis Parameters

There are several parameters that must be considered when analyzing with NNLS, namely the number of T_2 values, how they are spaced, and over what range they span, as well as

the type and strength of regularization. The following briefly discusses these parameters, and Table 3.2 summarizes the values used in the simulations. The parameter selection was based on relatively recent doctoral work done by Jones [115] which was subsequently published [66, 67].

Table 3.2: Simulation analysis parameters.

Parameters	Values
# T_2	120
T_2 range	10 ms - 4 s
Regularization type	Minimization of energy
Allowed χ^2 increase †	0 - 0.5, 0.5 - 1, 1 - 1.5, 2 - 2.5, *or* 2 - 2.5%
MWF range‡	10 - 40, 10 - 50 ms, *or* manual peak separation*

† Based on χ^2 of the unregularized LS solution

‡ Does not affect actual decomposition of decay curve

* Not investigated for simulation studies, used for select human studies

The T_2 solution First, the specified range of T_2 values must be large enough to cover all possible solutions for the system. Secondly, the number of components must be sufficient to give adequate T_2 resolution. Although a finely spaced T_2 solution set can give better precision, there is the trade-off with long computational times from the intensive data processing. There is also a limit at which the distribution does not change with increased resolution. Since MW has the shortest T_2 and is the water pool of interest in our study, a logarithmically spaced solution of 120 T_2 values between 10 - 4000 ms was chosen to allow a more precise MW distribution profile [115].

Amount of regularization Most studies using NNLS to analyze multi-compartment tissue choose to minimize the distribution's "energy". Instead of smoothing LS-solutions

by choosing some pre-determined value of μ, an alternative approach is to set an allowed range above χ^2_{min} (the misfit from the LS-solution) for χ^2 to increase by. The process is carried out by choosing some μ and generating a smooth distribution. Compare χ^2 to χ^2_{min} and adjust μ accordingly so that χ^2 falls within the allowed range. As an example, a smoothed T_2 distribution generated with a χ^2 increase of 1 - 2% would mean that $1\% < \frac{\chi^2}{\chi^2_{min}} \times 100\% < 2\%$. In our experiments, the various ranges over which χ^2_{min} were allowed to increase were 0 - 0.5%, 0.5 - 1%, ..., 2 - 2.5%. For experiments where the effect of regularization on MWF estimates was not tested, distribution were regularized by 2 - 2.5% (i.e., $1.02\chi^2_{min} < \chi^2 < 1.025\chi^2_{min}$) [66, 67].

Other factors affecting the solution Other factors affecting the solution are the initial μ and the algorithm used to arrive at the desired regularized solution. Although NNLS itself is not an iterative process, finding a constrained regularized solution requires repetitive calculations through various μ until a set condition is met. The solution may differ depending on the specifics of the algorithm (e.g., whether μ is sampled from a pre-defined vector, or whether the new μ is generated based on the previous step's value). The effect of these factors was outside the scope of this study.

3.3 Calculating Myelin Water Fraction Estimates

Typical brain tissue T_2 distributions may contain peaks corresponding to MW, I/E water, and CSF. If the distribution contained well-defined peaks consistently in the range corresponding to these aforementioned components, the assignment of the pool size (equivalent to the area under the peak) would be trivial. This is unfortunately not always the case and is described in further detail later in this chapter.

In the literature, MWF is defined as the percentage of the area under the myelin water peak (refereed publications usually specify a myelin water range of 10 - 50 ms [46, 63, 66–68]) when compared to the area of the total T_2 distribution (i.e., total water content). Since the main water peak in T_2 distributions has a tendency to vary, MW ranges were defined using a manual peak separation method or with set ranges of 10 - 40 and 10 - 50 ms to investigate how much the MWF depends on the chosen MW range[1]. The manual peak separation method assigned signal below the main (I/E water) T_2 peak to MW. In the case where the distribution below the I/E water peak was not zero-valued (i.e., the separation between the short and middle T_2 peak was not trivial), the lowest point of the distribution between the myelin water and I/E water components was assigned as the MW cut-off. The general equation for determining the MWF is therefore

$$MWF = \frac{\sum s(T_{2,MW})}{\sum s(T_2)}. \tag{3.8}$$

[1]Literature reports of MW ranges are sometimes specified as a set range (e.g., 10 - 50 ms), or stated as a maximum cut-off value (e.g., signal under 50 ms). Later in this chapter, we discuss how stated values may not correspond to actual MWF integration limits.

3.4 Simulation Results

3.4.1 NNLS Solution for Noise-free Data

Regularized solutions are based on the χ^2 misfit which only exists when the data contains noise (refer to Equation 3.4); therefore, only LS solutions can be generated for noise-free data. In theory, the NNLS solution from a noise-free decay curve should contain the exact modelled T_2 values, barring complex decay curves with closely spaced T_2 components which results in an incorrect number of peaks and peak heights. Based on the generated WM and GM decay curves, the NNLS algorithm returns very accurate T_2 components (both pool weight and T_2 value). Pool weightings were typically well within 1% of the expected value, while T_2 values had slightly larger errors (the MW pool had the largest which was no more than 4%). The discrepancies are partly due to the logarithmic spacing and number of T_2 samples in the set which may not contain the exact T_2 values the data were modelled with.

3.4.2 The Effect of SNR and Regularization

One thousand realizations of a normal WM model (T_2 = 15 ms, 14% MW weighting and T_2 = 80 ms, 84% I/E water weighting) with SNR of 50, 100, 200, 400 and 1000 were created. As seen in Figure 3.2, higher SNRs result in sharper peaks with very good peak resolution and distributions do not contain spurious long T_2 peaks. It is evident from the figure that pool weights from high SNR data can be easily determined using manual peak separation. At lower SNRs, the spilling of one peak into the other makes this method difficult.

Although MW ranges of 10 - 40 and 10 - 50 ms were chosen, the T_2 solution (given in Table 3.3) set does not contain matching values corresponding precisely to the 40 or 50 ms cut-off, thereby leaving one to use the next closest T_2. The MWF is calculated using two MW range cut-offs: 40 ms (actual T_2 of 41.0 ms) and 50 ms (actual T_2 of 50.1 ms). A third cut-off value, also closely matching the chosen 50 ms cut-off, was 47.6 ms which is the next T_2 sample below 50.1 ms. A comparison was done with these three cut-off values to see how sensitive the MWF estimate is to the set MW ranges. Figure 3.3 shows

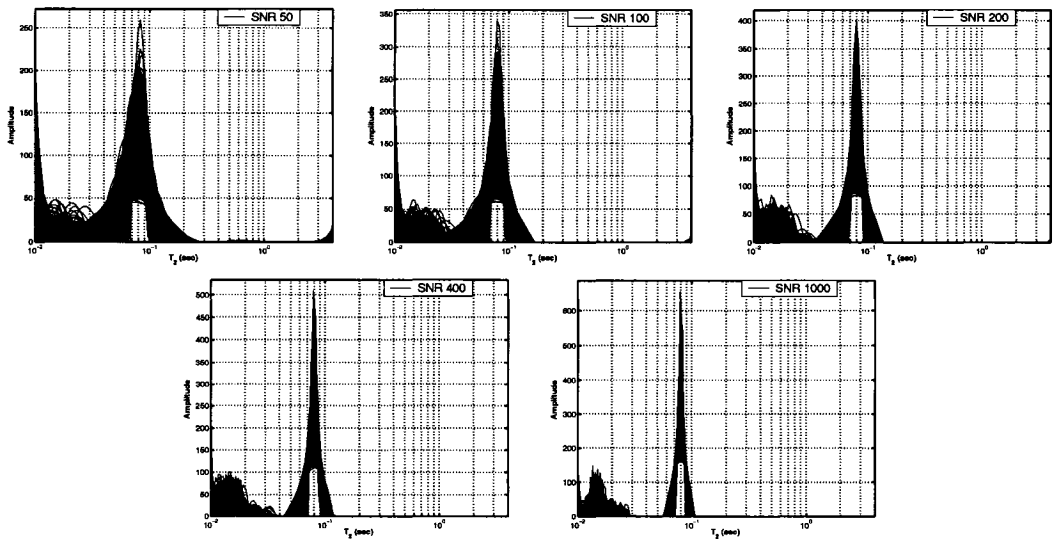

Figure 3.2: One thousand realizations of T_2 distributions of a WM model (MW: 15 ms, 14% weight, I/E water: 80 ms, 86% weight) with various SNR levels.

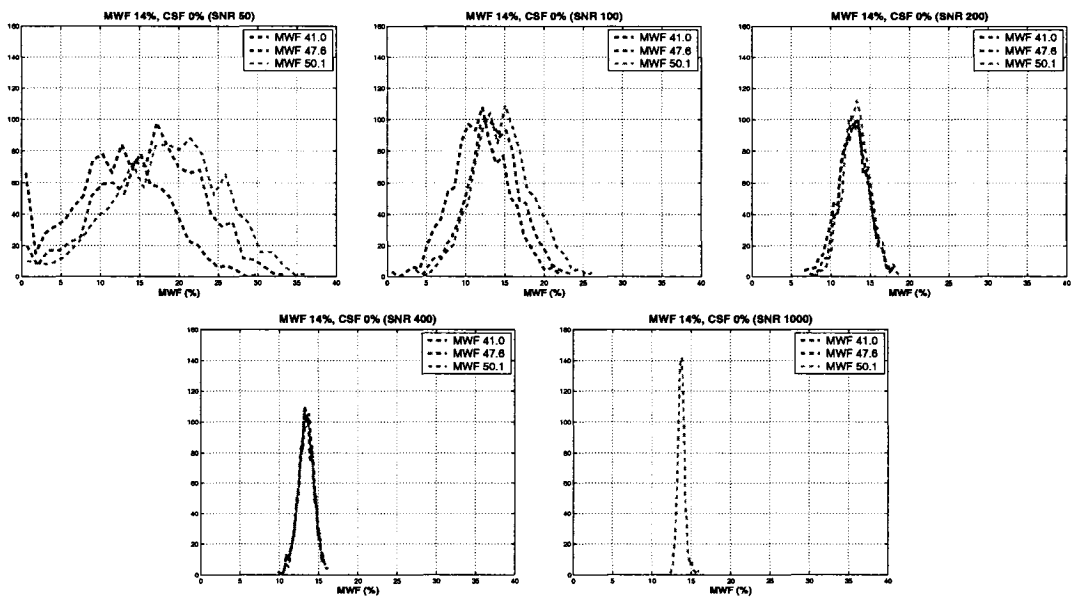

Figure 3.3: MWF histograms of WM data (varying SNR) calculated with different MW range cut-offs (actual upper integration limits of 41.0 ms, 47.6 ms, and 50.1 ms).

Table 3.3: T_2 vector (in ms) of 120 logarithmically spaced values between 10 and 4000 ms. The actual T_2 values used for the MW cut-off of 40 or 50 ms are highlighted.

10.0	18.3	33.5	61.3	112.1	205.1	375.3	686.7	1256.4	2299.0
10.5	19.2	35.2	64.4	117.9	215.7	394.7	722.1	1321.3	2417.7
11.1	20.2	37.0	67.8	124.0	226.8	415.0	759.4	1389.5	2542.5
11.6	21.3	38.9	71.2	130.4	238.5	436.5	798.6	1461.3	2673.8
12.2	22.4	**41.0**	74.9	137.1	250.9	459.0	839.9	1536.8	2811.9
12.9	23.5	43.1	78.8	144.2	263.8	482.7	883.2	1616.1	2957.1
13.5	24.8	45.3	82.9	151.6	277.4	507.6	928.8	1699.6	3109.8
14.2	26.0	**47.6**	87.1	159.5	291.8	533.8	976.8	1787.3	3270.4
15.0	27.4	**50.1**	91.6	167.7	306.8	561.4	1027.3	1879.6	3439.2
15.7	28.8	52.7	96.4	176.3	322.7	590.4	1080.3	1976.7	3616.8
16.5	30.3	55.4	101.4	185.5	339.3	620.9	1136.1	2078.7	3803.6
17.4	1.8	58.3	106.6	195.0	356.9	653.0	1194.7	2186.1	4000.0

MWF histograms from WM model data with varying SNR levels. For SNR = 50, the peak MWF (i.e., the most frequented MWF), from the three MW ranges disagree (the larger MW range over-estimates the MWF while the smaller MW range gives a fairly accurate value) and MWF estimates are poorly matched as seen with the wide profiles. For SNR = 100, the sharper histograms still disagree but peak MWFs are closer to the expected value. At SNR $\geq$ 200 and higher, peak MWFs $\approx$ 13.5% come into agreement and approach the expected value. The decreasing spread in MWF with increasing SNR can be attributed to the increased peak resolution resulting in decreased spilling of the main T_2 peak into the MW range. Although peak MWFs match the modelled pool weight with higher SNR, there is still some spread in estimated values. For SNR = 200, MWF ranges from 7 - 19% with $\overline{MWF} \approx 13\%$ and $\sigma \approx 3\%$.

Typical *in vivo* quantative T_2 brain images have SNR $\approx$ 200; therefore, SNR = 200 WM model data were analyzed with different allowed ranges of regularization (refer to Figure 3.4). The histograms from the three MW ranges (not shown) are almost identical and the peak MWF is stable at $\approx$ 14%. The impact of regularization on MWF is negligible as shown with MWF histograms based on the 50.1 ms MW range cut-off (see Figure 3.5). It appears that regularization with χ^2 increases between 1 - 2.5% results in similar MWF

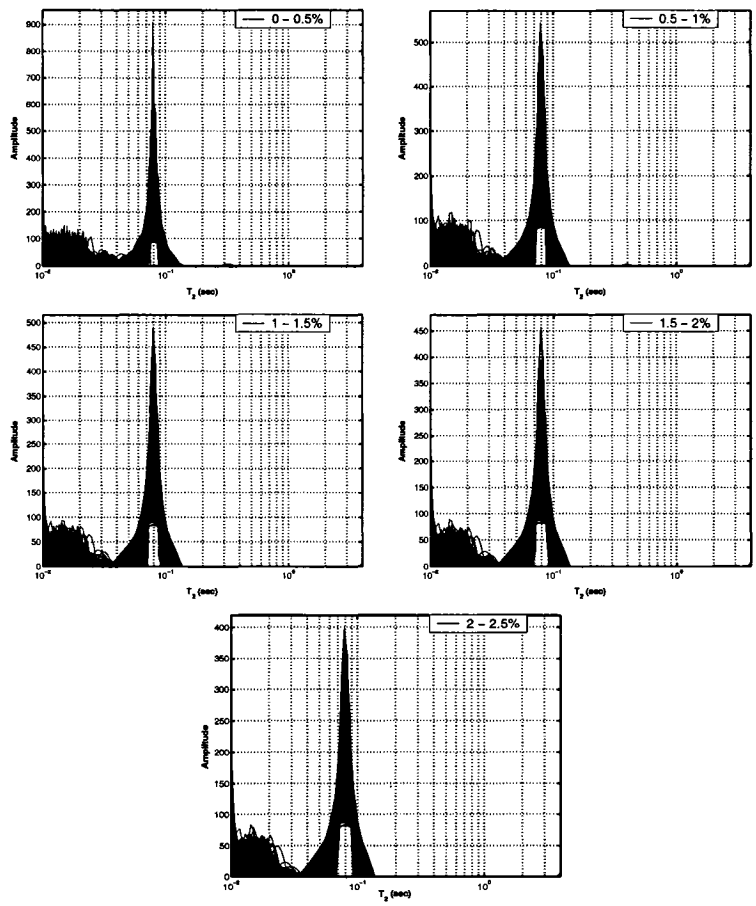

Figure 3.4: T_2 distributions from SNR = 200 WM data analyzed with various allowed ranges of regularization.

profiles which are also marginally narrower than profiles corresponding to less regularized distributions.

3.4.3 T_2 Distributions and MWFs for Varied MW Pool Weights

T_2 distributions (SNR = 200 data with various MW weights) and their corresponding MWF histograms calculated with different MW ranges are shown in Figure 3.6. Based on the histogram peaks, calculated MWF profile peaks are centred marginally below the true MW pool sizes (the modelled MW pool size of 2% is the exception where the calculated MWF is typically 0%). Furthermore, histograms calculated with different MW ranges start to

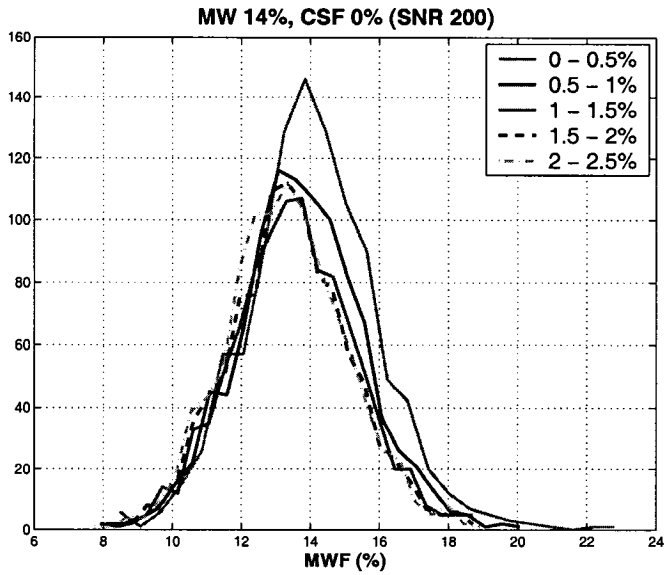

Figure 3.5: MWF histograms for SNR = 200 WM data with different amounts of regularization using the 50.1 ms MW range cut-off.

lose coherence with increased amount of MW, showing that MWFs can be more sensitive to chosen MW ranges with increased MW content.

3.4.4 The Effect of CSF Contamination

Normal WM and GM model data were constructed with varying CSF weighting from 0 - 15% with SNR = 200 (refer to Figures 3.7 and 3.8). CSF was modelled with T_2 = 2 sec, but the T_2 distribution for both WM and GM models contain a long T_2 component starting around 0.3 and 0.2 sec, respectively. There is also a tendency for signal to be assigned to the largest T_2 value (4 sec) which may be due to NNLS's inability to fit to the logarithmically spaced solution which has larger T_2 steps at high T_2. It is not likely that the T_2 at 4 sec comes about due to noise since this component is not present in distributions corresponding to 0% CSF data with the same noise level.

Figures 3.9 and 3.10 show that the MWF histograms are in fair agreement for the three MW ranges when there is no CSF component modelled in the data. With the slight presence of CSF ($\geq$ 5%), the MWF profiles deviate from each other and increases in width with

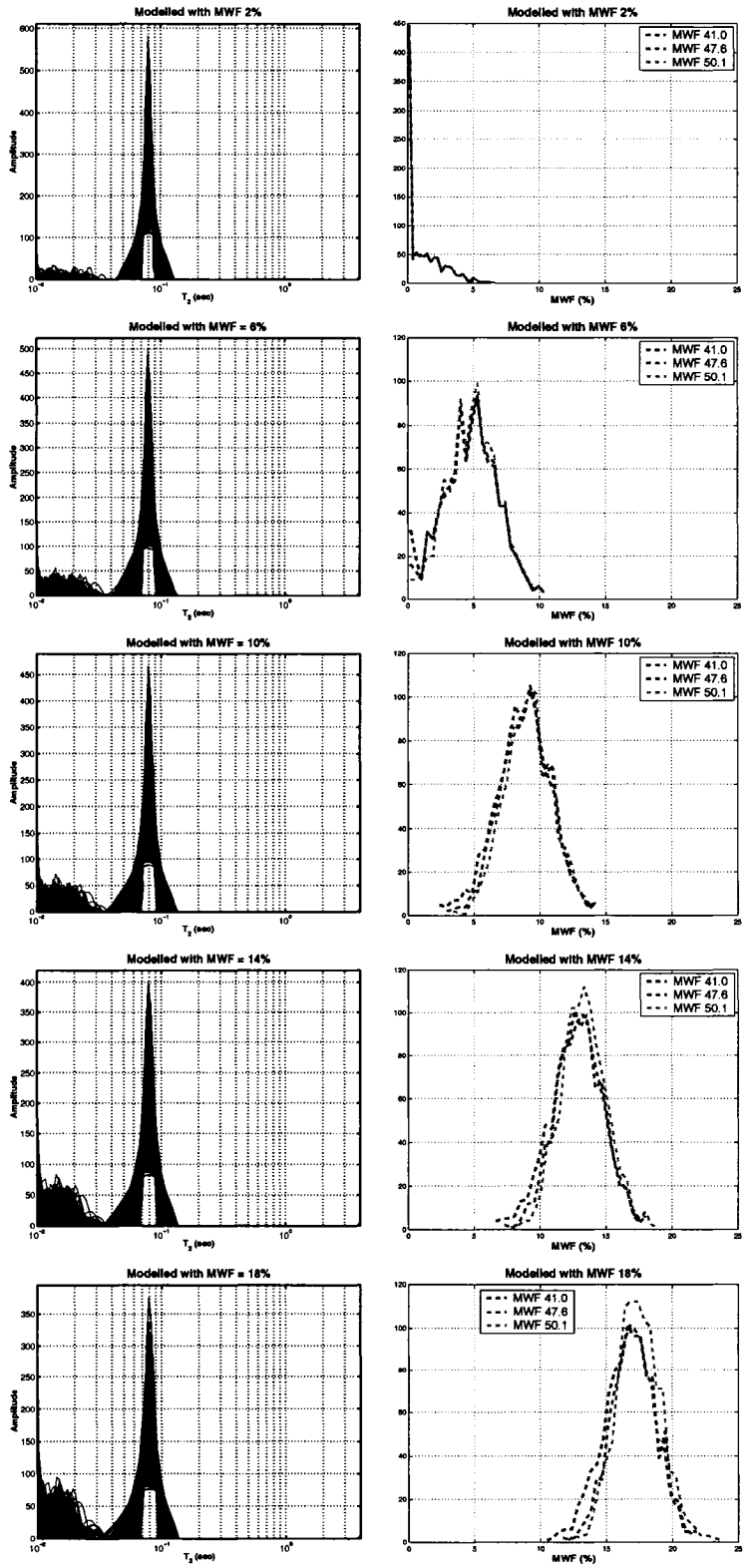

Figure 3.6: T_2 distributions and corresponding MWF histograms (actual upper integration limits of 41.0 ms, 47.6 ms, and 50.1 ms) from SNR = 200 data analyzed with 2 - 2.5% allowed increase in χ^2.

larger MW ranges, although marginal differences are seen with increased CSF content. In the normal GM model (MWF 2%, CSF up to 15%), MWF $\approx$ 1% is most frequently reported. Due to T_2 distribution variations, MWFs as high as 6, 11, and 14% can be expected (although with much smaller probability) when calculated with MW range cut-offs of 41.0, 47.6, and 50.1 ms, respectively. For normal WM model data (MWF 14%), MWF profiles with the smallest MW range have the smallest spread while increased MW ranges appears to have less symmetric profiles which favours slightly larger MWFs. For all WM profiles, the most frequented MWF lies within 1% of the true pool weight.

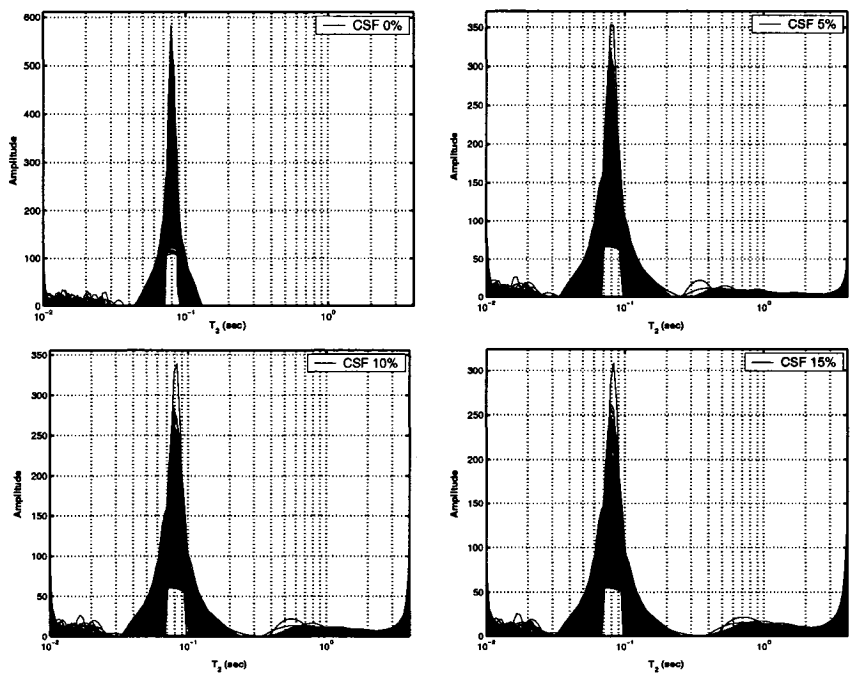

Figure 3.7: T_2 distributions from GM model data (1000 realizations, SNR = 200, 2 - 2.5% allowed χ^2 increased, MWF 2%) with varying CSF weightings.

In summary, the simulation study allowed better understanding of the type of results expected from *in vivo* data with similar SNR over a range of MWFs typically found in GM and WM. The next chapter describes the experimental imaging sequence in detail and the studies performed in human subjects.

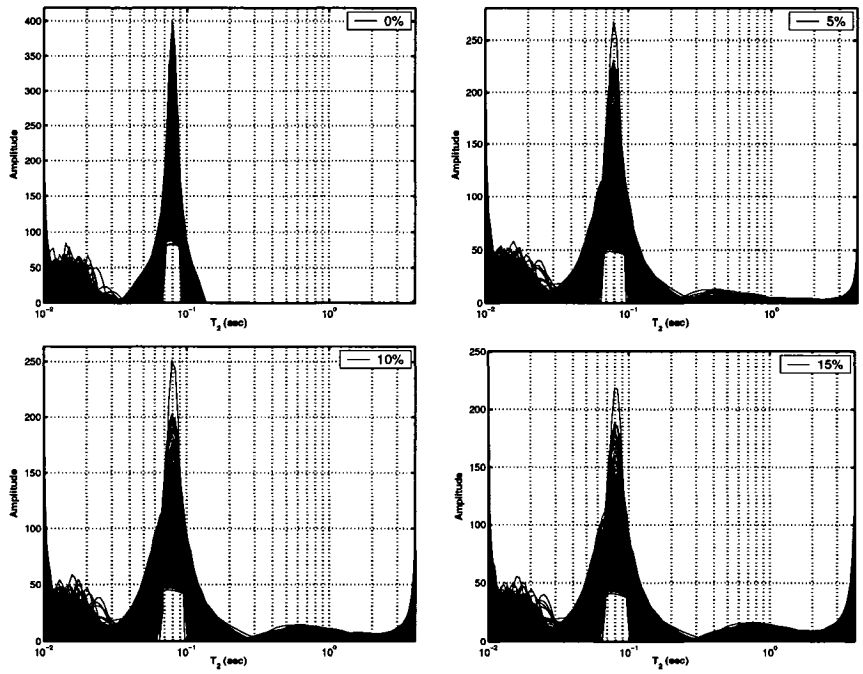

Figure 3.8: T_2 distributions from WM model data (1000 realizations, SNR = 200, 2 - 2.5% allowed χ^2 increased, MWF 14%) with varying CSF weightings.

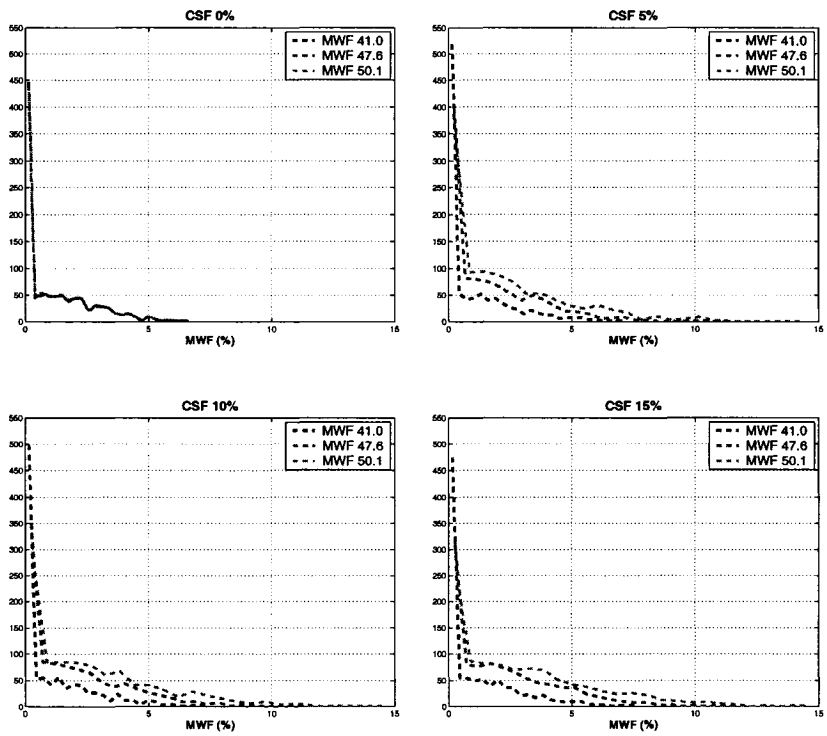

Figure 3.9: MWF histograms using different MW ranges for a SNR = 200 GM model (MWF 2%) with various amount of CSF contamination.

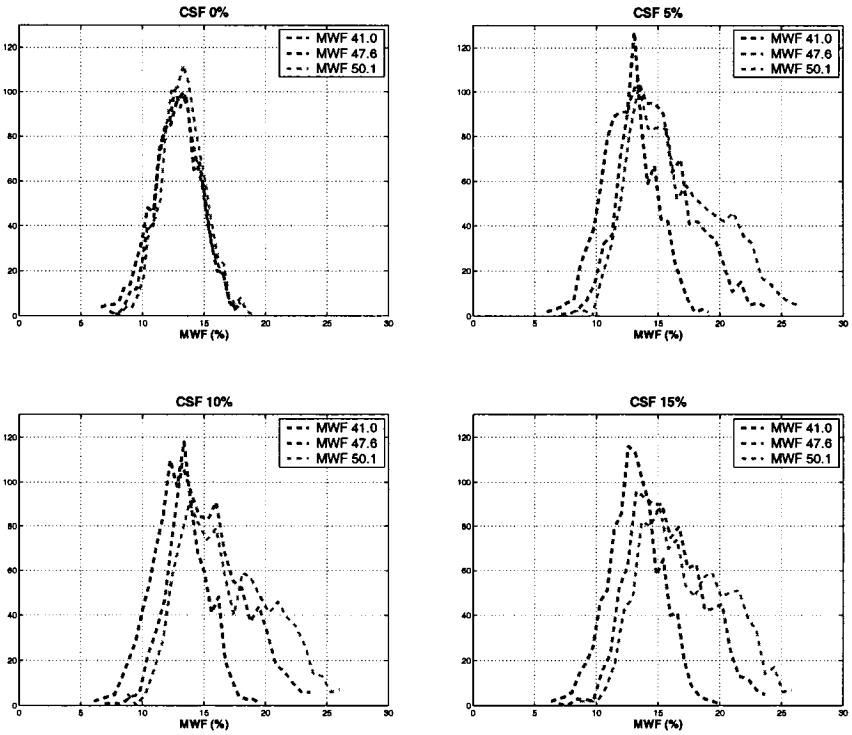

Figure 3.10: MWF histograms using different MW ranges for a SNR = 200 WM model (MWF 14%) with various amount of CSF contamination.

Chapter 4

Experimental Materials and Methods

4.1 Sequence Design

In the past, quantitative T_2 techniques were error prone and gave inconclusive and incorrect results which fueled the need for improved techniques to compensate for experimental imperfections. A single-slice multi-echo pulse sequence using composite RF pulses and gradient crusher pulses was developed by Poon and Henkelman [116].

Composite 180° pulses are used to compensate B_1 inhomogeneities or miscalibration, e.g., RF clipping. A $180°_y$ pulse is equivalent to a $90°_x$ - $180°_y$ - $90°_x$ composite pulse where any small errors in the 180° pulse will constitute very minute second-order effects. As an example, if the $90°_x$ pulse is clipped (i.e., short of producing the expected $90°_x$ pulse), the magnetization vector will be rotated by $\theta < 90°$ to somewhere above the *xy*-plane. The $180°_y$ will then translate the magnetization vector to a point equally distant below the *xy*-plane at which point another short $90°_x$ pulse would rotate the vector by the same θ down to the negative *z*-axis [26]. Poon and Henkelman proposed a better designed 180° RF pulse, referred to as Version S, which is immune to a broad range of field variations and compensates for refocusing pulse imperfections and field inhomogeneities. Although Levitt and Freeman's 90_0-180_{90}-90_0 composite pulse is insensitive to B_1 inhomogeneity, simulated comparisons of the section profile for Levitt and Freeman's composite pulse and

Version S shows that the latter has better homogeneity across larger B_1 offsets while the former fairs better across a slightly larger B_0 range.

Besides an improved RF pulse, a modified spoiler gradient scheme was implemented as an effective technique for artifact suppression to counter-balance the fractional signal loss. Spurious echoes are generated from pulse imperfections in multi-echo sequences, leading to image artifacts. Any spurious contributions to each echo can be eliminated by bracketing 180° refocusing pulses with balanced spoiler gradients. Poon and Henkelman's [116] proposed gradient scheme has the strongest spoiler gradient pair applied to the first refocusing pulse with each subsequent pair decreasing in strength and alternating in sign (i.e., the weaker spoiler gradients correspond to weaker echo amplitudes).

The most established *in vivo* multi-component T_2 decay acquisition has been developed at UBC with the first published paper in 1994 [56] demonstrating *in vivo* brain tissue multi-compartment T_2 measurements. The acquisition is a modified CPMG sequence consisting of a slice-selective 90° pulse followed by 32 180° composite pulses flanked by decreasing crusher gradients with alternating sign as proposed by Poon and Henkelman (refer to Figure 4.1). Since then, there have been many publications using this technique for *in vivo* [46, 50, 63, 65–68, 80, 117] and *in vitro* [69, 118] work in brain and other tissue. Initial experiments [56] were carried out with 32 echoes, TE = 15 ms, TR = 3 s, slice thickness of 5 or 10 mm, 2 to 8 averages, FOV 220 × 220 mm^2, matrix size 256 × 128. Subsequent experiments [46, 63, 65–69, 117] were with TE = 10 ms in order to better sample the decay curve, as well as 5 mm slice thickness and 4 signal averages to minimize partial voluming and to maintain a high SNR necessary to discern multiple components [95].

Given that typical 1.5 T clinical scanner offsets for B_0 and B_1 are 50 - 100 Hz and 10 - 20%, respectively, the $90°_x$ - $180°_y$ - $90°_x$ composite pulse was implemented in our pulse sequence (Figure 4.1) since sensitivity profiles were within tolerable ranges. Besides suppressing artifacts during acquisition, post-acquisition corrections for B_1 and B_0 errors can be applied to data sets as previously demonstrated by Sled [49] on mono-exponential T_2 fits. These corrections require B_0 and B_1 field mapping and were not incorporated in our multi-exponential fit experiment.

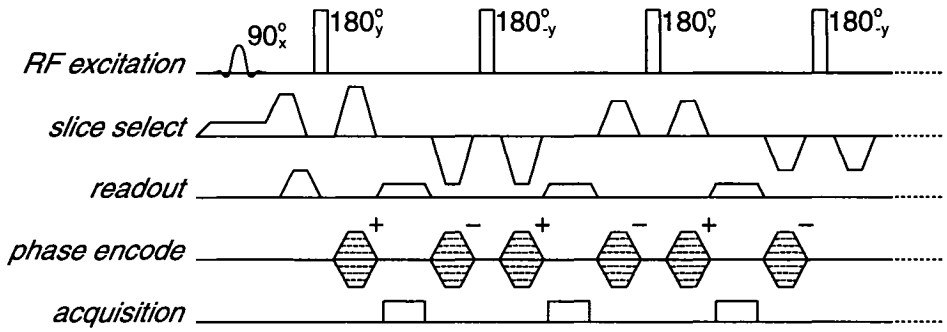

Figure 4.1: Schematic of the 32-echo spin-echo sequence for multi-component T_2 quantification (from [49]). The 180° pulses employed are $90°_x$ - $180°_y$ - $90°_x$ composite pulses.

4.1.1 qT_2 Protocols

The current standardized UBC qT_2 imaging protocol[1] has an SNR of ~200 with voxel dimensions 0.86 × 1.72 × 5.0 mm^3 and a scan time of approximately 26 minutes. qT_2 data is also collected at the MNI as a part of the MNI's qMTI protocol. The motivation for the MNI protocol was to be able to quickly acquire qT_2 data but with comparable SNR. For MNI-implemented sequences, phase cycling was used on every pair of averaged acquisitions to minimize baseline offsets. The resulting MNI protocol has similar SNR to the UBC protocol's, but the most notable difference is the resolution (2.0 × 2.0 × 7.0 mm^3) and scan time (~4 min). Table 4.1 summarizes the UBC and MNI protocols, and Fig. 4.2 compares sample 5^{th} echo images from each protocol.

[1]Throughout the thesis, the terms **UBC protocol** (also referred to as **Protocol 1**) and **MNI protocol** (also referred to as **Protocol 2**) are used. They represent the multi-echo single-slice T_2 protocols developed on 1.5 T scanners at the **University of British Columbia (UBC)** and the **Montreal Neurological Institute (MNI)**, respectively.

Table 4.1: Comparison of the UBC (Protocol 1) and MNI (Protocol 2) protocols.

	UBC (Protocol 1)	**MNI** (Protocol 2)
# echoes	32	32
TE (ms)	10	10
TR (ms)	3000	2000
Matrix	256 × 128	128 × 96
FOV (mm × mm)	220 × 220	256 × 192
Thickness (mm)	5	7
In-plane resolution (mm × mm)	0.86 × 1.72	2 × 2
No. averages	4	1
Scan time (min)	~26	~4

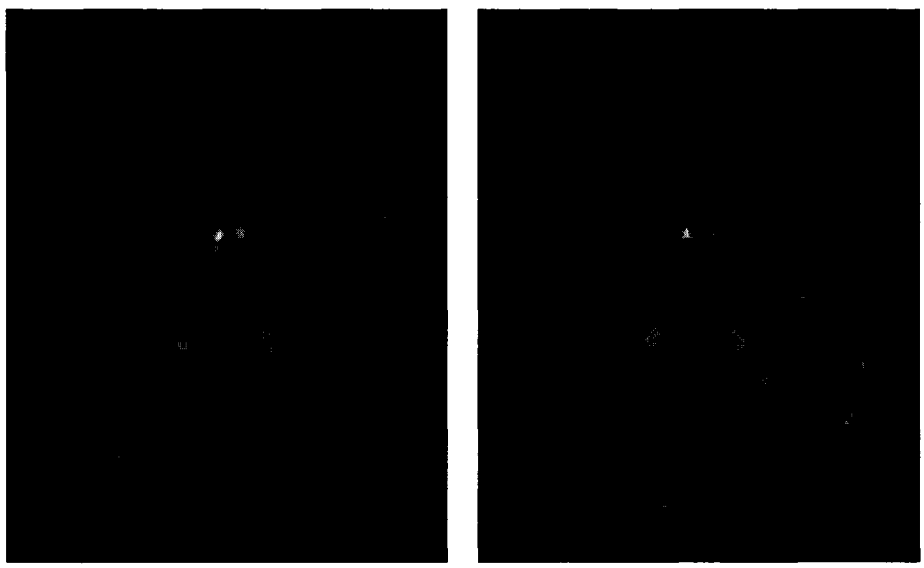

UBC
(Protocol 1)

(a)

MNI
(Protocol 2)

(b)

Figure 4.2: Comparison of sample 5^{th} echo images acquired with the (*a*) UBC and (*b*) MNI protocol. Note: images have been re-sized for comparison purposes, and window and levels altered.

4.2 Human Studies

This section describes the various studies performed *in vivo*. Data collected at the MNI were acquired with a 1.5 T Siemens Sonata (Siemens Medical Systems, Erlangen, Germany) using the standard quadrature head coil. Data from UBC were collected on a 1.5 T GE Horizon Signa (General Electric Medical Systems, Milwaukee, WI, USA) also with a quadrature head coil. All subjects were healthy volunteers who gave informed consent. Experiments fell under the quantitative MTI protocol ethics approval which was obtained from the MNI Research Ethics Board (see Appendix A).

Acquired images were of a single slice positioned to pass through the thickest part of the genu and splenium of the corpus callosum (refer to Figure 4.3a). The genu and splenium of the corpus callosum and the major and minor forceps were selected as WM regions of interest (ROIs) for analysis in the slice. The thalamus and head of the caudate nucleus were selected as GM ROIs in the slice. All ROIs were conservatively hand drawn (refer to Figure 4.3b) to minimize any contamination from artifacts or unwanted tissue from partial voluming. If a high resolution anatomical image of the subject was available, ROIs were registered to it to verify minimal partial voluming.

To generate a regularized NNLS T_2 distribution, an estimate of the σ of the image noise is required. This value was determined from the average signal ($\bar{z}$) from an artifact-free background ROI in the 1^{st} echo (see Figure 4.3c) using the relationship [22]

$$\sigma = \bar{z}\sqrt{\frac{2}{\pi}} \tag{4.1}$$

which was used for all ROIs calculated in that image. The value σ was not determined from individual ROIs because signal variations are not purely from noise but include tissue heterogeneity as well as field inhomogeneities (typical 1.5 T clinical imaging has B_0 frequency offsets of 50 - 100 Hz and B_1 variation of 10 - 20%). The SNR, defined as the ratio of the signal to the standard deviation of the noise, was determined using the average brain signal (Figure 4.3d) from the 1^{st} echo and σ from Equation 4.1.

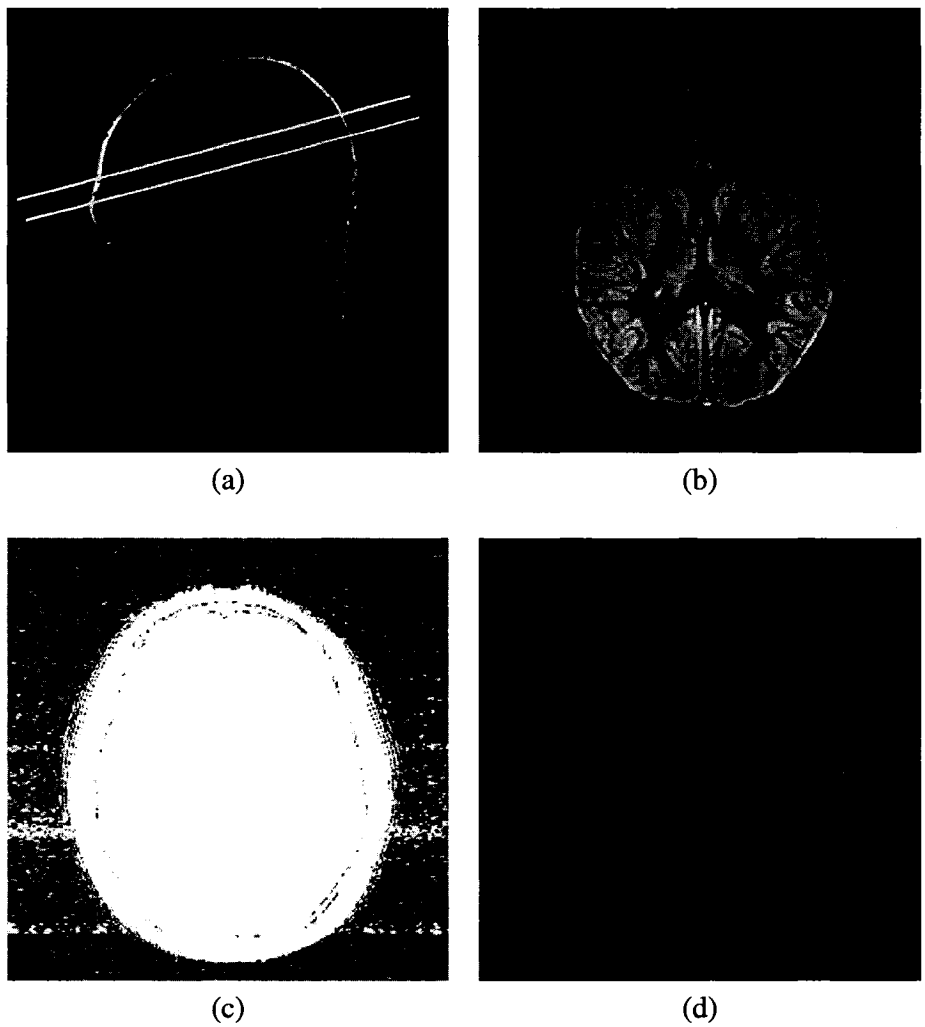

Figure 4.3: (*a*) A side-view of the single-slice volume acquired in the human studies which passes through the genu and splenium of the corpus callosum. (*b*) An example of the various WM (genu and splenium of the corpus callosum, and major and minor forceps) and GM (head of the caudate nucleus and thalamus) ROIs drawn conservatively to avoid partial volume effects. (*c*) An example of a background ROI drawn in an artifact-free region outside the subject in air for calculating the noise in images. (*d*) An example of a brain ROI used to calculate SNR.

All ROI analysis was carried out with the "average-invert" method where signal from all voxels in an ROI are averaged and then fed into the NNLS algorithm for MWF calculations as described in Section 3.3. The opposite approach, "invert-average", is to analyze individual voxels and then average the calculated MWFs. The latter method has lower SNR and therefore is not as robust as the "average-invert" method. Myelin water maps were generated by calculating MWFs on a voxel-by-voxel basis. No spatial smoothing or volume averaging was carried out to maintain image resolution. Maps were plotted as the logarithm of the MWF since this allows the greyscale to be better distributed than a linear scale over the MWF range of interest ($< 30\%$) [56, 63].

4.2.1 Cross-site Comparison

The cross-site reproducibility of the T_2-based MWF acquisition and analysis needs to be established in order to be useful in multi-centre trials. In this study, we collected and analyzed data at two sites (UBC and MNI) and compared T_2 distributions and MWF estimates in various WM and GM ROIs in healthy brain. Protocol 1, developed at UBC, has SNR $\approx$ 200 and has been used extensively in a number of studies [46, 56, 63, 66, 68, 117]. Protocol 2, developed at the MNI, has similar SNR to Protocol 1 but with decreased scan time and spatial resolution (refer to Figure 4.2). Protocol 1 was evaluated at both sites, while Protocol 2 was only evaluated at the MNI. All data were collected on the same slice of the same healthy subject (female, age 25 years).

Table 4.2: Summary of the protocol acquisitions and analysis carried out for the cross-site reproducibility study. Select data sets were analyzed with different MW ranges of upper integration limits of 41.0, 47.6 and 50.1 ms, and using maual peak separation.

	Acquired at UBC		**Acquired at MNI**		
Protocol	*1*		*1*		*2*
Analyzed at	UBC	MNI	UBC	MNI	MNI
MW range	10 - 41.0 10 - 47.6 10 - 50.1	10 - 47.6	10 - 41.0 10 - 47.6 10 - 50.1	10 - 47.6	10 - 41.0, 10 - 47.6, 10 - 50.1, and manual peak separation

For the purpose of verifying that the MNI's NNLS algorithm implementation was consistent with the UBC implementation, select data sets were analyzed by both UBC and MNI. To minimize error introduced by different investigators outlining ROIs, the same person drew ROIs on all data sets. ROIs drawn on different data sets were similar in dimension and anatomical location but the number of voxels were not precisely matched. Analysis parameters and criteria were matched for analysis carried out at both sites (parameters used are outlined in Table 3.2). T_2 distributions were regularized by 2 - 2.5% and MWF estimates for Protocol 1 data acquired at both sites were calculated with the MW range of 10 - 50 ms (actual upper integration limit of 47.6 ms). Protocol 2 data, although compared to Protocol 1 data using the same MW range, was also investigated with a 10 - 40 ms (actual integration limit of 41.0 ms), 10 - 50 ms (actual integration upper limits of 47.6 and 50.1 ms were investigated) and a variable range based on manual peak separation. Table 4.2 summarizes the protocol acquisitions and analysis carried out.

4.2.2 Scan Re-scan Reproducibility

Scan re-scan reproducibility of the qT_2 method also has to be thoroughly investigate before use in clinical studies at the same site or across centres. For this purpose, a healthy subject was imaged on separate occasions to establish the reproducibility of MWF estimates across scans of the same ROIs. The purpose of the test was to better understand the amount of variability in MWF measurements due to measurement error, spatial variability, and analysis parameters.

The larger voxels (poorer resolution) of the MNI protocol are more susceptible to partial volume effects. In order to minimize volume averaging on MNI protocol images, ROIs would have to be drawn stringently such that the number of voxels making up that volume would be greatly reduced, thereby compromising SNR. For this reason, as well as the fact that it has been used for many multi-component T_2 studies and is the most established, only the UBC protocol was acquired for scan re-scan tests.

A healthy subject (female, age 25 years) was scanned over four sessions and the slice placed through the same volume as described in Section 4.2. A screen capture of the slice

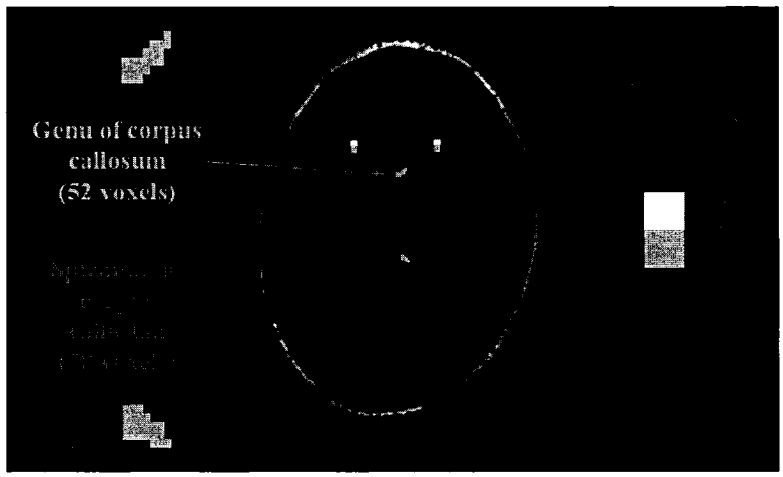

(a)

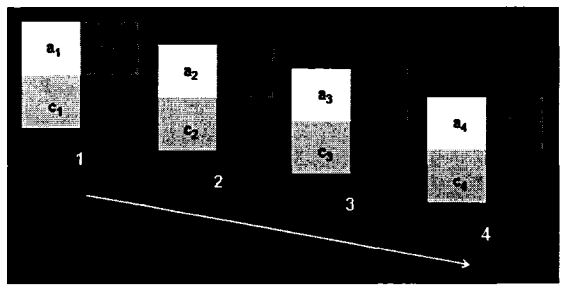

(b)

Figure 4.4: (*a*) Illustration of the WM ROIs chosen and their sub-divisions. (*b*) An example of how the minor forceps ROIs' 4 sub-divisions were compared over 4 scans. The genu and splenium ROIs each consisted of 2 sub-divisions.

profile from the first scan was used as a reference image to minimize slice placement errors for subsequent scans. The myelin water signal constitutes a minor component in the total water signal, thereby making its detection difficult. Furthermore, larger heterogeneous volumes of WM are easier to select compared to GM in the acquired slice. For these reasons, only WM ROIs were chosen for the scan-rescan test, namely the (i) left and (ii) right minor forceps, and the (iii) genu and (iv) splenium of the corpus callosum.

Automated registration of ROIs across scans was attempted, but registration of the 3D anatomical was not robust and incorrect transformations led to erroneously registered ROIs. Instead, a manual matching of ROIs with fixed dimensions were carefully aligned across the 4 scans (Figure 4.4a). The left and right minor forceps each consisted of 64 voxels and were sub-divided into 4 sections of 16 voxels each. The genu and splenium of the corpus callosum was drawn with 52 and 78 voxels, respectively, and sub-divided (roughly left-right) into 2 sub-sections of 26 and 39 voxels, respectively. Figure 4.4b illustrates how MWFs were compared:

1. across scans (as entire or sub-divided ROIs)
2. across ROI sub-sections within a scan
3. using different MW ranges
4. using various amounts of regularization as controlled by increased χ^2.

4.2.3 Across Subjects and Regional Variations

MWF profiles across subjects and brain regions were generated by acquiring data from both the UBC and MNI protocol on 10 normal subjects (5 males and 5 females), mean age of 27 (range from 24 to 31). The slice profile and ROIs analyzed are illustrated in Figure 4.3. All ROIs (except for the noise ROI) were drawn on the UBC image since its higher resolution allows better differentiation between WM and GM for minimizing volume averaging. Each ROI drawn on the UBC images contained the same number of voxels across all subjects to maintain similar SNR. Some ROIs had flow artifacts neighbouring or running through

them; therefore, ROI sizes had to be compromised to maintain matched SNR across subjects. Instead of drawing ROIs on MNI protocol images, a better comparison of MWFs between the protocols was accomplished by mapping ROIs from the UBC image space to the MNI image space by resampling down to the MNI protocol resolution. Due to the intricacies of the image resampling tools, the number of voxels from the UBC image ROIs do not translate to the same number of voxels across all MNI image ROIs. As shown in Table 4.3, there are some small variations in the number of voxels seen in the same ROI for the MNI protocol data.

In summary, the following data sets from normal subjects were compared using the MW range of 10 - 40 ms (actual upper integration limit of 41.0 ms) and 10 - 50 ms (actual upper integration limit of 50.1 ms), as well as manual peak seperation:

1. UBC protocol

2. MNI protocol.

Table 4.3: Summary of the number of voxels in the ROIs for various protocols.

ROI	**UBC protocol**	**MNI protocol**
Genu	30	3 - 7
Splenium	43	4 - 9
Minor forceps	128	24 - 30
Major forceps	99	16 - 21
Head caudate	26	3 - 7
Thalamus	41	4 - 9

Chapter 5

Results

The overall goal of the thesis is to assess the robustness of the MWF as an indicator of myelin content using a multi-echo acquisition and multi-component T_2 analysis. The initial step was to use simulations to validate the chosen analysis method (see Chapter 3). The next step involved investigating cross-site reproducibility and verifying developed protocols and analysis methods with the UBC group who has been using this technique and actively publishing work in normal, MS, schizophrenic, and phenylketonuria (PKU) subjects. Further studies were then carried out to measure scan re-scan reproducibility of MWFs with different protocols in a normal subject, as well as measuring the MWF variability in a group of normal subjects. Chapter 3 contains the results from the simulation study, while the ensuing sections report the findings from the human studies. Specifically, this chapter presents results of the *in vivo*:

- cross-site reproducibility of MWF estimates
- scan re-scan reproducibility of MWF estimates
- MWF estimates in healthy subjects.

5.1 Cross-site Reproducibility of MWF Estimates

The UBC group has extensively developed the single-slice, modified multi-echo CPMG acquisition, whereas the MNI group developed a protocol with similar SNR but shorter scan time at the expense of spatial resolution. The data presented here are from the same slice of the same healthy subject collected at UBC and MNI. Figure 5.1 shows the six ROI T_2 distributions from Protocol 1 acquired and analyzed at both sites, and Table 5.1 summarizes the MWFs obtained from these distributions. It is evident from the negligible differences in MWFs seen in the table that the locally implemented regularizing NNLS fitting algorithm is consistent with UBC's. Protocol 1 acquired at UBC and MNI have similar distributions with some variation in the locations of the short and main T_2 peaks as well as the width of the main T_2 peak. UBC acquired data seem to contain defined short T_2 peaks (present in all ROIs except for the major forceps and thalamus). MNI acquired data do not have a short T_2 peak but has signal, with relatively high amplitude for most ROIs, at the first T_2 sample which drops down to zero over the next few T_2 samples. Despite these noticeable variations in the protocols' distributions, MWFs are surprisingly similar and contain absolute differences of $\sim$2% or less.

Figure 5.2 compares the distributions from Protocols 1 and 2 acquired and analyzed at the MNI. Table 5.1 contains MWF estimates for Protocol 1, MNI acquired data and Table 5.2 contains estimates from Protocol 2, MNI acquired data calculated with various MW

Table 5.1: Summary of the MWFs from Protocol 1 data acquired at UBC and MNI using the upper integration limit of 47.6 ms.

	Protocol 1 at UBC		**Protocol 1 at MNI**	
Analyzed at	*UBC*	*MNI*	*UBC*	*MNI*
MW range	*10 - 47.6 ms*	*10 - 47.6 ms*	*10 - 47.6 ms*	*10 - 47.6 ms*
Genu	10.35	10.28	10.16	10.18
Splenium	12.93	12.93	14.17	14.05
Minor forceps	7.71	7.71	8.97	8.97
Major forceps	10.56	10.67	10.49	10.47
Head caudate	3.05	3.02	4.63	4.65
Thalamus	7.50	7.53	5.58	5.60

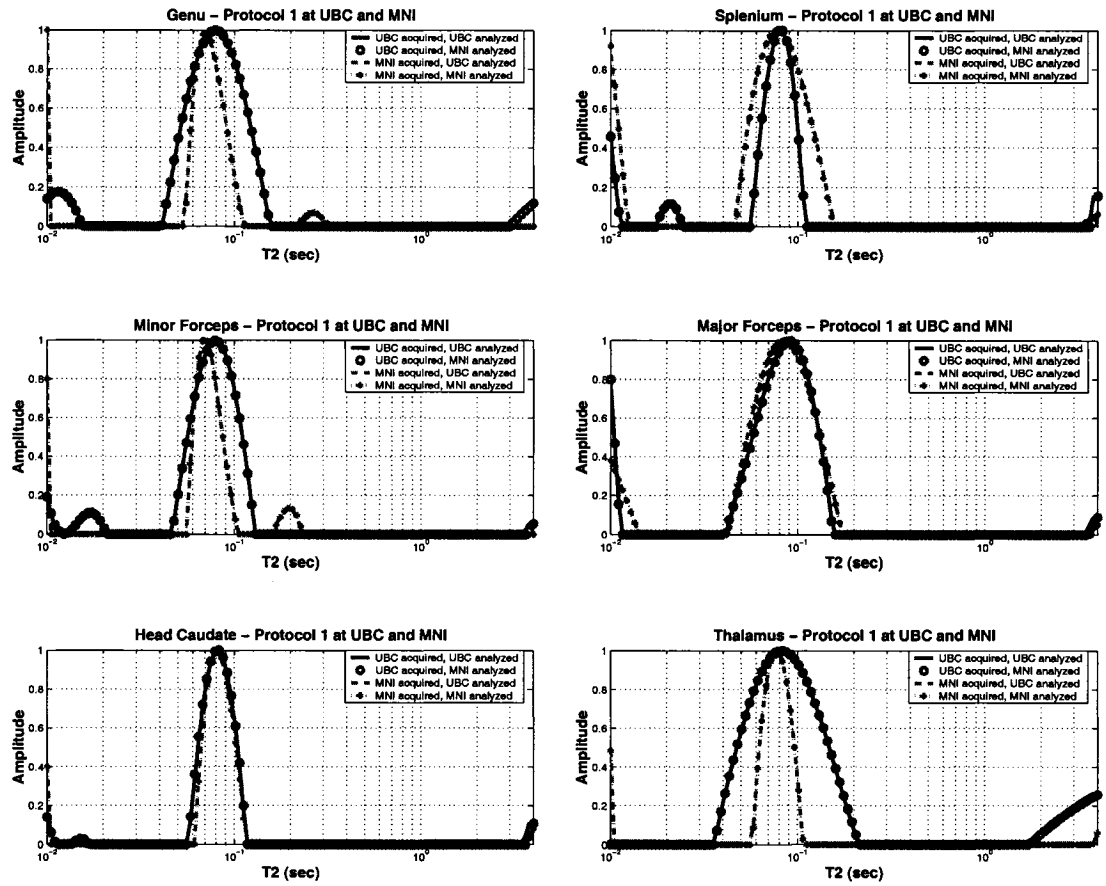

Figure 5.1: T_2 distributions for Protocol 1 data collected at UBC and MNI and analyzed by both sites.

Table 5.2: Summary of the MWFs from Protocol 2 data acquired and analyzed at MNI for various MW ranges. The manual peak separation method assigns any signal below the main T_2 peak to myelin water.

	Protocol 2 at MNI			
Analyzed at	*MNI*			
MW range	*10 - 41.0 ms*	*10 - 47.6 ms*	*10 - 50.1 ms*	*Manual Peak Separation*
Genu	8.18	14.63	17.56	5.36
Splenium	10.74	18.75	21.78	0.00
Minor forceps	6.77	9.02	11.52	6.77
Major forceps	10.22	10.22	10.22	10.22
Head caudate	2.08	2.08	2.08	2.08
Thalamus	3.96	4.11	5.53	3.96

Table 5.3: Summary of the MWFs using different integration limits from Protocol 1 data acquired at UBC and analyzed at UBC. Discrepancies in MWF estimates are marked (*).

	Protocol 1 at UBC			
MW range	*10 - 41.0 ms*	*10 - 47.6 ms*	*10 - 50.1 ms*	
Genu	6.57	10.21	12.64	*
Splenium	12.73	12.73	12.73	
Minor forceps	7.18	7.68	9.13	*
Major forceps	8.11	10.51	12.16	*
Head caudate	3.02	3.02	3.02	
Thalamus	2.06	7.42	9.86	*
	Protocol 1 at MNI			
MW range	*10 - 41.0 ms*	*10 - 47.6 ms*	*10 - 50.1 ms*	
Genu	10.16	10.16	10.16	
Splenium	13.46	14.12	15.71	*
Minor forceps	8.97	8.97	8.97	
Major forceps	8.18	10.46	12.35	*
Head caudate	4.59	4.59	4.59	
Thalamus	5.55	5.55	5.55	

ranges. Similar to the distributions from Protocol 1 data acquired at UBC and MNI, Protocol 1 and 2 data acquired at MNI show relatively similar distributions with discrepancies mainly seen in the main T_2 peak width. Besides the major forceps, all other Protocol 2 distributions appear to be missing a defined short T_2 peak but exhibit an extremely short T_2 component as seen in Protocol 1 distributions. Comparing Tables 5.1 and 5.2, Protocols 1 and 2 acquired at MNI show MWFs with absolute discrepancies as large as $\sim$5%.

Table 5.3 shows MWF estimates from Protocol 1 data acquired at both sites and analyzed at UBC. About half the distributions show MWF variations with different MW ranges, but most importantly is the significant difference seen when integrating with one T_2 sample higher (i.e., comparing the integration limit of 47.6 with 50.1 ms). Data acquired with Protocol 2 also returned a wide range of values depending on the defined MW range of 10 - 40 ms, 10 - 50 ms or using manual peak separation. Results showed absolute MWF estimates with large variations of as much as $\sim$20%).

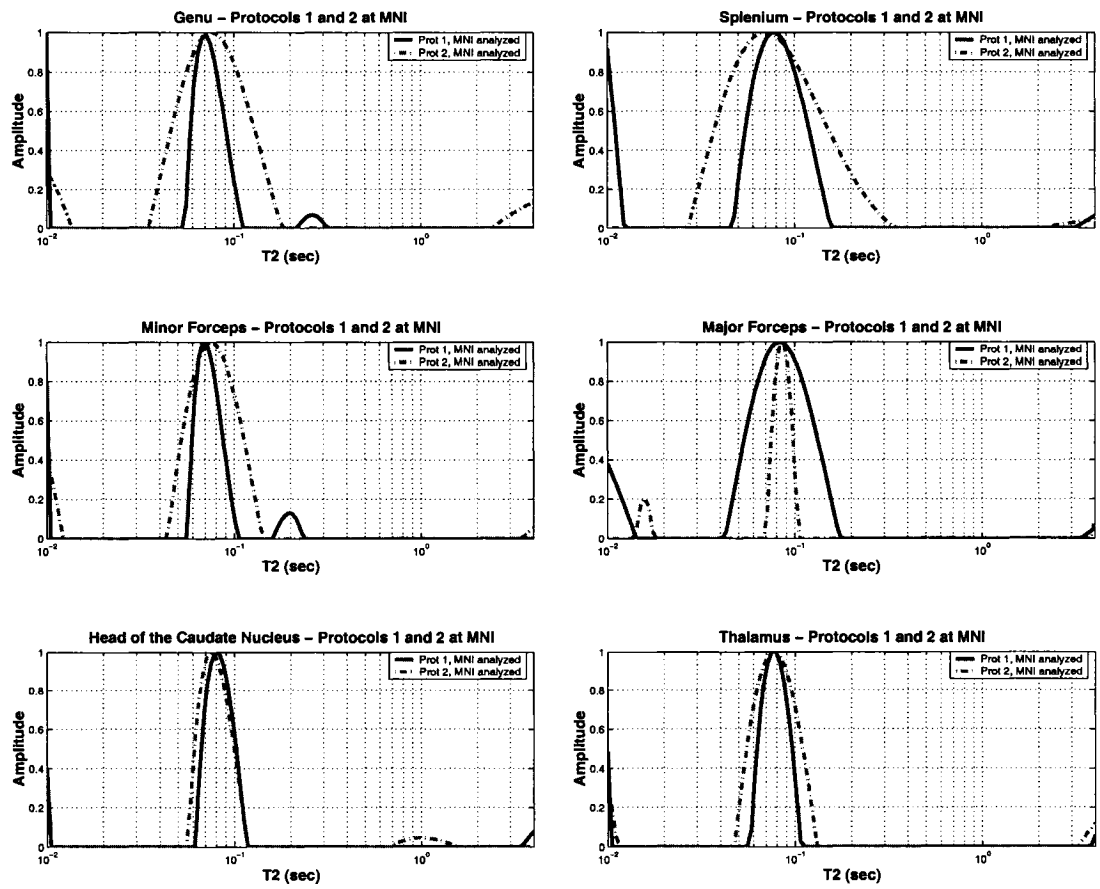

Figure 5.2: T_2 distributions for Protocols 1 and 2 data collected and analyzed at MNI.

5.2 Scan Re-scan Reproducibility of MWF Estimates

Decay curves of each ROI from the 4 separate scans of the same slice of a healthy subject are shown in Figure 5.3. Absolute decay curve differences are also calculated from scans 2 through 4 using the first scan as the reference scan. Discrepancies in the decay curve from scan-to-scan are larger at earlier echo times and decrease with later echoes, possibly indicating the difficulties in acquiring consistent short T_2 signals.

The standard error of the mean ($\sigma_M = \sigma/\sqrt{N}$, where M denotes the mean and N is the number of samples) in MWF estimates in adjacent WM tissue sub-sections within scans and identical tissue sub-sections across scans are not significantly different. As an example (refer to Figure 4.4b), the σ_M of $\{a_1, b_1, c_1, d_1\}$ are comparable to that of $\{a_1, a_2, a_3, a_4\}$, and $\{b_1, b_2, b_3, b_4\}$, etc. Therefore, each sub-section can be considered separate measurements which allows the number of individual measurements to increase from 4 (the number of scans). As a result, the MWF estimates for the left and right minor forceps were each based on 16 measurements (i.e., 4 measurements $\times$ 4 scans), while the genu and splenium were each based on 8 measurements (i.e., 2 measurements $\times$ 4 scans). Figure 5.4 shows the distributions for entire ROIs across the 4 scans. Figure 5.5 shows different distributions from the 4 sub-sections from scan 1 of the left minor forceps as well as all sub-sections across all 4 scans for the genu. Tables 5.4 - 5.7 summarizes the $\overline{MWF}$s for the various ROIs calculated using the MW range of 10 - 40 and 10 - 50 ms (actual upper integration limit of 41.0 and 50.1 ms, respectively) for distributions with different allowed ranges of regularization.

As seen in Figure 5.6, MWF increases with increased regularization for those calculated with the 10 - 50 ms MW range. For MWF calculations using the 10 - 40 ms range, 3 out of 4 ROIs show a small decrease with increased regularization. The decrease in MWF is not expected if the main T_2 peak broadens and spills over into the MW range, causing additional signal to be assigned to MW. The 40 ms cut-off is probably small enough that the main T_2 peak does not breach this threshold within these levels of smoothing. Any differences in MWF estimates with changes in regularization (like the small decrease with increased smoothing) is likely a result of signal assignment from the regularization routine.

Overall, MWF estimates are higher and more dependent upon regularization when using a 10 - 50 ms integration window, making the 10 - 40 ms MW range more suited to consistent MWF estimates. Despite the noted dependency on regularization, all MWF estimates calculated with the same MW range across different levels of regularization fall within one standard deviation of each other.

Table 5.4: Summary of $\overline{MWF}$s using a 10 - 40 and 10 - 50 ms (actual upper integration limit of 41.0 and 50.1 ms, respectively) MW range for various allowed increases of χ^2 for the genu of the corpus callosum.

	Genu									
	10 - 40 ms					**10 - 50 ms**				
χ^2	*0-0.5*	*0.5-1*	*1-1.5*	*1.5-2*	*2-2.5*	*0-0.5*	*0.5-1*	*1-1.5*	*1.5-2*	*2-2.5*
$\overline{MWF}$	**8.80**	**7.93**	**8.27**	**8.58**	**8.83**	**12.96**	**17.57**	**18.68**	**19.43**	**20.38**
σ	2.98	2.04	2.11	1.78	1.82	4.30	4.62	5.02	5.21	5.29
σ_M	1.05	0.82	0.84	0.63	0.64	1.52	1.63	1.78	1.84	1.87
% σ	11.99	9.09	9.01	7.34	7.30	11.73	9.29	9.51	9.49	9.18

Table 5.5: Summary of $\overline{MWF}$s using a 10 - 40 and 10 - 50 ms (actual upper integration limit of 41.0 and 50.1 ms, respectively) MW range for various allowed increases of χ^2 for the splenium of the corpus callosum.

	Splenium									
	10 - 40 ms					**10 - 50 ms**				
χ^2	*0-0.5*	*0.5-1*	*1-1.5*	*1.5-2*	*2-2.5*	*0-0.5*	*0.5-1*	*1-1.5*	*1.5-2*	*2-2.5*
$\overline{MWF}$	**16.43**	**14.41**	**13.57**	**13.47**	**13.31**	**16.72**	**18.21**	**18.78**	**19.33**	**19.71**
σ	6.84	5.43	4.39	3.76	3.15	6.63	2.08	1.68	1.75	1.91
σ_M	2.42	1.91	1.50	1.33	1.12	2.34	0.74	0.60	0.62	0.68
% σ	14.71	13.31	11.43	9.86	8.38	14.02	4.04	3.17	3.21	3.43

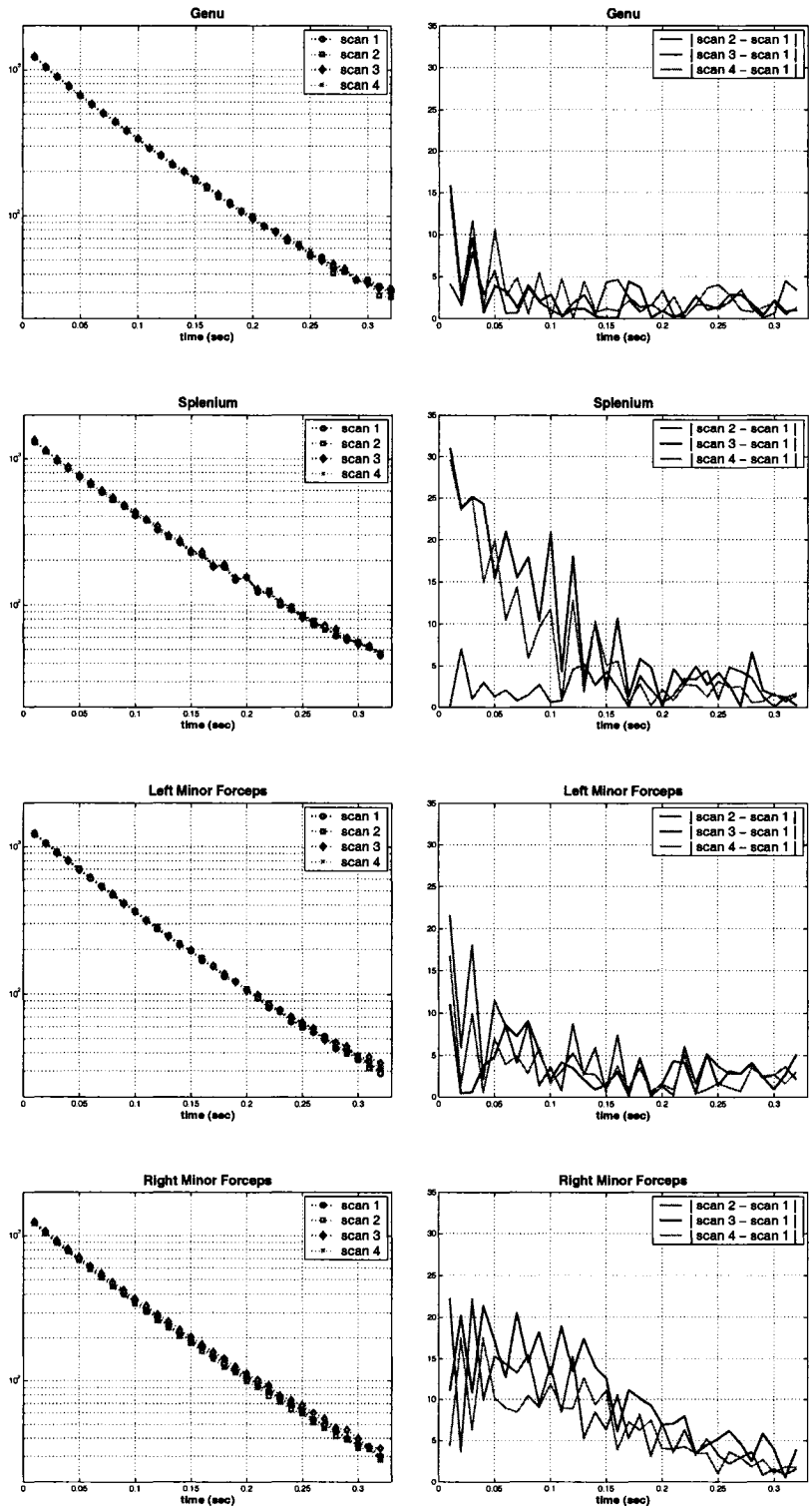

Figure 5.3: Entire ROI T_2 decay curves for Protocol 1 data collected on four separate scans on the same slice of the same subject (*left column*). Absolute decay curve differences between the first scan and subsequent scans were also calculated (*right column*).

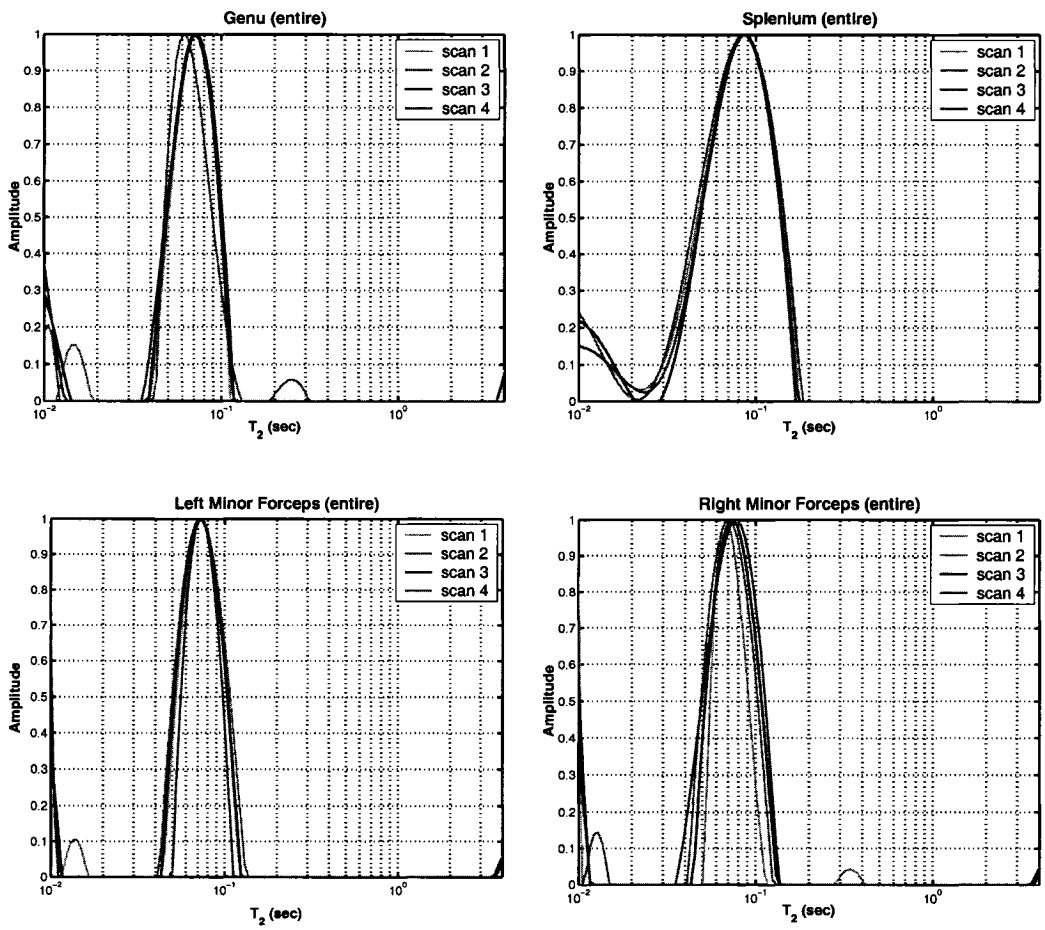

Figure 5.4: Entire ROI T_2 distributions (2 - 2.5% regularization) for Protocol 1 data collected on four separate scans on the same slice of the same subject.

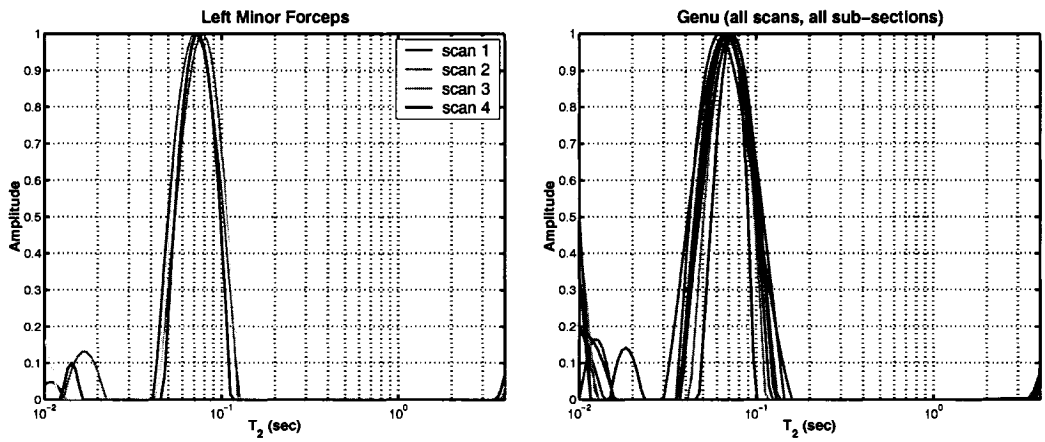

Figure 5.5: T_2 distributions for sub-sections within the entire ROI from Protocol 1 data collected on four separate scans on the same slice of the same subject. The left minor forceps plot shows the distribution from the four sub-sections from the first scan. The genu plot shows the distributions from all sub-sections across all four scans.

Table 5.6: Summary of $\overline{MWF}$s using a 10 - 40 and 10 - 50 ms (actual upper integration limit of 41.0 and 50.1 ms, respectively) MW range for various allowed increases of χ^2 for the splenium of the left minor forceps.

	Minor forceps (left)									
	10 - 40 ms					**10 - 50 ms**				
χ^2	*0-0.5*	*0.5-1*	*1-1.5*	*1.5-2*	*2-2.5*	*0-0.5*	*0.5-1*	*1-1.5*	*1.5-2*	*2-2.5*
$\overline{MWF}$	**7.06**	**5.98**	**5.59**	**5.39**	**5.21**	**7.55**	**8.25**	**9.46**	**10.09**	**10.73**
σ	2.12	1.75	1.79	1.79	1.73	3.06	2.76	2.49	2.51	2.62
σ_M	0.53	0.44	0.45	0.45	0.43	0.77	0.69	0.62	0.63	0.65
% σ	7.53	7.33	8.02	8.31	8.29	10.14	8.36	6.57	6.21	6.10

Table 5.7: Summary of $\overline{MWF}$s using a 10 - 40 and 10 - 50 ms (actual upper integration limit of 41.0 and 50.1 ms, respectively) MW range for various allowed increases of χ^2 for the splenium of the right minor forceps.

	Minor forceps (right)									
	10 - 40 ms					**10 - 50 ms**				
χ^2	*0-0.5*	*0.5-1*	*1-1.5*	*1.5-2*	*2-2.5*	*0-0.5*	*0.5-1*	*1-1.5*	*1.5-2*	*2-2.5*
$\overline{MWF}$	**7.75**	**6.84**	**6.64**	**6.55**	**6.53**	**10.43**	**12.48**	**12.90**	**13.37**	**13.68**
σ	2.73	1.83	1.67	1.65	1.60	3.13	3.88	3.92	4.10	4.14
σ_M	0.68	0.46	0.42	0.41	0.40	0.78	0.97	0.98	1.03	1.03
% σ	8.82	6.70	6.29	6.31	6.12	7.50	7.78	7.60	7.67	7.56

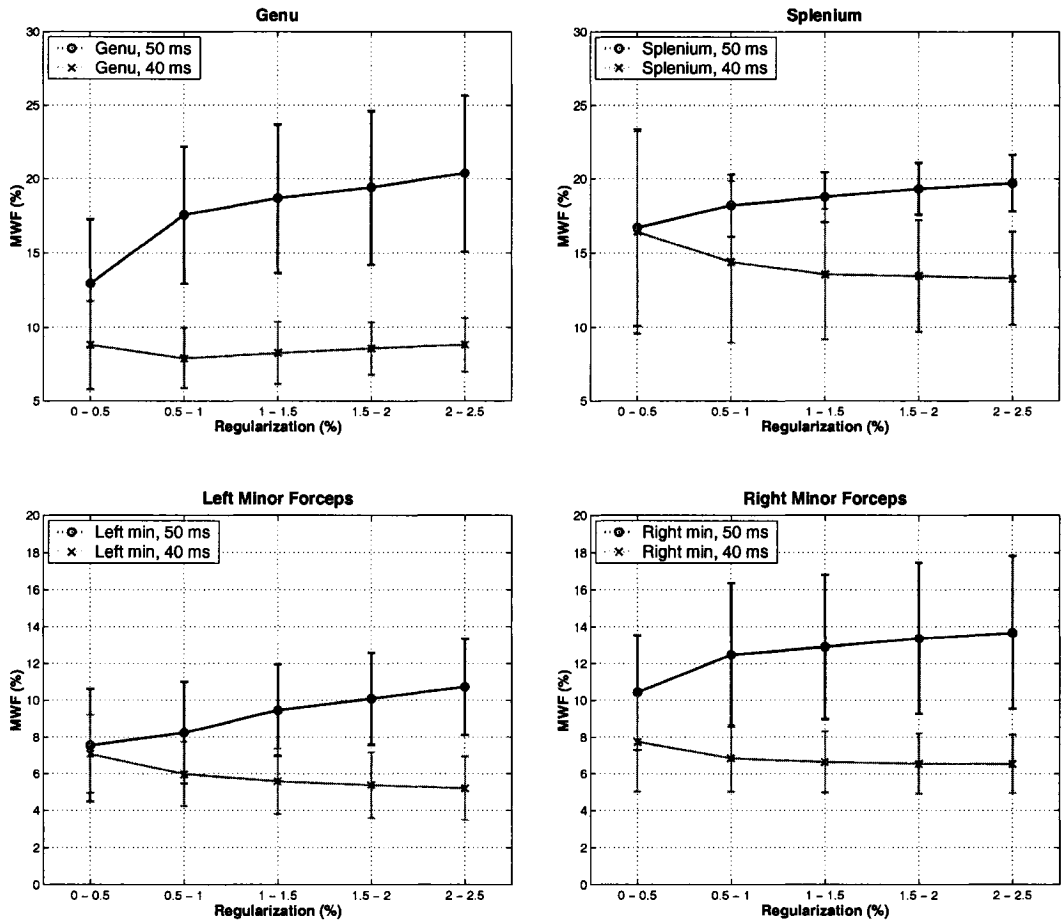

Figure 5.6: $\overline{MWF}$s (σ as error bars) calculated with different MW ranges from T_2 distributions with different amount of regularization. Trends are labelled with $\times$ (10 - 40 ms MW range) and $\circ$ (10 - 50 ms MW range).

5.3 MWF Estimates in Healthy Subjects

Ten healthy subjects were scanned with the UBC and MNI protocol and MWF estimates of several WM and GM were calculated from T_2 distributions (2 - 2.5% regularization) using different MW ranges. Figure 5.7 compares a few ROIs acquired with the UBC and MNI protocol and shows the normalized decay curves on a logarithmic scale and their T_2 distributions. Although not shown in Figure 5.7, both UBC and MNI protocol data have similar signal strength in the 1^{st} echo (the UBC protocol has marginally larger signal) with signal differences appearing at later echo times. Again, distributions are similar with the main peak's mean T_2 staying comparably constant despite some variation in width. Differences in the short T_2 component are more pronounced.

Figure 5.8 contains the T_2 distributions (regularized distribution and the underlying LS-solution) from all ROIs of a normal subject using the UBC protocol with 2 - 2.5% regularization. The distributions for GM structures are typically well-defined. In GM, the MWF comes from a short T_2 component (as in the case of the head of the caudate nucleus distribution in Figure 5.8), or from part of the main T_2 peak signal which spills over into the MW range (as in the thalamus distribution of Figure 5.8). Some WM structures contain a well-defined short T_2, either a peak by itself, or a component at the shortest T_2 samples. Unlike the distributions from the cross-site experiment where manual peak separation was trivial, some splenium distributions from this experimental data were problematic. When distributions had no definite peak separation (i.e., the distribution between the short and main peaks was never zero), the absolute lowest point between the two peaks was used as the MW cut-off.

MWF estimates for different brain structures in normal subjects are shown in Figures 5.9 - 5.10. A summary of $\overline{MWF}$ estimates (error bars represent σ) calculated with different MW ranges are shown in Figures 5.11 - 5.12 and are listed in Table 5.8. The GM MWF estimates are in very good agreement for the different MW range cut-offs, with the exception of the 10 - 50 ms integration window for the thalamus. Larger variances between MWF calculation methods are seen for WM structures. Overall, the manual peak separation method and the 10 - 40 ms MW range have better matched $\overline{MWF}$ and σ. The 10 - 50

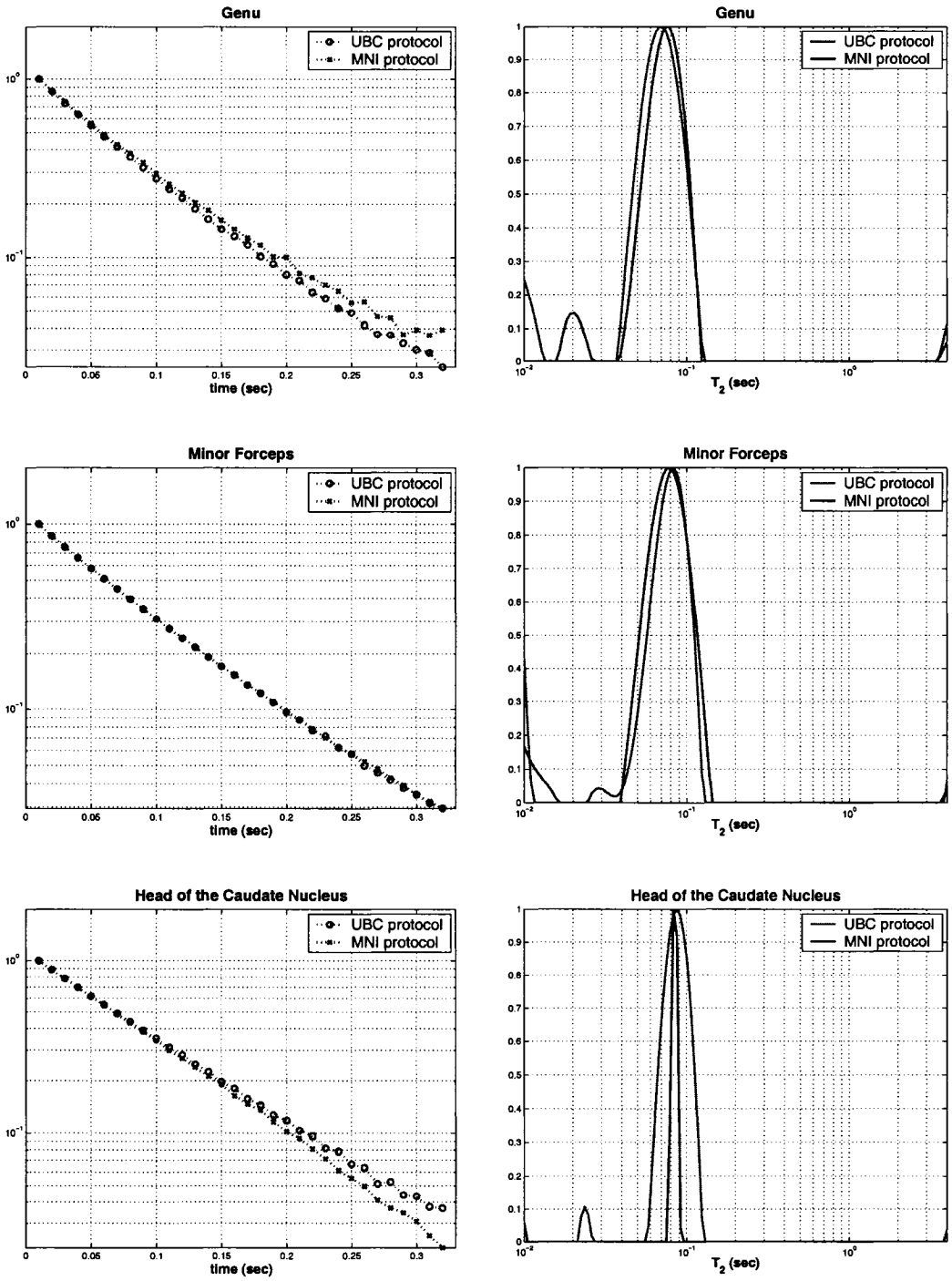

Figure 5.7: Comparison of the protocols' decay curves (normalized) and distributions (2 - 2.5% regularization).

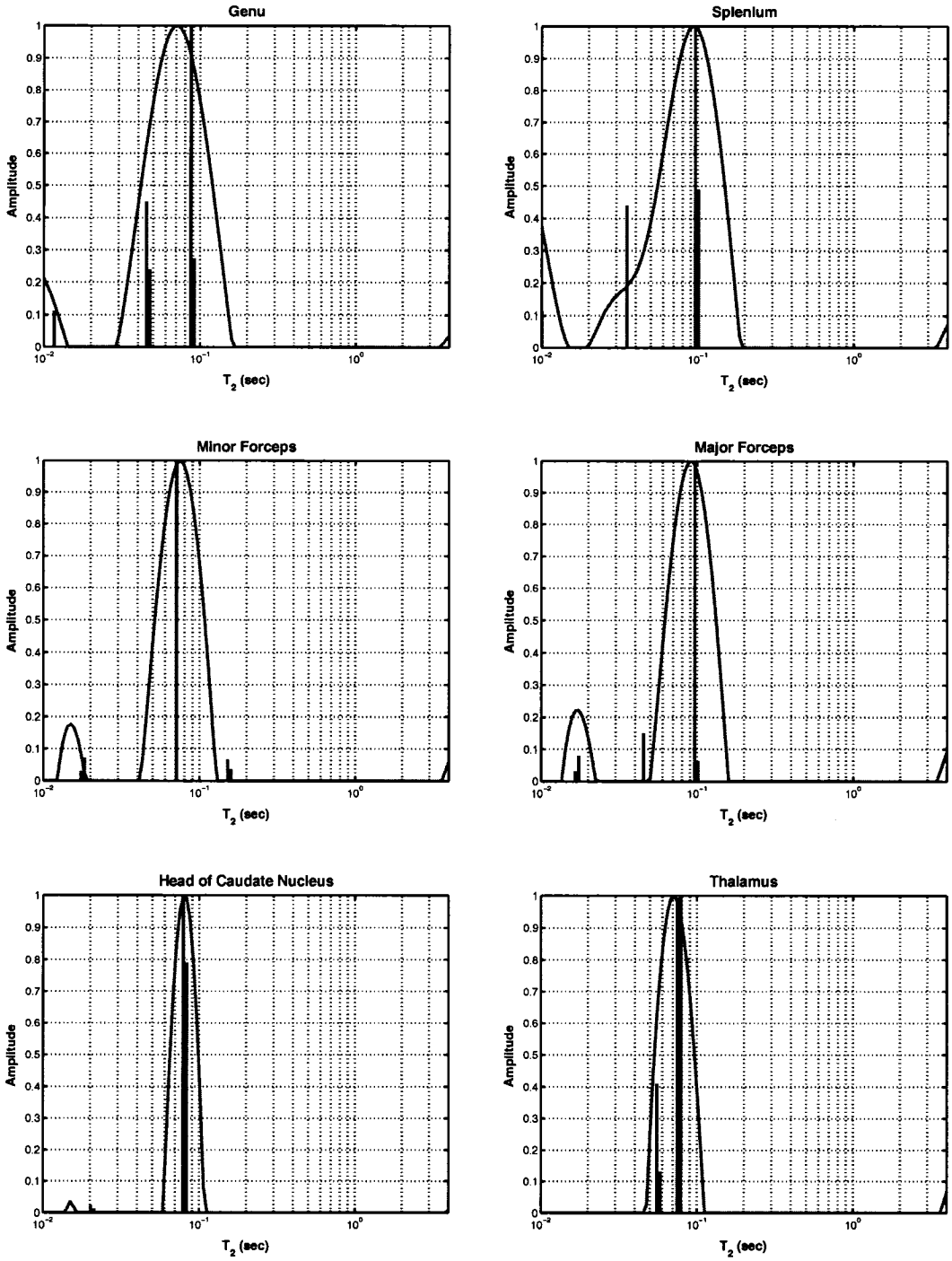

Figure 5.8: Regularized T_2 distributions (red) using the UBC protocol, 2 - 2.5% regularization and their underlying LS-solutions (blue) from a normal subject.

ms integration window introduces larger σ as well as larger MWF estimates, which in the worse case is 3 times larger than the smallest estimate given by the manual peak separation method. The results from the UBC and MNI protocol overlap but the MNI estimates and σ are marginally higher in most cases (the MWF is at most 2% higher).

Figure 5.13 gives examples of a subject's myelin water map with different amounts of regularization using either a 40 or 50 ms MW range cut-off (actual upper integration limit of 21.0 and 50.1 ms, respectively). As a result of increased regularization, there are less "holes" in the WM regions of the myelin water maps. Little or no visual differences are seen between the 10 - 40 or 10 - 50 ms MW range. Flow artifacts are seen in the phase encode direction and prevent ideal myelin water maps to be produced. Fortunately, in the case shown, the artifact runs through a region with low MW structures, thereby presenting little interference.

Table 5.8: $\overline{MWF}$ (σ in brackets) for UBC protocol data and MNI protocol data. Values were calculated for normal subjects using manual peak separation and the 40 and 50 ms MW range cut-off from distributions with 2 - 2.5% regularization.

		UBC protocol		
ROI	*# voxels*	*Peak sep*	*40 ms*	*50 ms*
Genu	30	5.51 (1.62)	8.41 (2.73)	18.80 (5.63)
Splenium	43	6.89 (3.06)	13.35 (2.84)	20.22 (3.83)
Minor forceps	128	5.89 (1.43)	6.17 (1.40)	10.38 (3.29)
Major forceps	99	7.80 (0.92)	7.82 (0.92)	9.74 (1.55)
Head caudate	26	0.89 (1.01)	0.90 (1.01)	0.89 (1.01)
Thalamus	41	2.09 (1.89)	2.32 (1.74)	3.87 (2.73)
		MNI protocol		
ROI	*# voxels*	*Peak sep*	*40 ms*	*50 ms*
Genu	3 - 7	8.86 (2.60)	10.28 (2.75)	16.90 (6.26)
Splenium	4 - 9	6.55 (3.63)	12.31 (3.86)	20.44 (4.62)
Minor forceps	24 - 30	5.95 (1.77)	6.30 (1.43)	12.22 (3.25)
Major forceps	16 - 21	8.54 (1.97)	8.63 (1.95)	11.04 (1.83)
Head caudate	3 - 7	1.28 (1.20)	1.28 (1.20)	1.49 (1.13)
Thalamus	4 - 9	1.18 (1.37)	2.59 (3.51)	5.88 (7.51)

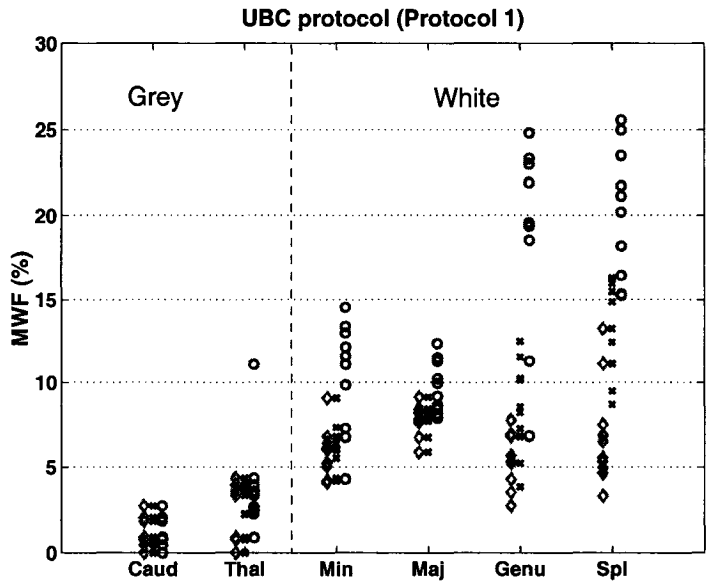

Figure 5.9: MWF estimates calculated with different MW ranges for UBC protocol data. Manual peak separation (◇), MW range 40 ms (×), MW range 50 ms (○). *Caud*: head of the caudate, *Thal*: thalamus, *Min*: minor forceps, *Maj*: major forceps, *Genu*: genu, *Spl*: splenium.

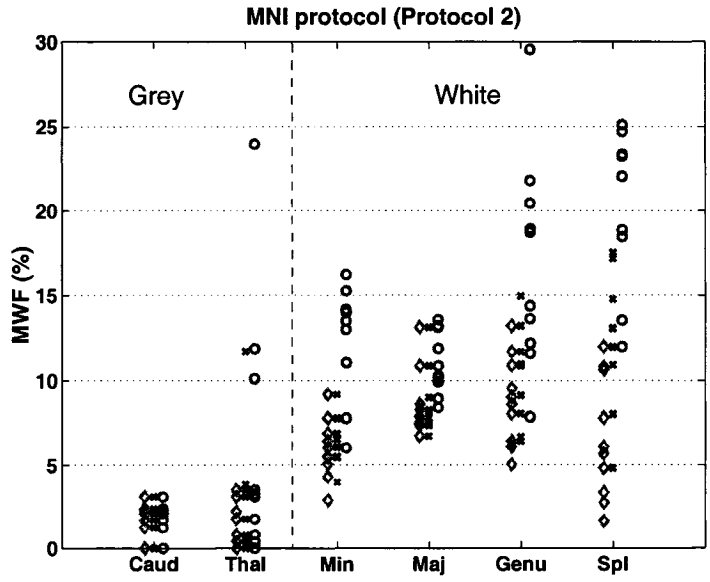

Figure 5.10: MWF estimates calculated with different MW ranges for MNI protocol data. Manual peak separation (◇), MW range 40 ms (×), MW range 50 ms (○). *Caud*: head of the caudate, *Thal*: thalamus, *Min*: minor forceps, *Maj*: major forceps, *Genu*: genu, *Spl*: splenium.

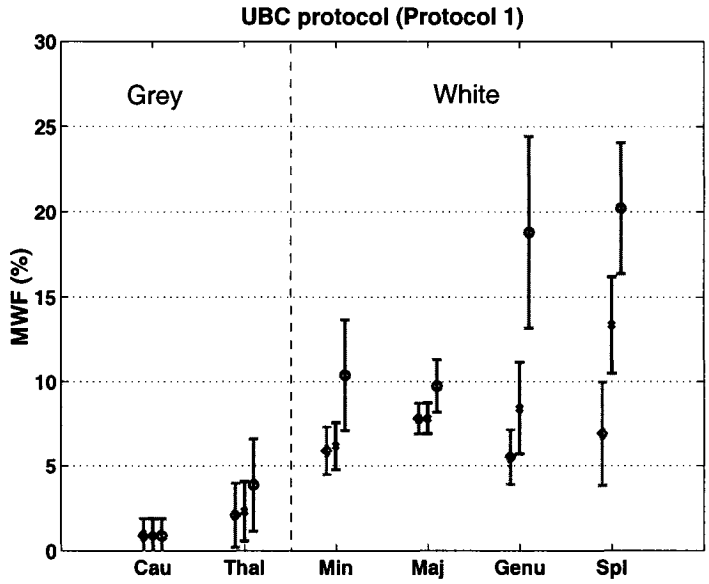

Figure 5.11: Summary plot of $\overline{MWF}$ estimates (error bars represent σ) from UBC protocol data for various MW ranges.
Manual peak separation (◇), MW range 40 ms (×), MW range 50 ms (○). *Caud*: head of the caudate, *Thal*: thalamus, *Min*: minor forceps, *Maj*: major forceps, *Genu*: genu, *Spl*: splenium.

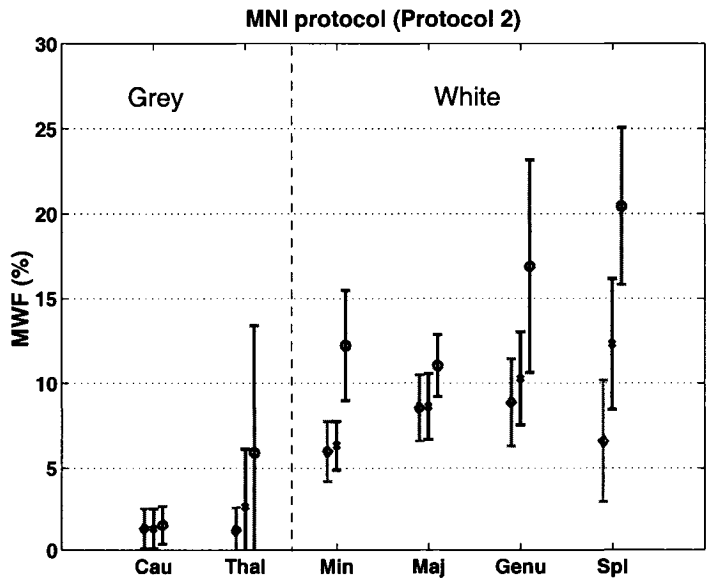

Figure 5.12: Summary plot of $\overline{MWF}$ estimates (error bars represent σ) from MNI protocol data for various MW ranges.
Manual peak separation (◇), MW range 40 ms (×), MW range 50 ms (○). *Caud*: head of the caudate, *Thal*: thalamus, *Min*: minor forceps, *Maj*: major forceps, *Genu*: genu, *Spl*: splenium.

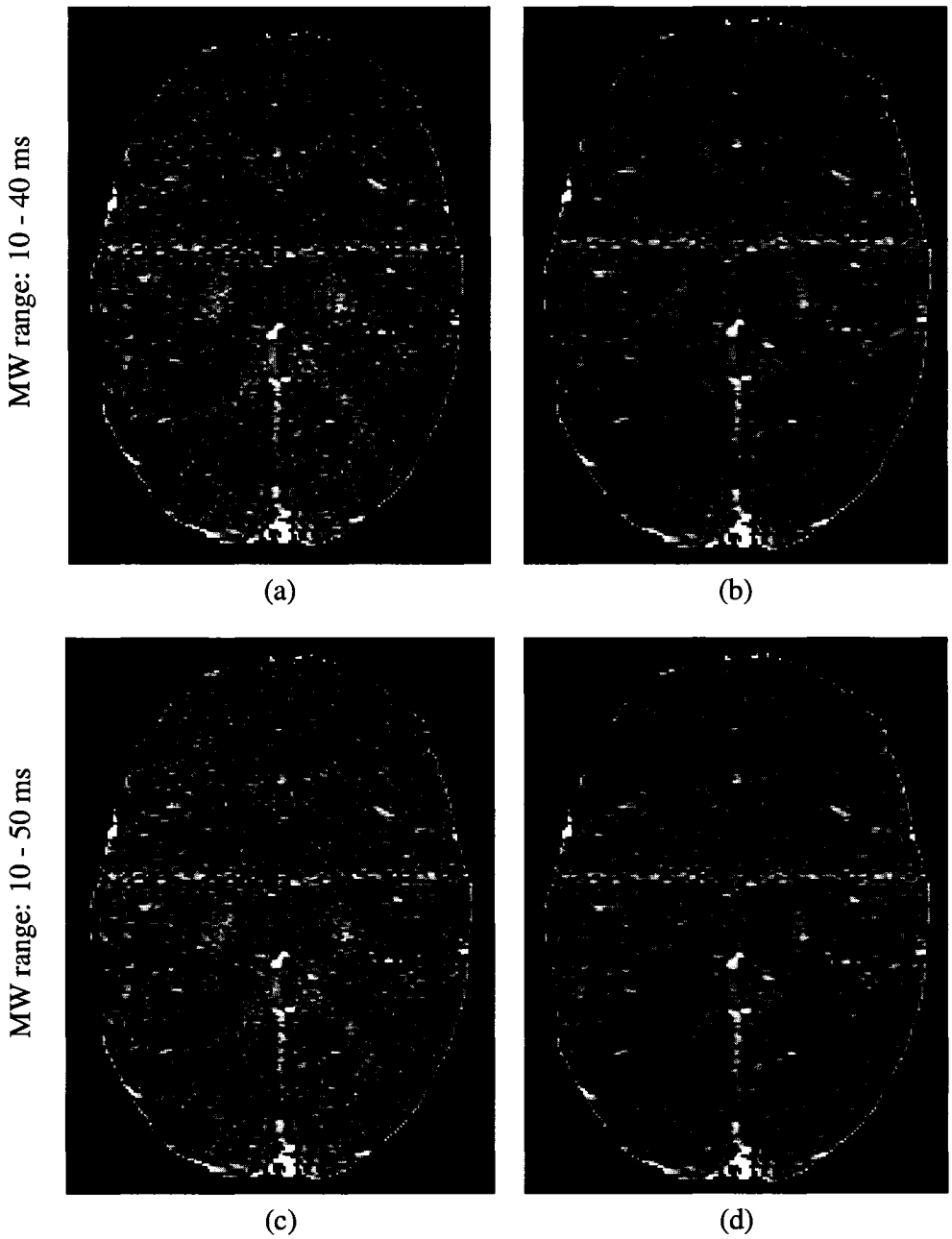

Figure 5.13: The top two myelin water maps are created with a MW range of 10 - 40 ms (actual upper integration limit of 41.0 ms) with allowed χ^2 increases of (*a*) 0 - 0.5% and (*b*) 2 - 2.5%.
The bottom two myelin water maps are created with a MW range of 10 - 50 ms (actual upper integration limit of 50.1 ms) with allowed χ^2 increases of (*c*) 0 - 0.5% and (*d*) 2 - 2.5%. All maps are from the same healthy subject using the UBC protocol.

Chapter 6

Discussion

Chapters 3 and 5 presented results from the simulation study and data collected on normal subjects. The simulation study validated our NNLS implementation and allowed a better understanding of the effects of CSF contamination on WM and GM T_2 distributions and MWF estimates. Studies in healthy subjects were used to compare analysis procedures, determine the reproducibility of inter- and intra- site MWF measurements, and study MWF variations in a healthy population.

The focus of this chapter is a review of analysis procedures tested and their effect on MWF estimates. Further discussion centres on effects of different qT_2 acquisition protocols to arrive at a consistent and comparable measure of myelin water. Comparisons of our experimental results with previously reported qT_2 studies and explanations for discrepancies are also presented here. The consequences of our reproducibility studies are also cast in the form of example sample size calculations.

6.1 Simulation Study

The assumption of slow exchange between microstructural compartments for structural discrimination was used in our simulation studies. The effective limit of slow exchange is governed by the relative timescale of the expected MR process; that is, if the exchange process is slow compared to the T_2 decay rate. Our results showed that in order for the short (myelin water) and main (I/E water) T_2 peaks to be defined (i.e., clearly separable from each other), an SNR $\geq$ 200 is required. In general, the SNR affected the MWF histogram widths, with higher SNRs producing narrower histograms. However, extremely low SNR produced histograms that were skewed towards lower MWFs. The important issue of the T_2 range assigned to MW was investigated, and although MWFs were expected to increase with larger MW ranges, simulations showed that MWF histograms agreed for SNR $\geq$ 200 for a MW range upper T_2 limit encompassing 40 and 50 ms. Since T_2 distributions become better defined with higher SNR, the MWF histograms stabilize. For SNR = 200, normal WM data (14% MW, 0% CSF, 2 - 2.5% regularization) produced mean MWF estimates of $\approx$13% but calculated MWFs had $\sigma \approx 3\%$ and ranged between 7 - 19%.

We found that at SNR $\geq$ 200, increased regularization from 0 - 0.5% up to 2 - 2.5% did not compromise the ability to separate the T_2 distribution peaks. At lower levels of regularization, the main (I/E water) T_2 peak was closely represented by the sharp profile of the underlying delta functions of the LS-solution. As the distribution was smoothed, the peak amplitudes decreased but the pool sizes (given by the peak area) was compensated by peak broadening. For the main T_2 peak, broadening caused part of it to overlap into the MW range. Considering the I/E water peak spilling into the MW range, the MWF would be expected to increase. Instead, histogram profiles for various levels of regularization showed a small change with increased smoothing, namely the histogram peak moved from the true MWF to a slightly smaller value (underestimated by at most 1%). A plausible explanation is that the MW and I/E water signal (not using assigned MW ranges but strictly considering the area under the short and main T_2 peak, respectively) are incorrectly assigned, but although the MW signal is underestimated, the MWF reports a high value (compared to signal actually assigned to MW) due to partial inclusion of the I/E water peak. MWF

histograms stayed Gaussian-like while the full-width half-maximum (FWHM) marginally decreased with more regularization.

The ability of the regularized NNLS algorithm to accurately estimate the true MWF over the simulated range of expected MW contents in WM and GM was verified. At SNR = 200, with 2 - 2.5% regularization, the MWF histogram peak value was however consistently $\lesssim$1% below the modelled pool weight. With the exception of the 2% MWF simulation, the other simulations (6 - 18% MW) did not show any significant decrease in the FWHM of the MWF histograms. Therefore, MWF variability (not accounting for biological variability which relates to tissue with different myelin water content) across all brain tissue is expected to be independent of the actual MW content variations expected across regions.

Normal WM and GM modelled with CSF contamination had distributions (2 - 2.5% regularization) with a CSF-associated T_2 component above the I/E water peak starting at T_2 values as short as ~0.2 sec. With increased CSF contamination, there was a higher incidence of MW and I/E water T_2 peaks partially overlapping with each other, thereby making the task of peak separation, and hence MWF estimation, harder. In view of this, carefully selected tissue ROIs should be used to minimize potential errors caused by CSF contamination. Regardless of this, normal WM (MW 14%) simulations showed that with increased CSF, MWF calculated with different MW ranges had larger discrepancies. Larger MW ranges corresponded to increased $\overline{MWF}$ estimates as well as slightly larger histogram FWHM.

6.2 NNLS Analysis Procedure

In addition to analysis of simulations, analysis at both UBC and the MNI of the same human data sets allowed further verification that our modified NNLS analysis procedure is consistent with UBC's and could thereby be ruled out as a possible source of variability. The analysis software used at both sites was not identical but was based on the same basic algorithm, so it was important to use identical analysis parameters (see Table 3.2) to compare results. As expected, WM and GM ROIs in a healthy subject returned essentially identical T_2 distributions with MWF estimates within numerical error when algorithm parameters were matched.

Most qT_2 publications (the majority of which come from the UBC group) do not disclose complete details of the analysis procedure. The chosen analysis parameters for this thesis were based on published values by Jones [66, 67, 115] and personal communications with Dr. Alex MacKay. Table 6.1 summarizes the reported analysis parameters (unspecified values are denoted with a dash (-)) used in the various publications using NNLS to estimate MWF *in vivo*. Overall, regularizing by energy minimization (maximum of 2.5%) is most common. Stated MWF calculations use either a 40 or 50 ms MW range cut-off, with some studies vaguely citing calculations using signal from the small "myelin water" peak over the total distribution signal. Some studies have excluded any CSF signal in the definition of total water signal [65, 119], while others have attempted an absolute myelin water content (MWC) estimation in which the MW signal is normalized to an external water standard and T_1 corrected [120–122]. Whittall *et al.* [63] chose to use a 10 - 50 ms MW range because they found the T_2 times to vary from 10 - 40 ms. Therefore, they argue that by choosing a 10 - 50 ms window, the MWF would be centred on the true value. Negligible differences were seen in an MS study of 30 patients plus controls when MWF were calculated with a 40 or 50 ms cut-off (personal communication with Dr. Alex MacKay). A recent study on PKU subjects and controls [123] gave different values for the two MW intervals. Differences were thought to be due to the larger point spread function from a lower resolution matrix (128 $\times$ 128, not 256 $\times$ 128), as well as the variable TR used in that study (personal communication with Dr. Alex MacKay).

Table 6.1: Analysis parameters from select publications using NNLS. Entries with a dash (-) denote unspecified parameters.

	Regularization type (%)	**# T_2**	**T_2 range (ms)**	**MW range (ms)**
Flynn [117]	-	-	-	0 - 50
Jones [66, 67]	Energy (2 - 2.5%)	-	-	10 - 50
Jones [115]	Energy (2 - 2.5%)	120	10 - 4000	10 - 50
Kolind [124]	-	-	-	< 40
Laule [68, 123]	-	-	-	< 50
Laule [125]	Energy (2 - 2.5%)	120	15 - 2000	< 50
Lang [126]	-	-	-	< 50
MacKay [56]	none	-	-	Peak, 10 - 55*
Oh [111]	- ($< 1\%$)	80	15 - 2000	Peak
Tozer [109]	2^{nd} deriv (2 - 2.5%)	113	10 - 2000	< 50
Vavasour [46]	Energy (0.1 - 0.3%)	-	-	0 - 50
Vavasour [65]	Energy (-)	-	-	Peak†
Vavasour [119]	Energy (0.1 - 0.3%)	100	15 - 2000	15 - 40†
Vavasour [120–122]	-	-	-	0 - 40
Whitaker [127]	-	-	-	0 - 40
Whittall [63]	Energy (1 - 2%)	80	15 - 2000	10 - 50

* Used for myelin water maps.

Peak: Short T_2 component signal divided by the total T_2 distribution.

† Signal from CSF was excluded from total distribution.

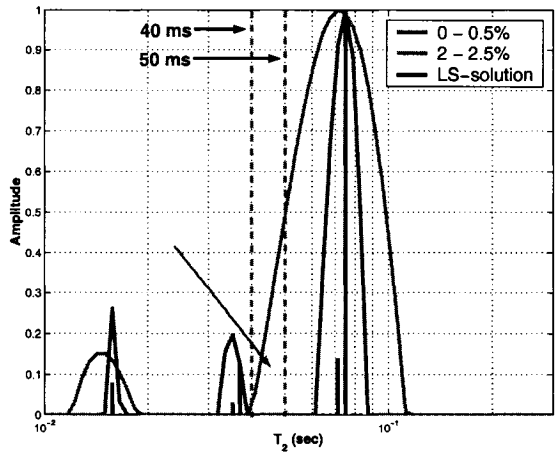

Figure 6.1: A T_2 distribution from *in vivo* data with different amounts of regularization showing how MW range cut-offs are crucial in defining MWFs. Additional signal not related to the short T_2 peak (as pointed out with the pink arrow) can be assigned to the MWF when the main T_2 peak spills over into the MW range.

Certain analysis parameters were unchanged throughout our experiments, namely the type of regularization and T_2 set (range and number of values) upon which our solutions were calculated. The two analysis parameters that were varied were: the MW range and the level of regularization, specified by the parameter μ. MWF estimates from simulated data, similar to that acquired *in vivo*, showed no or very little dependence on MW range or regularization (with the exception of CSF-contaminated signal). In contrast, our *in vivo* data appeared to have larger discrepancies. Figure 6.1 shows an *in vivo* analyzed data set with two levels of regularized distributions (red and green lines) on top of the unregularized LS-solution (blue lines), as well as specific MW ranges. The example shows how the choice of a 50 ms MW cut-off will inherently add signal to the MW pool, resulting in increased MWFs; therefore, clearly demonstrating how crucial MW ranges are in the assignment of signal from various water pools. Another point to note is that the unregularized LS-solution (blue lines) may contain spurious peaks. Insufficient regularization will not suppress these peaks and improper pool assignment may result from unaccounted signal. From this one example, it might appear that less regularization and/or a lower MW cut-off would solve the problem, but our results suggest that this is not the optimal solution. Furthermore, different

analysis procedures might be preferred depending upon factors such as the scanner type and sequence specifics (e.g., type and duration of pulses).

6.2.1 Defining Exact Myelin Water Ranges

In Section 3.4.2, the issue of defined MW ranges *vs.* actual integration bounds was introduced. From simulated WM data with no CSF and SNR = 200 (refer to Figure 3.3 and 3.6), it appears that the choice of integrating up to 40 or 50 ms, let alone including an extra T_2 bin (47.6 *vs.* 50.1 ms), in MWF calculations has minimal consequences. Larger discrepancies in MWFs calculated with varying MW ranges are seen with increased CSF contamination (refer to Figure 3.10). It has been suggested [50] that even the purest tissue sample has a slight presence of a CSF-assigned component. Given the sensitivity to MW range with CSF contamination, it is important for publications to report MW ranges and give exact integration limits.

It has been shown with that the choice of integration limits plays a significant role in MWF values, especially when the main T_2 peak spills below the MW range. Despite choosing similar integration limits, MWF measurements may still be impacted by the actual T_2 sampling used[1]. Standardizing MW ranges and sampling should be perform when possible. Interpolating T_2 distributions so that the MWF integration limits are closer to assigned MW ranges (e.g., stated MW cut-off of 50 ms actually corresponds to 50 ms) could also be performed. This may be a possible retrospective cross-site standardizing step once the effect of interpolation methods (e.g., linear, nearest neighbour, cubic, cubic spline) and step sizes on distributions are clearly understood. Alternatively, the simplest solution to this problem is for groups to test for algorithm consistency, and secondly use the same analysis parameters. The downfall of this fixed parameter idealism is revisited in the discussion of the cross-site reproducibility (Section 6.5).

[1]The logarithmically spaced T_2 set used in our experiments (found in Table 3.3) is specifically generated from 120 values between 15 - 4000 ms. T_2 sets generated with a different number of values and/or a different range will have different components. As previously described, the stated MW range of 40 or 50 ms does not coincide with actual values in the solution set. So, clearly, the chance of precisely matching MW ranges from different T_2 solution sets is slim, thereby posing a problem when comparing results calculated with different T_2 sets and integration limits.

Using Manual Peak Separation Methods

The confinement of the short and main T_2 peaks to their assigned T_2 domain is crucial in maintaining the theory of the short peak being associated with myelin water, the main peak being associated with I/E water, and any $T_2 > 2$ sec being assigned to CSF. The motivation for manually separating the short and main T_2 peaks is that peaks clearly separable by some minima (possibly zero-valued) in the T_2 distribution, which does not coincide with a single assigned or expected MW range upper limit cut-off T_2, should well represent different water components. The premise is that by calculating with a fixed MW range, MWFs would be incorrectly valued when signal from the main peak is included.

The pitfall of the manual peak separation technique is demonstrated by the sample splenium distribution in Figure 5.8. The underlying LS-solution is within the defined MW range but the main T_2 peak extends to a small T_2 (about 20 ms). In a case like this when the peak separation cut-off is too small and the underlying LS-solution shows a component within the MW range cut-off, the peak separation method would underestimate the MWF. A modified definition of the peak separation method where a higher T_2 cut-off value, such as the inflection point[2] of the distribution, might give more accurate MWF estimates. On the other hand, some problematic distributions contained LS-solution peaks right on MW range cut-off values. If no inflection point is present, the choice of MW cut-off is less obvious, hence the reasoning for using fixed MW ranges. It is easy to make exceptions to chosen criteria when looking at distributions case-by-case which, in the limit, is essentially not having any peak separating criteria.

Comparing peak separation MWFs to those found in literature (refer to several UBC studies in Figure 6.2), we find that our WM ROIs using UBC and MNI protocols had lower MWF estimates (due to the large standard deviations for some, they were not significantly different from literature values). Typically, MWF in WM is as much as a factor of 2 different across different brain structures, and values range from about 7 (minor forceps) to 13% (splenium). Our peak separation method values (taking standard deviations into account)

[2]For the splenium distribution of Figure 5.8, the MWF is 6.50% when using the minima (T_2 = 19.2 ms) as the cut-off, whereas using the inflection point (T_2 = 35.2 ms) as the cut-off results in a MWF of 12.58%, which is in the expected range for this ROI.

range from about 4 - 10% in the UBC protocol data and about 3 - 12% for the MNI protocol data. Of particular interest is the splenium which is noted as a structure with higher MWF than the minor or major forceps and the genu. Our splenium MWF estimate was approximately $7 \pm 3\%$ for both protocols and was not the structure with the highest MWF as expected. In closing, for cases where there is no signal below the main T_2 peak, MWF estimates would be zero. In WM ROIs, this is clearly not biologically consistent therefore, the manual peak separation method fails.

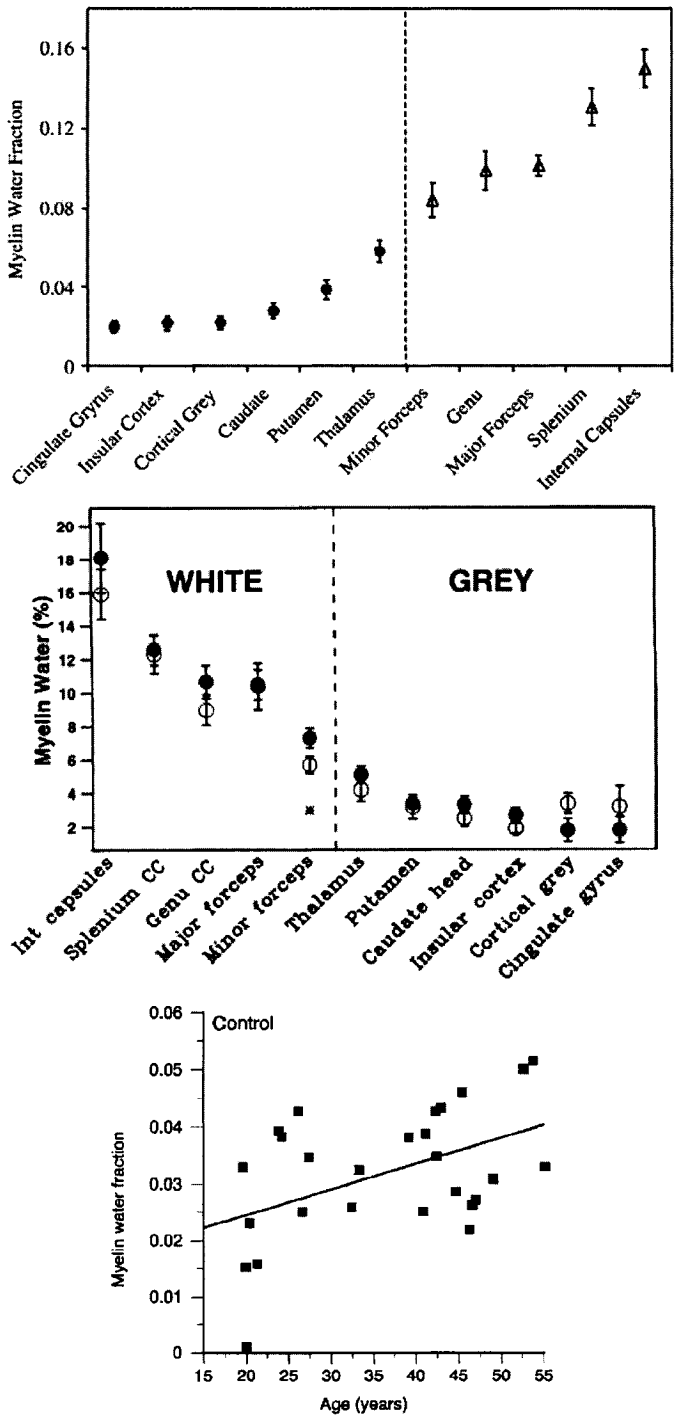

Figure 6.2: Select plots from literature showing MWF estimates with error bars as standard errors across various brain structures in: (*top*) 12 normal subjects [128], (*middle*) 10 normal (solid circle) and MS (empty circle) subjects using a 5 mm slice acquisition, 0.1 - 0.3% regularization and a MW range of 0 - 50 ms (from [46]), and (*bottom*) 27 normal subjects using a 10 mm slice (only for frontal WM) [117]).

6.3 Scan Re-scan Reproducibility of MWF Estimates

MWFs across scans in identical tissue or within adjacent pure WM voxels in a scan showed equal variability. MW content is also expected to be similar for symmetric left-right ROIs of healthy tissue, however, differences were observed but with smaller discrepancies when using the 10 - 40 ms *vs.* the 10 - 50 ms MW range. The MWFs calculated using the 10 - 40 ms MW range are also closer to literature values and although they have lower χ^2 than that of the 10 - 50 ms MW range, we cannot conclude that these values are more accurate.

A similar test/retest study by Vavasour *et al.* [122] using the UBC protocol found that myelin water content (MWC), essentially the MWF but normalized to an external water standard and T_1 corrected, has high reliability coefficients (RC). As a comparison, Table 6.2 lists the MWF and RC from Vavasour's study as a comparison to our scan re-scan results (refer to 10 - 40 ms range values of Tables 5.4 - 5.7). Although results were matched for stated MW ranges, the amount of regularization was not stated, thereby making direct comparisons impossible. Looking across all regularization levels, we generally find that our genu and minor forceps MWF estimates have similar σ but higher means, while splenium results show both higher MWF estimates and σ. The low RC for the splenium indicates that it is not a very reliable measure.

Optimizing and standardizing multi-component analysis parameters such as the number of T_2 values and the range of the MW, T_2 and χ^2 limits can improve MWF reproducibility and is important for multi-centre studies employing this technique. As demonstrated by the

Table 6.2: MWC and RC from the test/retest study by Vavasour *et al.* as a comparison to our scan re-scan results from UBC protocol data. MWC is equivalent to MWF except that it is normalized to a water standard and T_1 corrected. The RC (ranges from 0 to 1) estimates the consistency of a measurement. The more reliable the measure, the higher RC.

ROI	**Genu**	**Splenium**	**Minor forceps**
MWC (σ)	6.2 (1.9)	8.8 (2.0)	4.0 (1.3)
RC	0.88	0.37	0.89

comparison with another test/retest study, comparisons are difficult when complete analysis procedures are not disclosed.

Application: Calculating sample sizes

Scan re-scan studies on human subjects or a multi-component phantom is useful in powering studies for therapeutic trials. For comparison of continuous variables such as lesion MWF, the mean and standard deviation are critical. Besides the MR activity over time, the variability amongst the control group and treated patient group play an important role in determining sample sizes required to show a given treatment effect. If measurement error is less pronounced than biological variability within an ROI, then biological spread essentially determines the sample size. From the scan re-scan experiment, it appears that measurement error is comparable to biological variability. Although biological variability within pure WM or GM tissue cannot be minimized, careful voxel placement can minimize partial voluming and hence apparent variability. Unfortunately, tracking lesion MWF over time does not have the luxury of selecting purely diseased tissue due to slice thickness and in-plane resolution limits, or the selection of identical lesion volumes for each measurement.

G*Power [129], a general power analysis program, was used to compute sample sizes for *a priori* power analysis (i.e., with given effect sizes, alpha levels (α), and power values). Calculations were based on scan re-scan results using the 10 - 40 ms MW range and 2 - 2.5% regularization. The 10 - 50 ms results were not used since they were more dependent on regularization, typically had higher σ_M, and were larger than literature values (refer to Figure 6.2). Table 6.3 gives sample sizes for an actual MWF decrease of 25% with α and β of 0.05 (i.e., false positive and false negative, respectively) and a power of 0.95. As a result of the large spread in normal MWF estimates, detection of pathological changes would require a relatively large sample size as shown in the table.

Table 6.3: Calculated sample sizes required to ensure statistical power (wanted to see a MWF decrease of 25% with $\alpha = 0.05, \beta = 0.95$.)

	Control MWF	Expected MWF	σ	Total sample size
Minor forceps	6.53%	4.90%	1.60%	44
Genu	8.83%	6.62%	1.82%	32
Splenium	13.31%	9.98%	3.15%	42

6.4 Subject and Regional Variations of MWF Estimates

As expected, the results from the normal subject study showed MWF variations with a similar trend across brain structures as reported by the UBC group (Figure 6.2 gives examples for MS and normal subjects from a few studies). The majority of publications from the UBC group, regardless of sample size, report MWF estimates in healthy and MS subjects with relatively small errors. In contrast, the ROI measurements acquired here on 10 subjects, using both the UBC and MNI protocol, showed larger MWF estimates ranging from 0 - 25%, whereas UBC reported values are typically 1 - 14% (compare Figures 5.11 - 5.12 to Figure 6.2). In spite of this, our data generally shows an increase in σ with increased MWF content, which agrees with literature.

Another interesting observation involves the study[3] by Flynn *et al.* [117] which used T_2 distributions, specifically to calculate MWF, to compare schizophrenic patients to a group of normal subjects. Their study showed significant relations between frontal WM MWF and education (increase with education) and age (increase with age, shown in Figure 6.2) in the control group. Particularly of interest is the reported MWF of 0 - 5% (using a MW range 0 - 50 ms), which is clearly lower than other reported values for the minor forceps from UBC studies (Figure 6.2 shows estimates of ~8%). Furthermore, matching our subjects' age (24 - 31 years, mean age 27) to that of Flynn's findings, their expected range for MWF is 2.5 - 4.5%, whereas our UBC protocol MWF using the matched MW range of 10 - 50 ms gave 10.38 $\pm$ 3.29%. A possible explanation for this discrepancy is that Flynn's study used a 10 mm slice. Although they stated that regions were narrowly defined to limit partial

[3]This study was carried out at UBC using the UBC protocol with the exception of the slice thickness (10 mm). Analysis parameters can be found in Table 6.1.

volume effects, chosen volumes may have unwantedly included non-WM structures given the thicker slice which cause the MWF to be lower. However, given the relatively large size of the minor forceps, it is unlikely this could fully explain such a large difference. Slightly mismatched MW integration ranges may also play a role in the discrepancy. The point of this observation is that MWFs can be drastically different from one experiment to another with relatively small differences in the MW range used. To correctly compare MWFs across studies, acquisition parameters and analysis procedures need to be identical or as close as possible.

Overall, we found that subject variability across ROIs was large, but this was largely driven by measurement variability as demonstrated by the variations from the scan re-scan experiment. Using a 50 ms MW range caused MWF estimates to be larger, resulting in even larger variations across brain structures compared to using the smaller MW range of 40 ms, although both MW range cut-off values had equal variability. MWFs calculated from the UBC and MNI protocol data with a 50 ms cut-off typically gives higher MWFs than those reported in literature, but most are not statistically different due to the large σ. The measures calculated from the 40 ms cut-off are better matched with literature values. MWFs from UBC and MNI protocols are not significantly different. As a note, the study by Tozer *et al.*, although using a similar sequence to the UBC protocol but with a different analysis procedure (see Table 6.1), reports a MWF of 9.4 $\pm$ 2.7% in frontal WM for 9 normal subjects (35 $\pm$ 5 years of age) [109]. This study's standard deviation is closer to our reported values, and overlaps with our UBC protocol measurement using the 50 ms cut-off (10.38 $\pm$ 3.29). Both Tozer's and our results (matched for regularization and MW range) overlap with Jones' values of 7.0 $\pm$ 2.0% (right minor forceps), 12 $\pm$ 4.5% (left minor forceps) [115], and Laule's[4] (7.3 $\pm$ 2.1%) [68].

[4]Eighteen healthy subjects were scanned and MWF results were presented as 7.3 $\pm$ 0.5% (mean $\pm$ standard error). Standard error is equivalent to $\sigma/\sqrt{N}$, where N is the number of samples.

6.5 Cross-site Reproducibility

If the same qT_2 protocol was run at two different sites, one would expect the results to be very similar, assuming the same volume in the same subject is acquired and analyzed the same way. Cross-site comparison has allowed us to conclude that although the UBC protocol was implemented at both sites, there is a difference in the acquired data as seen in the different distributions. Although the obvious difference between the sites is the scanner type, other subtle factors (e.g., pulse sequence details, or just scan re-scan reproducibility) may play a role as well. Calculations show that cross-site variability is on the same order as scan re-scan variability. Despite the differences in distribution, the MWF estimates can be quite similar. Therefore, using a consistent acquisition protocol and analysis methods at multiple sites can result in T_2 distributions, and therefore MWFs, within reasonable agreement.

6.5.1 Protocol Differences and the Effect on T_2 Distributions

Data from different protocols, with similar SNRs, acquired on the same scanner and subject show large variations in MWFs. The larger voxels of Protocol 2 are more susceptible to partial volume effects but our ROI selection should have minimized this effect as verified using a high resolution MRI anatomical image[5]. Similarly, the potential slight mismatch between the single slices is likely not able to explain the large MWF variations we observed considering the results from Protocol 1 acquired from two different sites.

Minimizing discrepancies in MWFs requires using the same T_2 vector, as well as choosing identical MW integration ranges. MWF estimates are very sensitive to chosen MW ranges. Before performing multi-site MW studies, investigators should carefully assess cross-site and scan re-scan reproducibility. Assessment in healthy subjects or an appropriate multi-component phantom are necessary to power studies for therapeutic trials. Unless differences resulting from different protocols are understood and accounted for, the same

[5]In view of maintaining sufficiently high SNR, a balance was struck between averaging signal from a large number of voxels and obtaining an absolute absence of partial voluming. Also, considering the larger voxel size of MNI protocol data and resampling algorithm of the image resampling tool, it is inevitable that a very small amount of partial voluming may be present, albeit making up a small fraction of the voxel volume.

protocol should be implemented across sites to minimize measurement error. As shown in the various experiments, the analysis procedure's impact on MWFs is also crucial. Multi-component phantoms would be most suitable for determining necessary analysis parameters to consistently reproduce MWFs using different protocols, as well as same protocols at different centres.

Chapter 7

Conclusion and Future Work

7.1 Summary

Although MWFs give an indication of the myelin content, the technique is very sensitive to subtle changes in the decay curve measurement and/or analysis procedures; therefore, it has not proven to be an extremely reliable measure. Scan re-scan measurement fluctuations indicate the obstacles in longitudinal intra-subject studies where individual subject MWF measurements are inconsistent due to patient alignment and ROI selection. As a consequence, large sample sizes are required to power studies to see differences from group averages in clinical trials. Intra- and cross-site studies have to take measurement variances as a result of subject variability, possibly scanner type differences, and inconsistent analysis methods and parameters, into account. We believe that improved MWF estimate comparisons can be achieved by using a standard phantom to calibrate analysis, or at least understand the differences seen in T_2 distributions and adjust post-processing parameters to give consistent MWFs. Although using a calibration phantom, unlike a human phantoms which would be ideal for these purposes, will expectedly have lower variability due to larger heterogeneous voxels, no slice placement or intra-scan movement errors, and the absence of flow artifacts, they allow for a clearer intial estimate for optimized acquisition and analysis.

The work presented here can be incorporated with qMT development, and areas of disagreement can be further explored to refine each method to better investigate brain tissue. Overall, this qT_2 study should help clarify its validity in imaging healthy and diseased brain, particularly as an *in vivo* marker for myelin.

7.2 Future Work

The simulation study in this thesis only explored the variation of regularization and MW ranges on MWF estimates. Further simulations should include rigorous testing of the effect of changing the T_2 solution (both the number of T_2 values and the range), as well as using decay sampling similar to that in studies which have acquired non-linearly sampled decays curves [111, 130], or used piece-wise sampling to gather information from short and long T_2 components [86, 123, 124, 126, 131, 132].

A more pressing issue, on top of fully characterizing T_2 distributions using various analysis procedures, is for a standardizing procedure to match analysis procedures to protocols for more consistent and accurate MWF estimates. The same protocol implemented at various sites may give slightly different distributions, but optimizing analysis parameters may give the same results. Phantoms with multi-exponential T_2 decay, such as demonstrated with dairy cream [133] or urea-water mixtures [134, 135], should be developed for cross-site studies and longitudinal QA/QC.

There are several issues for protocol and analysis development which should be addressed. A multi-slice acquisition would be more useful than a single slice, but acquisition times have to be maintained or decreased. B_0 and B_1 field maps can be acquired for qT_2 data, but post-acquisition corrections have yet to be derived for multi-exponential data. Lastly, with the advent of high field imaging, a qT_2 acquisition protocol for 3 T should be implemented with all the suggestions made above.

Appendix A

Ethics Approval

The human studies included in this thesis were approved by the Montreal Neurological Institute and Hospital Research Ethics Board. The following document is the confirmation of the approval.

Centre universitaire de santé McGill
McGill University Health Centre

May 9, 2005

Dr Bruce Pike
Magnetic Resonance Imaging
MNI

5.k. PIKB 1995/2 **Quantitative Magnetization Transfer Imaging of Multiple Sclerosis** (CIHR MOP-43871)
Application for Continuing Review of 2005.04.12, English and French consent documents of 2005.04.12

The above submission, reviewed by the full board at the meeting of April 25, 2005 was found, upon receipt of a satisfactory revision of the consent documents in response to our letter of April 26, 2005, to be acceptable for continuation at the McGill University Health Centre (MUHC) and this was entered accordingly into the minutes of the REB meeting.

The reapproval of the study is valid until April 20, 2006.

All research involving human subjects requires review at recurring intervals. To comply with the regulation for continuing review of "at least once per year," it is the responsibility of the investigator to submit an Application for Continuing Review to the REB prior to expiry. However, should the research conclude for any reason prior to approval expiry, you are required to submit a Termination Report to the board once the data analysis is complete to give an account of the study findings and publication status.

The Research Ethics Boards (REBs) of the McGill University Health Centre are registered REBs working under the published guidelines of the Tri-Council Policy Statement, in compliance with the "Plan d'action ministériel en éthique de la recherche et en intégrité scientifique" (MSSS, 1998) and the Food and Drugs Act (2001.06.07), acting in conformity with standards set forth in the (US) Code of Federal Regulations governing human subjects research and functioning in a manner consistent with internationally accepted principles of good clinical practice.

Should any revision to the study or other development occur prior to the next required review, you must advise the REB without delay. Regulation does not permit initiation of a proposed study modification prior to REB approval of the amendment.

We trust this will prove satisfactory to you.

Yours very truly,

Eugene Bereza, MD CM, CCFP, Chair
MNH/I Research Ethics Board
EB/lz

Cc: MUHC Study # PIKB 1995/2

Bibliography

[1] P. Brodal, *The central nervous system: structure and function.* Oxford University Press, Inc., New York, USA, 2004.

[2] F. Dangond, ed., *Disorders of myelin in the central and peripheral nervous systems.* Elsevier Science, Inc., Woburn, MA, USA, 2002.

[3] T. Tabira, M. J. Cullen, P. J. Reier, and H. D. Webster, "An experimental analysis of interlamellar tight junctions in amphibian and mammalian CNS myelin," *J Neurocytol*, vol. 7, pp. 489–503, 1978.

[4] P. Morell, ed., *Myelin.* Plenum Press, New York, USA, 1984.

[5] R. A. Lazzarini, ed., *Myelin biology and disorders (Volume 1 and 2).* Elsevier Academic Press, California, USA, 2004.

[6] J. M. Charcot, "Histologie de la sclérose en plaque," Gazette Hôpitaux, Paris. 1868.

[7] MS Society of Canada, *http://www.mssociety.ca/en/information/default.htm.*

[8] B. G. Weinshenker, G. P. Rice, J. H. Noseworthy, W. Carriere, J. Baskerville, and G. C. Ebers, "The natural history of multiple sclerosis: a geographically based study. 3. Multivariate analysis of predictive factors and models of outcome.," *Brain*, vol. 114, pp. 1045–1056, 1991.

[9] G. Dean and M. Elain, "Age at immigration to England of Asian and Caribbean immigrants and the risk of developing multiple sclerosis," *J Neurol Neurosurg Psychiatry*, vol. 63, pp. 565–568, 1997.

[10] D. A. Dyment, G. C. Ebers, and A. D. Sadovnick, "Genetics of multiple sclerosis," *Lancet Neurol*, vol. 3, pp. 104–110, 2004.

[11] A. G. Osborn, K. L. Salzman, G. Katzman, K. Provenzale, M. Castillo, G. Hedlund, A. Illner, H. R. Harnsberger, J. Cooper, B. V. Jones, and B. Hamilton, *Diagnostic Imaging: Brain*. Amirsys, Inc., Utah, USA, 2004.

[12] S. G. Waxman, ed., *Multiple sclerosis as a neuronal disease*. Elsevier Academic Press, Burlington, MA, USA, 2005.

[13] B. Ferguson, M. K. Matyzszak, M. M. Esiri, and V. H. Perry, "Axonal damage in acute multiple sclerosis lesions," *Brain*, vol. 120, pp. 393–399, 1997.

[14] B. D. Trapp, J. Peterson, R. M. Ransohoff, R. Rudick, S. Mörk, and L. Bö, "Axonal transection in the lesions of multiple sclerosis," *New Eng J Med*, vol. 338, pp. 278–285, 1998.

[15] R. I. Grossman and D. M. Yousem, *Neuroradiology: The Requisites*. Mosby, USA, 2003.

[16] C. A. Davie, G. J. Barker, S. Webb, P. S. Toft, A. J. Thompson, A. E. Harding, W. I. McDonald, and D. H. Miller, "Persistent functional deficit in multiple sclerosis and autosomal dominant cerebellar ataxia is associated with axon loss," *Brain*, vol. 118, pp. 1583–1592, 1995.

[17] B. D. Trapp, R. Ransohoff, and R. Rudick, "Axonal pathology in multiple sclerosis: relationship to neurologic disability," *Curr Opin Neurol*, vol. 12, pp. 295–302, 1999.

[18] F. Bloch, W. W. Hansen, and M. Packard, "Nuclear induction," *Phys Rev*, vol. 69, p. 127, 1946.

[19] F. Bloch, "Nuclear induction," *Phys Rev*, vol. 70, pp. 460–474, 1946.

[20] E. M. Purcell, H. C. Torrey, and R. V. Pound, "Resonance absorption by nuclear magnetic moments in a solid," *Phys Rev*, vol. 69, pp. 37–38, 1946.

[21] P. C. Lauterbur, "Image formation by induced local interactions: examples employing NMR," *Nature*, vol. 242, pp. 190–191, 1973.

[22] E. M. Haacke, R. W. Brown, M. R. Thompson, and R. Venkatesan, *Magnetic resonance imaging: physical principles and sequence design*. John Wiley and Sons Inc., USA, 1999.

[23] E. L. Hahn, "Spin echoes," *Phys Rev*, vol. 80, no. 4, pp. 580–594, 1950.

[24] H. Y. Carr and E. M. Purcell, "Effects of diffusion on free precession in nuclear magnetic resonance experiments," *Phys Rev*, vol. 94, pp. 630–638, 1954.

[25] G. Meiboom and D. Gill, "Modified spin echo method for measuring relaxation times," *Rev Sci Instru*, vol. 29, pp. 688–691, 1958.

[26] R. Freeman, *A Handbook of Nuclear Magnetic Resonance*. Longman Scientific and Technical, England, 1988.

[27] D. H. Miller, R. I. Grossman, S. C. Reingold, and H. F. McFarland, "The role of magnetic resonance techniques in understanding and managing multiple sclerosis," *Brain*, vol. 121, pp. 3–24, 1998.

[28] F. Barkhof and M. Filippi, "Can MR be a predictor of long-term clinical outcome for MS?," *Int MS J*, vol. 2, pp. 4–9, 1995.

[29] P. Jezzard, P. M. Matthews, and S. Smith, eds., *Functional Magnetic Resonance Imaging: An Introduction to Methods*. Oxford University Press, Oxford, UK, 2001.

[30] M. Lee, H. Reddy, H. Johansen-Berg, S. Pendlebury, M. Jenkinson, S. Smith, J. Palace, and P. M. Matthews, "The motor cortex shows adaptive functional changes to brain injury from multiple sclerosis," *Ann Neurol*, vol. 47, pp. 606–613, 2000.

[31] H. Reddy, S. Narayanan, R. Arnoutelis, M. Jenkinson, J. Antel, P. M. Matthews, and D. L. Arnold, "Evidence for adaptive functional changes in the cerebral cortex with axonal injury from multiple sclerosis," *Brain*, vol. 123, pp. 2314–2320, 2000.

[32] S. L. Ramin, W. A. Tognola, and A. R. Spotti, "Proton magnetic resonance spectroscopy: clinical applications in patients with brain lesions," *Sao Paulo Med J*, vol. 121, pp. 254–259, 2003.

[33] A. Bitsch, H. Bruhn, V. Vougioukas, A. Stringaris, H. Lassmann, J. Frahm, and W. Brück, "Inflammatory CNS demyelination: Histopathologic correlation with *in vivo* quantitative proton MR spectroscopy," *AJNR Am J Neuroradiol*, vol. 20, pp. 1619–1627, 1999.

[34] C. Bjartmar, G. Kidd, S. Mork, R. Rudick, and B. D. Trapp, "Neurological disability correlates with spinal cord axonal loss and reduced N-acetyl aspartate in chronic multiple sclerosis patients," *Ann Neurol*, vol. 48, pp. 893–901, 2000.

[35] J. H. T. M. van Waesberghe, W. Kamphorst, C. J. A. D. Groot, M. A. A. van Walderveen, J. A. Castelijns, R. Ravid, G. J. L. a. Nijeholt, P. van der Valk, C. H. Polman, A. J. Thompson, and F. Barkhof, "Axonal loss in multiple sclerosis lesions: Magnetic resonance imaging insights into substrates of disability," *Ann Neurol*, vol. 46, pp. 747–754, 1999.

[36] J. R. Hesselink, M. B. Zlatkin, and R. R. Edelman, eds., *Clinical magnetic resonance imaging*. WB Saunders, Philadelphia, USA, 1996.

[37] T. M. Rudkin and D. A. Arnold, "Proton magnetic resonance spectroscopy for the diagnosis and management of cerebral disorders," *Arch Neurol*, vol. 56, pp. 919–926, 1999.

[38] D. Le Bihan, E. Breton, D. Lallem, , P. Grenier, E. A. Cabanis, and M. Lavel-Jeantet, "MR imaging of intravoxel incoherent motions: application to diffusion and perfusion in neurologic disorders," *Radiology*, vol. 161, pp. 401–407, 1986.

[39] P. Tofts, ed., *Quantitative MRI of the Brain: Measuring Changes Caused by Disease*. John Wiley and Sons Ltd., England, 2003.

[40] G. B. Pike, "Magnetization transfer imaging of multiple sclerosis," *Ital J Neurol Sci*, vol. 18, pp. 359–365, 1997.

[41] R. M. Henkelman, X. Huang, Q. S. Xiang, G. J. Stanisz, S. D. Swanson, and M. J. Bronskill, "Quantitative interpretation of magnetization transfer," *Magn Reson Med*, vol. 29, no. 6, pp. 759–766, 1993.

[42] H. M. McConnell, "Reaction rates by nuclear magnetic resonance," *J Chem Phys*, vol. 28, pp. 430–431, 1958.

[43] T. A. Bjarnason, *The effect of cross relaxation on the NMR behaviour of bovine white matter*. PhD thesis, University of British Columbia, 2005.

[44] S. D. Wolff and R. S. Balaban, "Magnetization transfer imaging: practical aspects and clinical applications," *Radiology*, vol. 192, pp. 593–599, 1994.

[45] V. Dousset, R. I. Grossman, K. N. Ramer, M. D. Schnall, L. H. Young, F. Gonzales-Scarano, E. Lavi, and J. A. Cohen, "Experimental allergic encephalomyelitis and multiple sclerosis: lesion characterization with magnetization transfer imaging," *Radiology*, vol. 182, pp. 483–491, 1992.

[46] I. M. Vavasour, K. P. Whittall, A. L. MacKay, D. K. B. Li, G. Vorobeychik, and D. W. Paty, "A comparison between magnetization transfer ratios and myelin water percentages in normals and multiple sclerosis patients," *Magn Reson Med*, vol. 40, pp. 763–768, 1998.

[47] R. M. Henkelman, G. J. Stanisz, and S. J. Graham, "Magnetization transfer in MRI: a review," *NMR Biomed*, vol. 14, pp. 57–64, 2001.

[48] J. G. Sled and G. B. Pike, "Quantitative imaging of magnetization transfer exchange and relaxation properties *in vivo* using MRI," *Magn Reson Med*, vol. 46, pp. 923–931, 2001.

[49] J. G. Sled and G. B. Pike, "Correction for B_1 and B_0 variations in quantitative T_2 measurements using MRI," *Magn Reson Med*, vol. 43, pp. 589–593, 2000.

[50] K. P. Whittall, A. L. MacKay, and D. K. B. Li, "Are mono-exponential fits to a few echoes sufficient to determine T_2 relaxation for *in vivo* human brain?," *Magn Reson Med*, vol. 41, pp. 1255–1257, 1999.

[51] T. J. Swift and O. J. J. Fritz, "A proton spin-echo study of the state of water in frog nerves.," *Biophys J*, vol. 9, pp. 54–59, 1969.

[52] V. Vasilescu, E. Katona, V. Simplaceanu, and D. Demco, "Water compartments in the myelinated nerve. iii. Pulsed NMR results," *Experientia*, vol. 34, pp. 1443–1444, 1978.

[53] R. S. Menon and P. S. Allen, "Application of continuous relaxation time distributions to the fitting of data from model systems and excised tissue," *Magn Reson Med*, vol. 20, pp. 214–227, 1991.

[54] R. S. Menon, M. S. Rusinko, and P. S. Allen, "Proton relaxation studies of water compartmentalization in a model neurological system," *Magn Reson Med*, vol. 28, pp. 264–274, 1992.

[55] W. A. Stewart, A. L. MacKay, K. P. Whittall, G. R. Moore, and D. W. Paty, "Spin-spin relaxation in experimental allergic encephalomyelitis. Analysis of CPMG data using a non-linear least squares method and linear inverse theory.," *Magn Reson Med*, vol. 29, pp. 767–775, 1993.

[56] A. MacKay, K. Whittall, J. Adler, D. Li, D. Paty, and D. Graeb, "*In vivo* visualization of myelin water in brain by magnetic resonance," *Magn Reson Med*, vol. 31, pp. 673–677, 1994.

[57] M. D. Does and R. E. Snyder, "T_2 relaxation of peripheral nerve measured *in vivo*," *Magn Reson Imaging*, vol. 13, pp. 575–580, 1995.

[58] R. Harrison, M. J. Bronskill, and R. M. Henkelman, "Magnetization transfer and T_2 relaxation components in tissue," *Magn Reson Med*, vol. 33, pp. 490–496, 1995.

[59] C. Beaulieu, F. R. Fenrich, and P. S. Allen, "Multicomponent water proton transverse relaxation and T_2-discriminated water diffusion in myelinated and nonmyelinated nerve," *Magn Reson Imaging*, vol. 16, no. 10, pp. 1201–1210, 1998.

[60] P. J. Gareau, B. K. Rutt, C. V. Bowen, S. J. Karlik, and J. R. Mitchell, "*In vivo* measurements of multi-component T_2 relaxation behaviour in guinea pig brain," *Magn Reson Imaging*, vol. 17, pp. 1319–1325, 1999.

[61] S. Peled, D. G. Cory, S. A. Raymond, D. A. Kirschner, and F. A. Jolesz, "Water diffusion, T_2, and compartmentalization in frog sciatic nerve," *Magn Reson Med*, vol. 42, pp. 911–918, 1999.

[62] M. D. Does and R. E. Snyder, "Multiexponential T_2 relaxation in degenerating peripheral nerve," *Magn Reson Med*, vol. 35, pp. 207–213, 1996.

[63] K. P. Whittall, A. L. MacKay, D. A. Graeb, R. A. Nugent, D. K. B. Li, and D. W. Paty, "*In vivo* measurement of T_2 distributions and water contents in normal human brain," *Magn Reson Med*, vol. 37, pp. 34–43, 1997.

[64] K. P. Whittall and A. L. MacKay, "Quantitative interpretation of NMR relaxation data," *J Magn Reson*, vol. 84, pp. 134–152, 1989.

[65] I. M. Vavasour, K. P. Whittall, D. K. B. Li, and A. L. MacKay, "Different magnetization transfer effects exhibited by the short and long T_2 components in human brain," *Magn Reson Med*, vol. 44, pp. 860–866, 2000.

[66] C. K. Jones, K. P. Whittall, and A. L. MacKay, "Robust myelin water quantification: averaging vs. spatial filtering," *Magn Reson Med*, vol. 50, pp. 206–209, 2003.

[67] C. K. Jones, Q. S. Xiang, K. P. Whittall, and A. L. MacKay, "Linear combination of multiecho data: short T_2 component selection," *Magn Reson Med*, vol. 51, pp. 495–502, 2004.

[68] C. Laule, I. M. Vavasour, G. R. W. Moore, J. Oger, D. K. B. Li, D. W. Paty, and A. L. MacKay, "Water content and myelin water fraction in multiple sclerosis: a T_2 relaxation study," *J Neurol*, vol. 251, pp. 284–293, 2004.

[69] G. R. W. Moore, E. Leung, A. L. MacKay, I. M. Vavasour, K. P. Whittall, K. S. Cover, D. K. B. Li, S. A. Hashimoto, J. Oger, T. J. Sprinkle, and D. W. Paty, "A pathology-MRI study of the short-T_2 component in formalin-fixed multiple sclerosis brain," *Neurology*, vol. 55, pp. 1506–1510, 2000.

[70] H. B. W. Larsson, J. Frederiksen, L. Klaer, O. Henriksen, and J. Olesen, "*In vivo* determination of T_1 and T_2 in the brain of patients with severe but stable multiple sclerosis," *Magn Reson Med*, vol. 7, pp. 43–55, 1988.

[71] J. Kesselring, D. H. Miller, D. G. MacManus, G. Johnson, N. M. Milligan, N. Scolding, D. A. S. Compston, and W. I. McDonald, "Quantitative magnetic resonance imaging in multiple sclerosis: the effect of high dose intravenous methylprednisolone," *Magn Reson Med*, vol. 51, pp. 495–502, 2004.

[72] D. H. Miller, G. Johnson, P. S. Tofts, D. MacManus, and W. I. McDonald, "Precise relaxation time measurements of normal-appearing white matter in inflammatory central nervous system disease," *Magn Reson Med*, vol. 11, pp. 331–336, 1989.

[73] J. P. Armspach, D. Gounot, L. Rumbach, and J. Chambron, "*In vivo* determination of multiexponential T_2 relaxation in the brain of patients with multiple sclerosis," *Magn Reson Imaging*, vol. 9, pp. 107–113, 1991.

[74] V. M. Haughton, F. Z. Yetkin, S. M. Rao, A. A. Rimm, M. E. Fischer, R. A. Papke, R. K. Breger, and B. O. Khatri, "Quantitative MR in the diagnosis of multiple sclerosis," *Magn Reson Med*, vol. 26, pp. 71–78, 1992.

[75] S. Barbosa, L. D. Blumhardt, N. Roberts, T. Lock, and R. H. Edwards, "Magnetic resonance relaxation time mapping in multiple sclerosis: normal appearing white matter and the "invisible" lesion load," *Magn Reson Imaging*, vol. 12, pp. 33–42, 1994.

[76] C. Gasperini, M. A. Horsfield, J. W. Thorpe, D. Kidd, G. J. Barker, P. S. Tofts, D. G. MacManus, A. J. Thompson, D. H. Miller, and W. I. McDonald, "Macroscopic and microscopic assessments of disease burden by MRI in multiple sclerosis: relationship to clinical parameters," *J Magn Reson Imaging*, vol. 6, pp. 580–584, 1996.

[77] D. E. Goodkin, W. D. Rooney, R. Sloan, P. Bacchetti, L. Gee, M. Vermathen, E. Waubant, M. Abundo, S. Majumdar, S. Nelson, and M. W. Weiner, "A serial study of new MS lesions and the white matter from which they arise," *Neurology*, vol. 51, pp. 1689–1697, 1998.

[78] A. J. Thompson, A. G. Kermode, D. Wicks, D. G. MacManus, B. E. Kendall, D. P. E. Kingsley, and W. I. McDonald, "Major differences in the dynamics of primary and secondary progressive multiple sclerosis," *Ann Neurol*, vol. 29, pp. 53–62, 1991.

[79] D. Kidd, G. J. Barker, P. S. Tofts, A. Gass, A. J. Thompson, W. I. McDonald, and D. H. Miller, "The transverse magnetisation decay characteristics of longstanding lesions and normal-appearing white matter in multiple sclerosis," *J Neurol*, vol. 244, pp. 125–130, 1997.

[80] K. P. Whittall, A. L. MacKay, D. K. B. Li, I. M. Vavasour, C. K. Jones, and D. W. Paty, "Normal-appearing white matter in multiple sclerosis has heterogeneous, diffusely prolonged T_2," *Magn Reson Med*, vol. 47, no. 2, pp. 403–408, 2002.

[81] P. J. Gareau, B. K. Rutt, S. J. Karlik, and J. R. Mitchell, "Magnetization transfer and multicomponent T_2 relaxation measurement with histopathologic correlation in an experimental model of ms," *J Magn Reson Imaging*, vol. 11, pp. 586–595, 2000.

[82] G. Stanisz, A. Kecojevic, M. J. Bronskill, and R. M. Henkelman, "Characterizing white matter with magnetization transfer and T_2," *Magn Reson Med*, vol. 42, pp. 1128–1136, 1999.

[83] T. A. Bjarnason, I. M. Vavasour, C. L. L. Chia, and A. L. MacKay, "Characterization of the NMR behavior of white matter in bovine brain," *Magn Reson Med*, vol. 54, pp. 1072–1081, 2005.

[84] T. A. Bjarnason and A. L. MacKay, "Magnetization transfer parameters in white matter can be described using a four-pool model," *Proc Imaging Myelin: Formation, Destruction and Repair, Vancouver*, p. 58, 2006.

[85] S. Portnoy and G. J. Stanisz, "MT effects in white matter - is a two-pool model enough?," *Proc 14th Int Soc Mag Res Med*, p. 2110, 2006.

[86] C. Laule, K. P. Whittall, and A. L. MacKay, "Shortening the acquisition time of a 48-echo T_2 relaxation pulse sequence by varying TR across k-space," *Proc 9th Int Soc Mag Res Med*, p. 896, 2001.

[87] B. Mädler and A. L. MacKay, "*In vivo* 3D T_2-relaxation measurements for quantitative myelin imaging," *Proc Imaging Myelin: Formation, Destruction and Repair, Vancouver*, p. 72, 2006.

[88] L. Vidarsson, S. M. Conolly, K. O. Lim, G. E. Gold, and J. M. Pauly, "Echo time optimization for linear combination myelin imaging," *Magn Reson Med*, vol. 53, pp. 398–407, 2005.

[89] L. Vidarsson, B. Mueller, K. O. Lim, and J. M. Pauly, "Myelin-water imaging at 3T with linear combination (LC) filtering," *Proc Imaging Myelin: Formation, Destruction and Repair, Vancouver*, p. 67, 2006.

[90] L. Vidarsson, B. Mueller, K. O. Lim, and J. M. Pauly, "Linear combination filtering in white matter with steady-state free-precession (SSFP) sequences," *Proc 14th Int Soc Mag Res Med*, 2006.

[91] P. D. Gatehouse and G. M. Bydder, "Magnetic resonance imaging of short T_2 components in tissue," *Clin Radiol*, vol. 58, pp. 1–19, 2003.

[92] P. E. Z. Larson, J. M. Pauly, and D. G. Nishimura, "UTE imaging in the brain with robust long-T_2 suppression pulses," *Proc Imaging Myelin: Formation, Destruction and Repair, Vancouver*, p. 63, 2006.

[93] R. M. Kroeker and R. M. Henkelman, "Analysis of biological NMR relaxation data with continuous distributions of relaxation times," *J Magn Reson*, vol. 69, pp. 218–235, 1986.

[94] S. J. Graham, P. L. Stanchev, and M. J. Bronskill, "Criteria for analysis of multicomponent tissue T_2 relaxation data," *Magn Reson Med*, vol. 35, pp. 370–378, 1996.

[95] F. R. E. Fenrich, C. Beaulieu, and P. S. Allen, "Relaxation times and microstructures," *NMR Biomed*, vol. 14, pp. 133–139, 2001.

[96] T. Andrews, J. L. Lancaster, S. J. D. C. Contreras-Sesvold, and P. T. Fox, "Testing the three-pool white matter model adapted for use with T_2 relaxometry," *Magn Reson Med*, vol. 54, pp. 449–454, 2005.

[97] R. M. Henkelman, "Measurement of signal intensities in the presence of noise in MR images," *Med Phys*, vol. 12, no. 2, pp. 232–233, 1985.

[98] H. Gudbjartsson and S. Patz, "The Rician distribution of noisy MRI data," *Magn Reson Med*, vol. 34, pp. 910–914, 1995.

[99] S. W. Provencher, "A constrained regularization method for inverting data represented by linear algebraic or integral equations," *Comput Phys Commun*, vol. 27, pp. 213–227, 1982.

[100] S. W. Provencher, "CONTIN: A general purpose constrained regularization program for inverting noisy linear algebraic and integral equations," *Comput Phys Commun*, vol. 27, pp. 229–242, 1982.

[101] C. L. Lawson and R. J. Hanson, *Solving least square problems*. Prentice Hall, New Jersey, USA, 1974.

[102] S. I. Gass, *Linear programming*. McGraw-Hill, New York, US, 1969.

[103] D. G. Luenberger, *Introduction to linear and nonlinear programming*. Addison-Wesley, Massachusetts, US, 1973.

[104] J. L. Lancaster, T. Andrews, L. J. Hardies, S. Dodd, and P. T. Fox, "Three pool model of white matter," *J Magn Reson Imaging*, vol. 17, pp. 1–10, 2003.

[105] J. J. Jain and W. E. Reddick, "Constrained triple-component T_2 quantification *in vivo*," *Proc 14th Int Soc Mag Res Med*, p. 2517, 2006.

[106] M. D. Does, C. Beaulieu, P. S. Allen, and R. E. Snyder, "Multi-component T_1 relaxation and magnetisation transfer in peripheral nerve," *Magn Reson Imaging*, vol. 16, pp. 1033–1041, 1998.

[107] M. D. Does and J. C. Gore, "Rapid acquisition transverse relaxometric imaging," *J Magn Reson*, vol. 147, pp. 116–120, 2000.

[108] K. Wachowicz and R. E. Snyder, "Assignment of the T_2 components of amphibian peripheral nerve to their microanatomical compartments," *Magn Reson Med*, vol. 47, pp. 239–245, 2002.

[109] D. J. Tozer, G. R. Davies, D. R. Altmann, D. H. Miller, and P. S. Tofts, "Correlation of apparent myelin measures obtained in multiple sclerosis patients and controls from magnetization transfer and multicompartmental T_2 analysis," *Magn Reson Med*, vol. 53, pp. 1415–1422, 2005.

[110] G. Stanisz, E. E. Odrobina, J. Pun, M. Escaravage, S. J. Graham, M. J. Bronskill, and R. M. Henkelman, "T_1, T_2 relaxation and magnetization transfer in tissue at 3T," *Magn Reson Med*, vol. 54, pp. 507–512, 2005.

[111] J. Oh, E. T. Han, D. Pelletier, and S. J. Nelson, "Measurement of *in vivo* multicomponent T_2 relaxation times for brain tissue using multi-slice T_2 prep at 1.5 and 3 T," *Magn Reson Imaging*, vol. 24, pp. 33–43, 2006.

[112] K. P. Whittall, M. J. Bronskill, and R. M. Henkelman, "Investigation of analysis techniques for complicated NMR relaxation data," *J Magn Reson*, vol. 95, pp. 221–234, 1991.

[113] M. A. Bernstein, K. F. King, and X. J. Zhou, *Handbook of MRI pulse sequences*. Elsevier Academic Press, Burlington, MA, USA, 2004.

[114] G. Saab, R. T. Thompson, and G. D. Marsh, "Multicomponent T_2 relaxation of *in vivo* skeletal muscle," *Magn Reson Med*, vol. 42, pp. 150–157, 1999.

[115] C. K. Jones, *T_2 decay curve acquisition and analysis in MRI*. PhD thesis, University of British Columbia, 2003.

[116] C. S. Poon and R. M. Henkelman, "Practical T_2 quantitation for clinical applications," *J Magn Reson Imaging*, vol. 2, pp. 541–553, 1992.

[117] S. W. Flynn, D. J. Lang, A. L. MacKay, V. Goghari, I. M. Vavasour, K. P. Whittall, G. N. Smith, V. Arango, J. J. Mann, A. J. Dwork, P. Falkai, and W. G. Honer, "Abnormalities of myelination in schizophrenia detected *in vivo* with MRI, and post-mortem with analysis of oligodendrocyte proteins," *Mol Psychiatry*, vol. 8, pp. 811–820, 2003.

[118] C. Laule, E. Leung, D. K. Li, A. L. Traboulsee, D. W. Paty, A. L. MacKay, and G. W. Moore, "Myelin water imaging in multiple sclerosis: quantitative correlations with histopathology," p. 461, 2004.

[119] I. M. Vavasour, *Magnetic resonance of human and bovine brain*. PhD thesis, University of British Columbia, 1998.

[120] I. M. Vavasour, D. K. B. Li, A. L. Traboulsee, and A. L. MacKay, "Multi-parametric MT of T_1 black holes in multiple sclerosis: evidence that myelin loss is not greater," *Proc Imaging Myelin: Formation, Destruction and Repair, Vancouver*, p. 77, 2006.

[121] I. M. Vavasour, D. K. B. Li, C. Laule, A. L. Traboulsee, and A. L. MacKay, "Myelin water is an independent measure of pathology in multiple sclerosis," *Proc Imaging Myelin: Formation, Destruction and Repair, Vancouver*, p. 78, 2006.

[122] I. M. Vavasour, C. M. Clark, D. K. B. Li, and A. L. MacKay, "Reproducibility and reliability of MR measurements in white matter: clinical implications," *Proc Imaging Myelin: Formation, Destruction and Repair, Vancouver*, p. 79, 2006.

[123] C. Laule, S. A. Tahir, S. M. Sirrs, E. E. Brief, C. Bishop, D. K. B. Li, and A. L. MacKay, "Long T_2 imaging: evidence of a new water reservoir in phenylketonuria," *Proc 14th Int Soc Mag Res Med*, p. 960, 2006.

[124] S. H. Kolind, C. Laule, D. K. B. Li, A. L. Traboulsee, T. A. Bjarnason, I. M. Vavasour, and A. L. MacKay, "Myelin water fraction is not strongly correlated with diffusion measures in multiple sclerosis," *Proc Imaging Myelin: Formation, Destruction and Repair, Vancouver*, p. 75, 2006.

[125] C. Laule, A. L. Traboulsee, D. K. B. Li, and A. L. MacKay, "Long T_2 imaging: evidence of a new water reservoir in multiple sclerosis," *Proc 14th Int Soc Mag Res Med*, p. 446, 2006.

[126] D. Lang, A. L. MacKay, C. Laule, L. C. Kopala, G. W. MacEwan, and W. G. Honer, "Assessment of subregional myelination in first-episode psychosis patients using myelin water imaing," *Proc Imaging Myelin: Formation, Destruction and Repair, Vancouver*, p. 70, 2006.

[127] K. J. Whitaker, C. M. Clark, and A. L. MacKay, "Myelination of the corpus callosum and reticular formation of males aged 8 to 12 years," *Proc Imaging Myelin: Formation, Destruction and Repair, Vancouver*, p. 71, 2006.

[128] A. MacKay, C. Laule, I. Vavasour, T. Bjarnason, S. Kolind, and B. Mädler, "Insights into brain microstructure from the T_2 distribution," *Magn Reson Imaging*, vol. 24, pp. 515–525, 2006.

[129] G*Power, *http://www.psycho.uni-duesseldorf.de/aap/projects/gpower/*.

[130] D. Pelletier, E. T. Han, S. J. Nelson, and J. Oh, "Supratentorial brain myelin water at 3 T in MS: an *in vivo* clinical application," *Proc Imaging Myelin: Formation, Destruction and Repair, Vancouver*, p. 73, 2006.

[131] S. H. Kolind, C. Laule, T. A. Bjarnason, I. M. Vavasour, A. L. Traboulsee, D. K. Li, and A. L. MacKay, "Correlation of diffusion measures with multicomponent T_2-relaxation data in multiple sclerosis lesions and normal appearing white matter," *Proc 13th Int Soc Mag Res Med*, p. 314, 2005.

[132] T. A. Bjarnason, "Will piecewise continuous echo spacing adversely affect the T_2 distribution?," *Proc 14th Int Soc Mag Res Med*, p. 1501, 2006.

[133] C. K. Jones, A. L. MacKay, and B. Rutt, "Bi-exponential T_2 decay in dairy cream phantoms," *Magn Reson Imaging*, vol. 16, no. 1, pp. 83–85, 1998.

[134] J. H. Lee, C. Labadie, S. Springer Jr., and G. S. Harbison, "Two-dimensional inverse Laplace transform NMR: altered relaxation times allow detection of exchange correlation," *J Am Chem Soc*, vol. 115, pp. 7761–7764, 1993.

[135] R. A. Horch and M. D. Does, "MRI phantoms with independently-controllable biexponential-T_2 decays," *Proc 14th Int Soc Mag Res Med*, p. 2518, 2006.